Study of Relativistic Jets in Active Galactic Nuclei Based on their Dynamics

力学に基づいた活動銀河核からの
相対論的ジェットの研究

２００８年 １２月

早稲田大学大学院 理工学研究科
物理及応用物理学専攻 宇宙物理学研究

伊藤 裕貴

Abstract

The properties of relativistic jets in active galactic nuclei (AGNs) are studied based on their dynamics. In order to do this, we use the analytical models which describe the dynamical evolutions of cocoons and shells which are formed via the interaction of jets with the surrounding ambient gas. In the present study, we particularly focus on the energetics of the jets and the emissions from the cocoons and shells.

By comparing the observed radio morphology of four bright FRII radio galaxies (Cygnus A, 3C 223, 3C 284, and 3C 219) with the analytical model of cocoon expansion, we evaluate the kinetic power of jets and the source age. It is found that large fractions $\gtrsim 0.02 - 0.7$ of the Eddington luminosity are carried away as kinetic power of jets. The upper limit of the ratio of jet kinetic power to the Eddington luminosity is larger than unity ($\lesssim 10$) for some sources, suggesting the possibility of super-Eddington mass accretions. As a consequence of the large powers, we also find that the total internal energy stored in the cocoon exceeds the energy derived from the minimum energy condition for the energy of radiating non-thermal electrons and magnetic fields. For the most powerful sources, the ratio of the total internal energy to the minimum energy can be as large as ~ 310. This result strongly suggests that most of the energy in cocoon is carried by invisible components such as thermal leptons (electron and positron) and/or protons.

As for the emissions associated with the cocoons, we evaluate the thermal bremsstrahlung emissions based on the model of cocoon expansion. Considering the thermal evolution of the cocoon, we find that the temperatures of plasma in the cocoon do not vary with time and are solely determined by the bulk Lorentz factor of the jet. The electron temperature is typically predicted in the range of MeV in the case of jet with bulk Lorentz factor of ~ 10. As a result, the bremsstrahlung emission peaked at MeV-γ band is predicted. We also find that the luminosity of young cocoon is brighter than that of older cocoon since the number density of the thermal electrons decrease with time.

We also explore the properties of the emissions from the shells based on the analytical model. First, we evaluate the effect of radiative cooling due to thermal bremsstrahlung emission on the dynamics. As a result, we find that the effect is negligible for a reasonable parameter range of kinetic power of jet and ambient mass density. Therefore, the shocks driven into the ambient medium by the jets can be considered as an adiabatic shock. Next, by assuming that constant fraction of internal energy in the shell is converted into that of non-thermal electrons via diffusive shock acceleration, we evaluate the spectrum of synchrotron emission. As a result, we find that the spectrum extends in wide range , up to X-ray band ($10^{17} - 10^{18}$Hz)

when Bohm diffusion limit is assumed. It is also found that the attainable peak luminosity is common among all frequencies and is determined solely by the kinetic power of jet and the ratio of energy of accelerated electrons to that of the total internal energy. We also discuss the detectability of the synchrotron emission at various frequencies and show that the observations at IR/optical/UV band is suited for the detection since observation at lower (radio) and higher (X-ray) is likely to be hampered by the emissions from radio lobe and the thermal emissions from the ambient gas and co-existing thermal electrons within the shell, respectively. Moreover, with regard to the source sizes, young compact sources are favored for detection, since their surface brightness tends to be higher than that of larger sources. It is suggested that the observations of compact radio sources ($\lesssim 10\mathrm{kpc}$) through the detectors such as Subaru Telescope and Hubble Space Telescope can be used as a powerful probe for the physics of electron acceleration.

Contents

Chapter 1
INTRODUCTION

1.1 What are AGN?

Active Galactic Nuclei (AGNs) are one of the spectacular object in the universe. Although their size is small ($\ll 1$ pc), their luminosity can be as much as 10^4 times the luminosity of a typical galaxy ($\sim 10^{44}$ ergs s^{-1}). Their radiation frequencies cover extraordinary broad range, ranging from radio to X-ray. $1 - 10\%$ of galaxies posses AGNs and are called active galaxies.

1.1.1 Standard picture

Radiation from the AGN is commonly believed to be gravitational energy released by matter spiraling around a supermassive central black hole of about $M_{\rm BH} \sim 10^6 - 10^{10} M_\odot$ (e.g., Ferrarese & Merritt 2000; Gebhardt et al. 2000; Shields et al. 2003) (see Fig. 1.1). Though the central engine which produces the enormous observed activity cannot be resolved observationally, a standard picture of an AGN has gradually emerged. Below we summarize the main components of AGN. Here we express the length scale using the gravitational radius, $r_{\rm g} = 2GM_{\rm BH}/c^2$, where G and c are gravitational constant and speed of light, respectively.

- an accretion disk from about 2 to $100 r_{\rm g}$ feeding the central black hole and emitting mainly in the UV and soft X-rays;
- the broad line optically emitting clouds (BLR), which seem to be absent in some sources (e.g. FRI, see hereafter) and extend up to a few $10^2 r_{\rm g}$ from the center. The BLR emission can be radiation scattered by hot electrons further away while the word 'cloud' should be taken in the broad sense meaning dense gas with a filling factor less than unity;
- a dusty torus (or wrapped disk or dusty bipolar flow) with an inner radius of a few $10^3 r_{\rm g}$, which obscures the central parts of the AGN from transverse lines of sight;
- the narrow line regions (NLR) which extend from about 10^4 to $10^6 r_{\rm g}$;
- powerful jets of plasma detected from the sub-parsec to the Mpc scales, mainly in the radio but also in the optical, UV and X-rays.

1.1.2 Unified model

Although numerous subvarieties have been named (see e.g., Krolik 1999 for review), AGNs can be classified into three broad classes classes (Antonucci 1993; Urry & Padovani 1995) based on the phenomenology of their emission in the radio and optical/UV parts of the spectrum. The overall classification is given as follows:

- Type 2: AGN have weak continua with narrow emission lines (NLR). They include, in the radio quiet group, the low luminosity type 2 Seyfert galaxies (Sey 2), while the radio-loud counterpart regroups the narrow-line radio galaxies.
- Type 1: AGN have bright continua with broad emission lines (BLR) in addition to the NLR. The type 1 radio-quiet group is composed of type 1 Seyfert galaxies (Sey 1) and the higher luminosity radio-quiet quasars (QSO), while the radio-loud group includes the broad line radio galaxies (BLRG) at low luminosities and the flat or steep spectrum radio-loud quasars (FSRQ and SSRQ) at higher luminosities.
- Type 0: AGN correspond to the remaining radio-loud class which is called the Blazars (BL Lacs and FSRQ).

In the unified scheme, various AGNs can be classified according to orientation, beaming and obscuration effects. The transition from Type 1 to Type 2 of the class of radio-quiet AGN is based on orientation effects alone. In Type 2 the viewing angle is close to disk edge-on and obtains remaining values for Types 1. The broad emission lines arise from clouds orbiting above but nearby the disk (BLR, see Fig. 1.1). Thus, when the line of sight makes a small angle with the system axis, they are not obscured by the dusty torus, as in type 1 Seyfert, while wherein these broad emission lines are obscured by the torus, only the narrow emission lines are visible because they are produced further away (NLR), as it is the case with type 2 Seyfert.

In radio-loud AGN, bipolar outflow is present. The outflow is relativistic at least in parsec scales, very well collimated in the form of a jet and quite powerful. Hence, among radio-loud AGN, the transition from Type 0 (Blazars) to Type 2 is based on a combination of orientation effect, and also depends on the angle between its relativistic jet and the line of sight. Note that in radio-quiet AGN the outflow is either stopped or loosely collimated in the form of a wind or a bipolar flow.

.

1.2 AGN Jets

Among all, about $10\ \%$ of AGNs are strong radio sources (radio-loud). As mentioned in the previous section, these objects are associated with pair of jets which emanate from AGN in opposite direction (Fig. 1.1). Their observed radio images show various morphology and covers

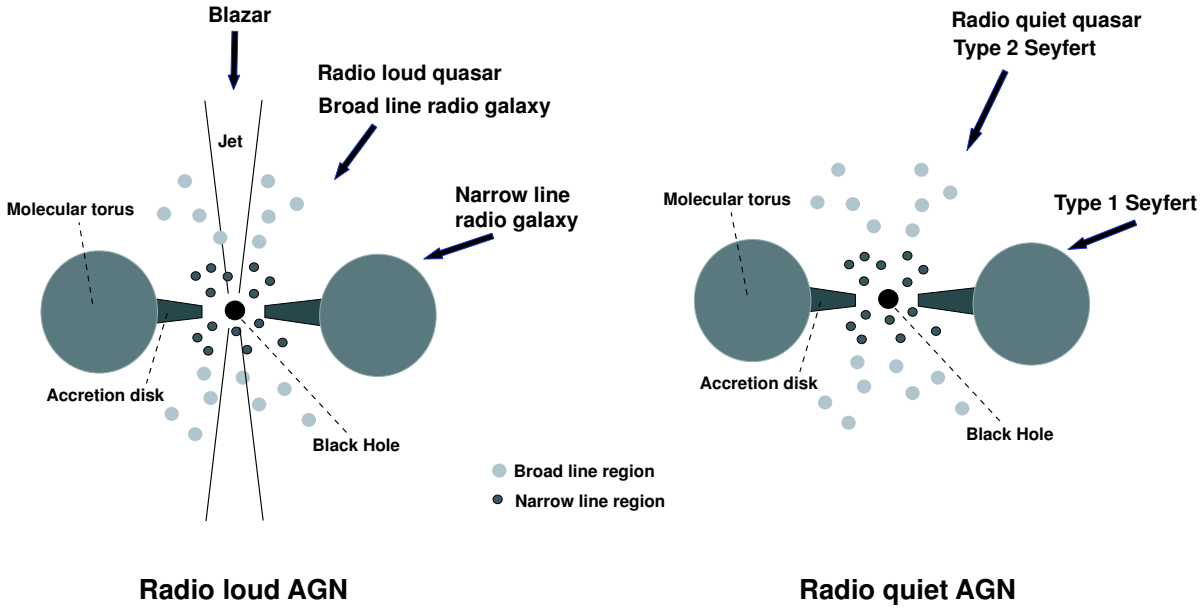

Figure 1.1: General sketch, not to scale, for unified scheme of AGNs. The left panel corresponds to the radio-loud AGNs, while the right panel corresponds to radio-quiet AGNs

wide range in size. It is well established that these emissions are the consequence of interactions between the AGN jets and the surrounding interstellar medium (ISM) or intracluster medium (ICM) depending on its scale (e.g., Begelman, Blandford, & Rees 1984 for review).

In this section, we briefly review the properties of the AGN jets which are subject of this thesis. Particularity, we focus on the morphology of the radio sources and its dynamics.

1.2.1 Observed properties of radio sources

Extended radio sources

Radio-loud quasars (except for Blazars) and radio galaxies are observed as extended radio sources whose linear size is comparable to or greater than that of a parent galaxy ($\sim$few$\times 10$ kpc). The largest sources extend up to Mpc scale. In Figs. 1.2 and 1.3, we show an examples of the observed radio images. Extended sources are almost always characterized by two-sided or double structure. The pair of diffuse radio components are called 'radio lobes'. The emission mechanism is synchrotron, and the spectrum of the observed flux is usually well described by a power-law of form $F_\nu \propto \nu^{-\alpha}$, with $0.5 \lesssim \alpha \lesssim 1.0$.

The extended radio sources can be divided into two subclasses based on their observed

morphologies. In some cases, the lobes are edge-brightened and have a very bright compact emission regions which are called 'hot spots' near the outer surface of the lobes (Fig. 1.2). Often spots of infrared or even optical continuum emission can be seen at the same locations as the radio hot spots. In other cases, the lobes are brightest near the central regions and are edge-darkened (Fig. 1.3). Object of this class often have lobes that are bent. Based on this division, Fanaroff & Riley (1974) designated as class 1 (FRI) those radio sources for which the ratio of the distance between the two brightest spots on either side of the nucleus to the overall size was less than 0.5 and as class 2 (FRII) for those which the ratio was greater than 0.5.

Although the division was based on the morphology, Fanaroff & Riley also found an important correlation between the emitted radio power and the source morphology. FRII objects also tend to be more-luminous. The crossover point was taken as 10^{25} W Hz^{-1} sr^{-1} at a received frequency of 178 MHz. Some dependence of the location of the FRI/FRII boundary on the optical magnitude of the host galaxy has also been found (Ledlow & Owen 1996). Almost all FRII sources have luminosity at 1.4 GHz (defined as νL_ν) greater than $6\times10^{40}L_{\rm R}^2$ ergs s^{-1}, while most of FRI sources have smaller luminosities, where $L_{\rm R}$ is the R band luminosity of the host. Occasionally there are objects that fall into one class according to morphology while having a luminosity more typical of the other, but by and large the division is a fairly clean one.

FRII radio sources were the first extragalactic sources observed, and they were also the sources examined in the most details as high resolution interferometers came into operation. Because of this, they were also the sources modeled extensively by theorists, and, therefore, they became archetype radio sources. However, this is due to their high radio luminosity, and it is now well known that FRII sources are not the most common type of extended radio source by a large margin. While the luminous FRII sources dominate any flux limited sample with a fairly high flux limit, such as 3C (for 3rd Cambridge) catalog, the fainter FRI sources have much higher space density and are in fact the most common type of extended radio source. The integrated number density of FRI sources at low redshift is about 3×10^{-4} Mpc^{-3} (Urry, Padovani, & Stickel 1991), whereas a rough integration of the luminosity function for nearby FRII sources (Padovani & Urry 1992) gives 1×10^{-6} Mpc^{-3}. Thus, the nearby FRI radio sources are almost 100 times more numerous than FRII sources.

Generally, also jets can be resolved in radio. Jets takes the form of elongated low-luminosity emission regions, very aligned with the double lobe structure. They often shows bends and wiggles between the central core and the point where jet appears to expand into the extended radio structure. In FRI sources, usually jet can be seen on both side of the nucleus and connects smoothly to the outer structure. On the other hand, jet is relatively weak compared to the lobes and often tends to be asymmetric or even one-sided in FRII sources.

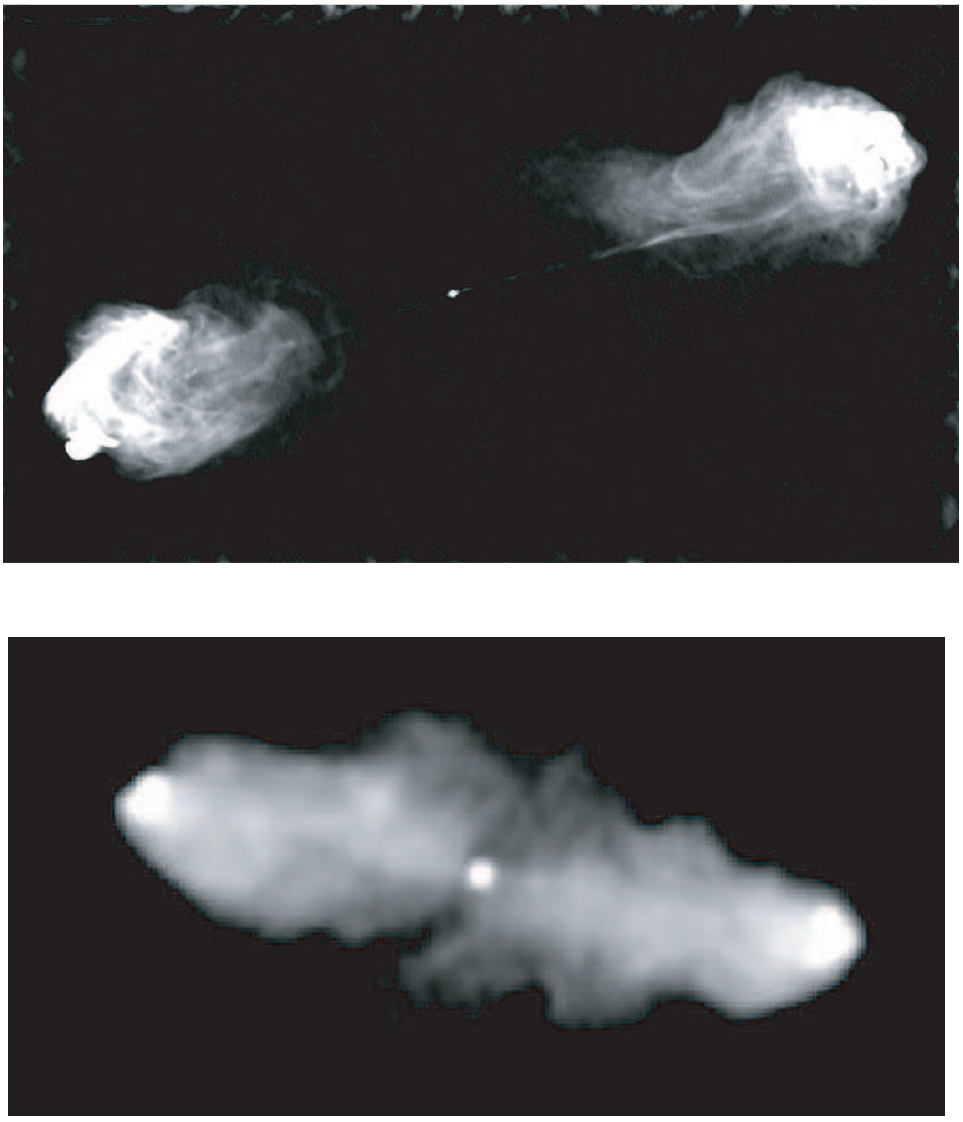

Figure 1.2: Examples of VLA radio images of FRII radio sources. *Top*: Cygnus A at 5 GHz (Perley et al. 1984); *bottom*: 3C 452 at 1.48 GHz (R. A. Laing, unpublished).

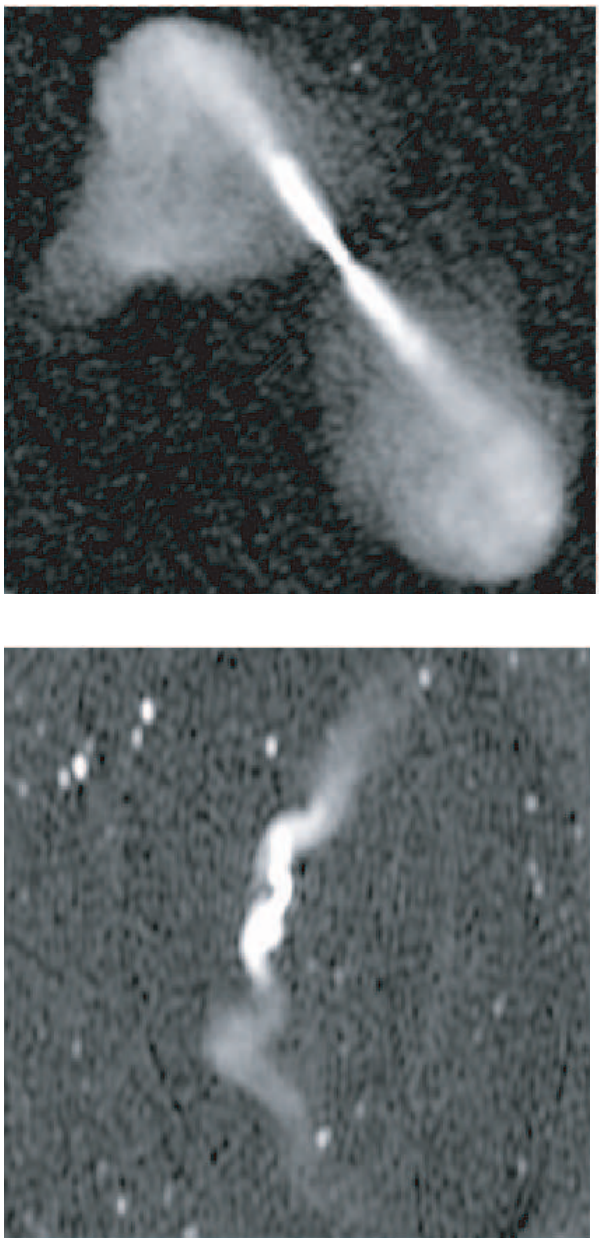

Figure 1.3: Examples of VLA radio images of FRI radio sources. *Top*: 3C 296 at 1.48 GHz (Leahy & Perley 1991); *bottom*: 3C 31 at 608 MHz (http://www.jb.man.ac.uk/atlas/object/3C31.html).

Compact radio sources

Compact radio sources in which there total size is less than that of a galaxy (i.e., typically less than few kpc) are also found by observations. Compact sources are classified on the basis of their spectral characteristics. Thus sources have been classified as Gigahertz Peaked Spectrum (GPS), and Compact Steep Spectrum (CSS) [1]. A review of the observational characteristics of these objects can be found in O'Dea (1998). GPS sources are radio sources whose spectra are inverted ($F_\nu \propto \nu^{-\alpha}$ with $\alpha < 0$) below peak (or turnover) frequencies $\nu \sim 0.5 - 10$ GHz. CSS sources are similarly inverted spectrum radio source but with peak frequencies in a lower frequency range when compare with the GPS population, $\nu \lesssim 0.5$ GHz. The GPS sources are quite small, usually less than 1 kpc in overall extent, while CSS sources are larger $\sim 1 - 20$ kpc. The radio luminosities of these objects are very high. Almost all of them are above the luminosity break that separates the FRII and FRI sources (O'Dea & Baum 1997). About $10\ \%$ of radio sources found in high-frequency radio survey belongs to the GPS sources and 30% are classified as CSS sources.

The radio morphology of CSS and GPS shows a wide variety of distributed emission. What is clear is that they are not unresolved core point sources with sub-pc length scale. An interesting morphological subclass of these objects are the compact symmetric objects (CSOs) and Medium Symmetric Objects (MSOs). CSOs are a compact sources with linear size smaller than 1 kpc whose radio morphology resembles the larger FRII radio sources (i.e., structure dominated by double-lobes and hot spots). This class of object was first identified by Phillips & Mutel (1982) but with insufficient resolution. More complete sample were presented by Wilkinson et al. (1994) and Readhead et al. (1996a,b). A similar but slightly larger class of object with linear size with $\sim 1 - 10$ kpc has been identified by Readhead et al. (1996a,b) as (MSOs). It should be noted, however, that not all GPS/CSS sources can be classified into these categories since some objects show 'core-jet' morphology with asymmetric lobes (if present at all) (e.g., Liu et al. 2007).

Concerning CSOs, two scenarios were initially proposed for the origin of their compactness. One is so-called 'frustrated scenario' in which the ambient medium is so dense that jet cannot break its way through, so sources are old and confined (van Breugel et al. 1984). The other is 'youth radio source scenario' in which CSOs are young progenitor of FRII radio sources (e.g., Phillips & Mutel 1982; Carvalho 1985; Fanti et al. 1995; Begelman 1996; Readhead et al. 1996a; O'Dea & Baum 1997). The latter scenario is strongly supported by recent observations. Two independent method: the kinematic study of hot spot separation velocities (Polatidis & Conway 2003; Gugliucci et al. 2005) and the measure of radiative age from the analysis of spectrum (Murgia et al. 1999; Murgia 2003; Orienti et al 2007); both find ages

[1] Blazars are also another class of compact radio sources which are named based on their temporal variability. However, these sources are not truly compact sources but a compact substructure of the extended radio sources (FRI/II radio sources).

of about $10^3 - 10^5$ yr, which are much shorter than the ages of FRII sources ($10^6 - 10^7$ yr). Hence, it is likely that compact sources are young counterparts of larger FRII sources.

1.2.2 Large scale dynamics

FRII sources

Standard model which explain the morphological structure of FRII radio sources was established by Scheuer (1974) and Blandford & Rees (1974). Although a large number of models has been proposed since then (e.g., Begelman & Cioffi 1989; Falle 1991; Kaiser & Alexander 1997; Bicknell et al. 1997; Kino & Kawakatu 2005), its essential features remain to the present day. Schematic illustration of the standard model is displayed in Fig. 1.4. In the model, supersonic jet is continuously emanated from the AGN. They propagate relatively unhindered (laminar jets) until they terminate in a strong shock on impact with the ambient medium. At this point the jets convert some fraction (or perhaps most) of their bulk kinetic energy into relativistic particles (via particle acceleration), and magnetic fields. These particles within the shocked jet material emits copious radio synchrotron radiation resulting in the high surface brightness radio hot spots. The high pressure shocked jet material then expands out of hot spot transversely inflating a cavity in the ambient medium. The cavity is filled with a waste-jet material and is often termed as 'cocoon'. The observed radio lobes correspond to the radio-emitting plasma within the cocoon.

The outline above applies to the radio emitting structures. A second aspect of this model is the effect of radio source on the ambient medium. The momentum flux of the jet and pressure within the cocoon are normally expected to be sufficient to drive a bow shock into the ambient medium. In the rest frame of the bow shock ambient gas is heated as it crosses the chock to fill a region between the cocoon and the bow shock. Hence, a 'shell' which envelopes the whole system is formed by the shocked ambient gas.

Significant insights into the physics of extragalactic radio sources has come through numerical simulations. The basic structure of supersonic jets, hot spots, and radio lobes were delineated in the early works of Norman et al. (1982). These hydrodynamical simulations showed the development of the double shock structure at the jet head (terminal shock and bow shock), and evolution of cocoon. A fundamental conclusion from these simulation was that well developed radio lobes, with width much larger than that of the jet, only result from very under-dense jet with a high Mach number. Another novel feature of the simulations were the existence of backflow. The jet material which has crossed the terminal shock is bent back towards the source of jet by the pressure gradient between the head region of the cocoon and the cocoon.

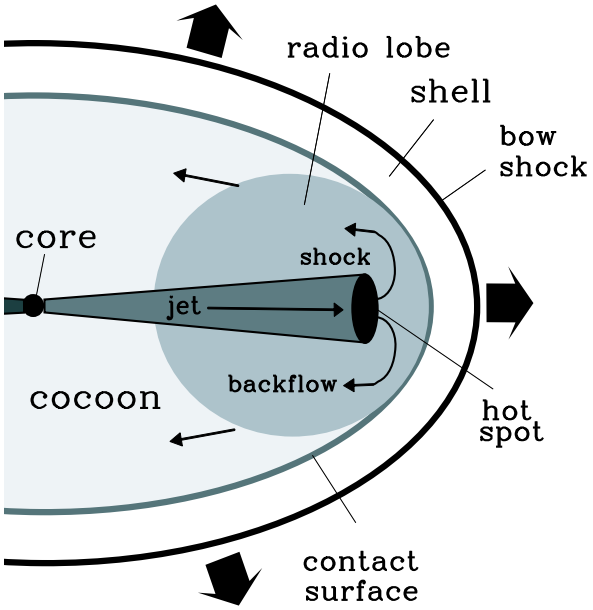

Figure 1.4: In the standard model of FRII radio sources, a supersonic jet decelerates at the terminal shock, producing a radio hot spot. Provided the shocked radio-emitting fluid forming the radio lobe has enough internal energy or momentum density to drive a leading bow shock, ambient gas will be heated as it crosses the bow shock to fill the region between the shocked jet matter and bow shock (shell).

FRI sources

While it is believed that the same basic mechanism is responsible for the generation of FRI sources and FRII sources, it appears that jets in FRI sources dissipate much of their energy without developing a well defined jet terminus. Hence, unlike FRII sources, FRI decelerate to much lower speeds within a few kpc. This is often taken to indicate that mass loading from stellar wind (Komissarov 1994; Bowman et al. 1996) or ambient gas (Bicknell 1984; De Young 1996; Rosen & Hardee 2000) is occurring in FRI jets while they propagate. As a result. the jet is driven into turbulent state.

The physics of the turbulent jet flow is far from clear, and, therefore, is difficult to model. Some insight can be gained from application of conservation laws to jet flow (Bicknell 1994; Bicknell 1995). Also, models for the velocity field, magnetic field structure and distribution of electrons can be crafted onto high resolution radio observations of the turbulent FRI sources (Laing & Bridle 2002a; Laing & Bridle 2002b; Laing & Bridle 2004). Unfortunately it is not clear how such models can be generalized to make predictions for dynamics and emission

properties of the FRI class as a whole.

In the absence of a general model for the dynamics and emission properties of FRI sources, we can only summarize a few basic facts. Generally, turbulent jets in FRI sources give rise to fainter large-scale radio structures than laminar jets in FRII sources. The main reason is the absence of an efficient acceleration site for relativistic electrons such as strong shock.

Observational evidence for the interactions between jet and ambient gas

X-ray data in the last decade provided a clear evidence for interaction of jet with surrounding ambient medium. These are the observations of X-ray cavity which is the region embedded in ISM/ICM with the suppressed X-ray surface brightness (Böhringer et al. 1993; Fabian et al. 2002; Bîrzan et al. 2004; Allen et al. 2006). X-ray cavities correspond to the region of ambient matter displaced by cocoon since the region coincide with the radio lobes of radio galaxy. Although the numbers are few, recent deep X-ray observations enabled to resolve the bow shock associated with the cavities. While most of the shocks found in clusters appears to be weak (Forman et al. 2005; Nulsen et al. 2005; Wilson et al. 2006; Fabian et al. 2006) on the other hand those found in giant elliptical galaxies are strong (Kraft et al. 2003; Croston et al. 2007), supporting the picture that the radio sources are expanding supersonically at least in the early stage.

1.3 Motivation and Outline of this Thesis

Aim of this thesis is to explore the properties of AGN jets and emissions associated with the large scale structure formed via interaction between the jet and the ambient medium. To do this, we use analytical model which describes the large scale dynamics of cocoon inflated by the jet. This thesis is organized as follows:

Chapter 2 The models which we will use in chapters 3, 4, and 5 is explained in detail. First, we introduce the model which describes the two-dimensional expansion of cocoon inflated powerful jet in FRII radio sources. Second, by approximating the cocoon expansion as spherical, the model for expanding shell composed of shocked ambient medium which envelopes the cocoon is presented.

Chapter3 We investigate the total kinetic powers ($L_{\rm j}$) and ages ($t_{\rm age}$) of jets in FRII radio galaxies by comparison of the model of expanding cocoons with the observed morphologies of the radio sources. We select four bright FRII radio galaxies (Cygnus A, 3C 223, 3C 284, and 3C 219) as a sample, for which the mass-density profiles of surrounding intracluster medium (ICM) are known in the literature.

Chapter 4 The thermal particles within the cocoon is explored. Particularly, we focus on the evolution of temperature and number density of relativistic particles (electrons and positrons). From the obtained result, we evaluate the thermal emissions from the cocoon.

Chapter 5 We investigate the emissions from the shell. Thermal bremsstrahlung and synchrotron are are calculated from the dynamics. We evaluate the dynamical feedbacks from thermal bremsstrahlung radiation and the spectrum of synchrotron emissions from the non-thermal electrons accelerated by the bow shock. We also discuss how the observation of synchrotron emission can be used as a probe for the physics of electron acceleration.

Chapter 6 Conclusions based on the results presented in chapters 3, 4 and 5 are given.

Chapter 2

ANALYTICAL MODELS FOR RADIO SOURCES

In this chapter, we present two models which we use to explore properties of relativistic jets. First, we show the model which describes the dynamics of cocoons in FRII radio sources in §2.1. Next, we show the model which describes the evolution of the shells enveloping the cocoon in §2.2.

2.1 Model for Cocoons in FRII Radio Sources

Here we deal with the cocoon dynamics in FRII radio sources. The adopted basic equations are almost the same as those in Kino & Kawakatu (2005) (Hereafter KK05) which extended the study of Begelman & Cioffi (1989) (Hereafter BC89). The modifications are described in §2.1.2.

2.1.1 Basic assumptions

Our main assumptions are as follows;

(i) we limit our attention on a jet with relativistic speed;
(ii) the jet supplies a constant kinetic power in time;
(iii) we focus on the over-pressured cocoon phase;
(iv) we assume that the magnetic fields are passive and ignore their dynamical effect.

For (i), although it is still under debate, some jets are suggested to be relativistic (e.g., Tavecchio et al. 2000; Celotti et al. 2001). Since little is known about the evolution of $L_{\rm j}$, the assumption (ii) is adopted as a first-step working hypothesis. The assumption of (iii) is automatically guaranteed by the sideways expansion of the cocoon (e.g., Cioffi & Blondin 1992). The assumption of (iv) is based on the results that a multi-frequency analysis of radio galaxies show that the energy density of magnetic field tend to be smaller than that of non-thermal electrons (e.g., Leahy & Gizani 2001; Isobe et al. 2002)

2.1.2 Basic equations

Based on BC89 and KK05, we briefly summarize the cocoon model we employ in the following. The model parameters are the kinetic power of jet $L_{\rm j}$ and source age $t_{\rm age}$. The unknown physical quantities are $v_{\rm h}$, $v_{\rm c}$, $P_{\rm c}$, and $A_{\rm h}$, which are the advance velocity of cocoon head, the velocity of cocoon sideways expansion, the pressure of cocoon the cross-sectional area of the head part of cocoon, respectively. We approximately describe the expansion of cocoon by the following three equations: (2.1) the equation of the motion along the jet axis, (2.2) the equation for the sideways expansion, and (2.3) the energy equation. They are expressed, respectively, as

$$\frac{L_{\rm j}}{c} = \rho_{\rm a}(r_{\rm h}) v_{\rm h}^2(t) A_{\rm h}(t), \tag{2.1}$$

$$P_{\rm c}(t) = \rho_{\rm a}(r_{\rm c})\, v_{\rm c}(t)^2, \tag{2.2}$$

$$\frac{d}{dt}\left(\frac{P_{\rm c}(t)V_{\rm c}(t)}{\hat{\gamma}_{\rm c}-1}\right) + P_c(t)\frac{dV_{\rm c}(t)}{dt} = 2L_{\rm j}, \tag{2.3}$$

where $\rho_{\rm a}$ and $\hat{\gamma}_{\rm c}$ are the density of ambient medium and the specific heat ratio of plasma inside cocoon, respectively. Throughout this paper, we assume $\hat{\gamma}_{\rm c} = 4/3$ since cocoon is expected to be dominated by relativistic particles. The cocoon shape is approximated as a rotational ellipsoid, and its volume is given as $V_{\rm c}(t) = 4/3\pi r_{\rm c}(t)^2 r_{\rm h}(t)$, where the distance from the jet apex to the hot spot and the radius of cocoon body are obtained from $r_{\rm h}(t) = \int_{t_{\rm min}}^{t} v_{\rm h}(t')dt'$ and $r_{\rm c}(t) = \int_{t_{\rm min}}^{t} v_{\rm c}(t')dt'$, respectively, and $t_{\rm min}$ is the initial time of source evolution. The mass density of ambient medium, $\rho_{\rm a}$, is assumed to be given by $\rho_{\rm a}(r) = \bar{\rho}_{\rm a}(r/r_0)^{-\alpha}$, where r_0 and $\bar{\rho}_{\rm a}$ are the reference position and the ambient mass density at r_0, respectively. A cartoon of the cocoon model is illustrated in Fig. 2.1. In this paper, we have slightly improved the model of BC89 and KK05 as follows: (i) the more accurate geometrical factor is employed in $V_{\rm c}$, and (ii) the PdV work done by the cocoon expansion is taken into account.

The model parameters are $L_{\rm j}$ and t, and the unknown physical quantities are $v_{\rm h}$, $v_{\rm c}$, $P_{\rm c}$, and $A_{\rm h}$. Since the numbers of the unknown quantities are four, while those of basic equations are three, an additional condition is required for the system of equations to be closed. Here we assume that the cross sectional area of cocoon body $A_{\rm c} = \pi r_{\rm c}^2$ is given by $A_{\rm c}(t) \propto t^X$ and treat X as a free parameter. Once the value of X is determined we obtain $v_{\rm h}$, $v_{\rm c}$, $P_{\rm c}$, and $A_{\rm h}$ as a function of $L_{\rm j}$ and t. It is worth noting that the model is capable of producing various dynamics by tuning the value of X. For example, in Kawakatu & Kino (2006), the results of 2D relativistic hydrodynamical simulations by Scheck et al. (2002) was reproduced fairly well.

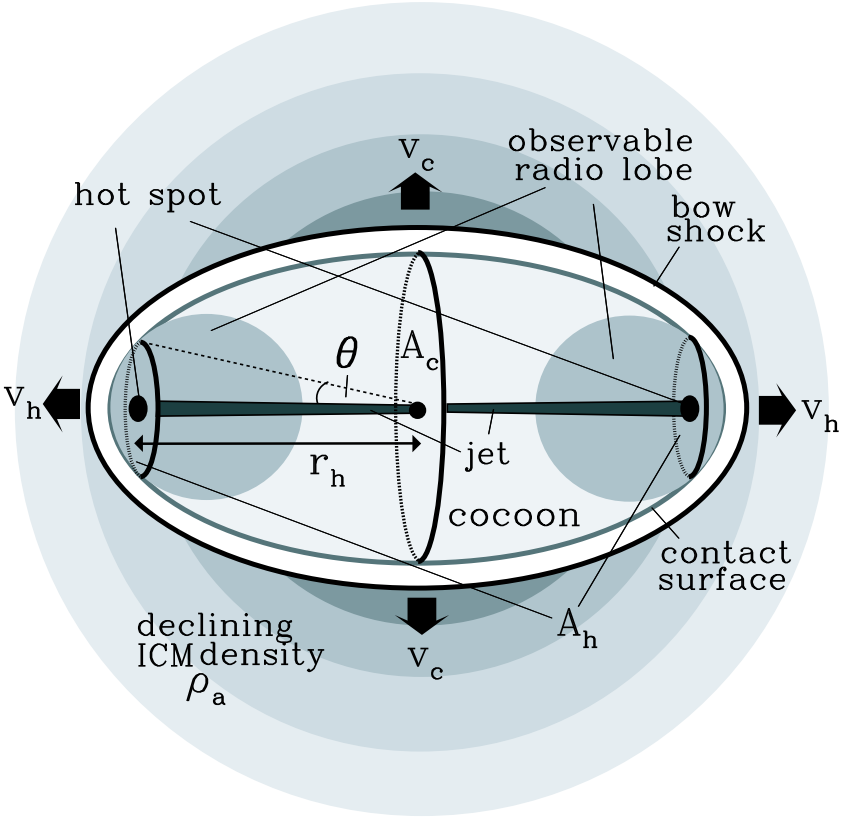

Figure 2.1: A cartoon of the employed model. The relativistic jet from FR II radio galaxy interact with ambient medium. Most of the kinetic energy of jet is deposited in the cocoon, which is then inflated by the internal energy.

2.1.3 Analytical solution

We assume that the physical quantities have a power-law time-dependence of the form $A = \bar{A}\,(t/t_{\rm age})^Y$ where Y is an arbitrary index. Hence the index and coefficient of $v_{\rm c}$, for example, is determined as

$$v_{\rm c}(t) = \bar{v}_{\rm c}\left(\frac{t}{t_{\rm age}}\right)^{0.5X-1} = \frac{\bar{A}_{\rm c}^{1/2}}{t_{\rm age}}\mathcal{C}_{\rm vc}\left(\frac{t}{t_{\rm age}}\right)^{0.5X-1}. \tag{2.4}$$

With this, by setting r_0 to be $r_{\rm h}(t_{\rm age})$, we obtain the following analytical form of cocoon quantities: from Eqs. (2.1)-(2.3):

$$P_{\rm c}(t) = \bar{\rho}_{\rm a}\bar{v}_{\rm c}^2\mathcal{C}_{\rm pc}\left(\frac{\bar{v}_{\rm c}}{v_0}\right)^{-\alpha}\left(\frac{t}{t_{\rm age}}\right)^{X(1-0.5\alpha)-2}, \tag{2.5}$$

$$v_{\rm h}(L_{\rm j},t) = \frac{L_j}{\bar{\rho}_{\rm a}\bar{v}_c^2\bar{A}_{\rm c}}\mathcal{C}_{\rm vh}\left(\frac{\bar{v}_{\rm c}}{v_0}\right)^{\alpha}\left(\frac{t}{t_{\rm age}}\right)^{X(-2+0.5\alpha)+2}, \tag{2.6}$$

$$A_{\rm h}(L_{\rm j},t) = \frac{L_{\rm j}}{v_{\rm j}\bar{\rho}_{\rm a}\bar{v}_{\rm h}^2}\mathcal{C}_{\rm ah}\left(\frac{\bar{v}_{\rm h}}{v_0}\right)^{\alpha}\left(\frac{t}{t_{\rm age}}\right)^{X(\alpha-2)(-2+0.5\alpha)+3\alpha-4}, \tag{2.7}$$

where $\mathcal{C}_{\rm vh} = 0.75(\hat{\gamma}_c-1)(0.5X)^{-\alpha}[3-(2-0.5\alpha)X]/[X(-1+0.5\alpha)(\hat{\gamma}_c-1)+3\hat{\gamma}_c-2]$, $\mathcal{C}_{\rm vc} = 0.5X/\pi^{1/2}$, $\mathcal{C}_{\rm pc} = (0.5X)^{\alpha}$, and $\mathcal{C}_{\rm ah} = [X(-2+0.5\alpha)+3]^{-\alpha}$, and $v_0 \equiv r_{\rm h}(t_{\rm age})/t_{\rm age}$ corresponds to the head speed assumed to be constant in time. The difference in $\mathcal{C}_{\rm vh}$ obtained here from that in KK05 is due to the correction made in the Eq. (2.3). We assume the conditions of $0.5X > 0$ and $X(-2+0.5\alpha)+3 > 0$, which ensure the contribution at $t_{\rm min}$ in the integrations of $r_{\rm h}$ and $r_{\rm c}$ is small enough. The cases we focus on in §3 and §4 clearly satisfy these conditions.

2.1.4 Determination of X

As mentioned in §2.1.2, an additional condition that determines the free parameter X is required for the system of equations to be closed. In the pioneering study of BC89, $A_{\rm h}(t) = {\rm const}$ was assumed. However, as can be confirmed from numerical simulations (e.g., Cioffi & Blondin 1992; Scheck et al. 2002), it is obvious that this condition is unlikely to hold for long-term evolutions from pc to Mpc scales. Here we consider the following two conditions, which seem more reasonable and equally possible, in determining X:

Constant aspect ratio

The aspect ratio of cocoon, $\mathcal{R} = r_{\rm c}/r_{\rm h}$, is assumed to be constant in time. This corresponds to the widely-discussed self-similar evolution (Begelman 1996; Komissarov & Falle 1997; Kaiser & Alexander 1997; Bicknell et al. 1997). Since the time dependence of $\mathcal{R}$ is given by $\mathcal{R}(t) \propto t^{[X(2.5-0.5\alpha)-3]}$, we obtain $X = 6/(5-\alpha)$ in this case.

Constant opening angle

The opening angle, $\theta = \tan^{-1}(A_{\rm h}^{1/2}/\pi^{1/2}r_{\rm h})$ (see Fig. 2.1), is assumed to be constant in time. Although there has been no previous work that has employed this condition, it seems to be reasonable when the jet is precessing with a constant pitch angle. Since the time dependence of $\tan\theta$ is given by $\tan\theta(t) \propto t^{[0.25X(\alpha-4)^2+1.5\alpha-5]}$, $X = (20-6\alpha)/(4-\alpha)^2$ is obtained for this case.

It should be noted, however, that these two independent conditions lead to the solutions that describe quite similar dynamical evolutions for the range of α we focus in §3 and §4 ($1 \leq \alpha \leq 2$). This can be seen as follows. If the constant opening angle is imposed (Case II), the evolution of the aspect ratio is obtained as $\mathcal{R}(t) \propto t^{(2-\alpha)/(4-\alpha)^2}$. It is easy to confirm its very weak time dependence, since the power-law index is limited to the range $0 \leq (2-\alpha)/(4-\alpha)^2 \leq 1/9$. Just in the same way, if the constant aspect ratio is adopted (Case I), we find again a very weak time dependence of the opening angle, $\tan\theta(t) \propto t^{(\alpha-2)/[2(5-\alpha)]}$, with the power-law index being $-1/8 \leq (\alpha-2)/[2(5-\alpha)] \leq 0$.

2.2 Model for Shells in Radio Sources

In this section, we consider the evolution of shell composed of shocked ambient gas.

2.2.1 Basic assumptions

As in the model presented previously in §2.1, we focus on the phase when the cocoon is overpressured with respect to the ambient gas. It should be noted that this corresponds not only to powerful FRII radio sources but also to the early stage of FRI radio sources (Kraft et al. 2003; Croston et al. 2007; Kraft et al. 2007; Perucho & Martí 2007). We also adopt assumptions (ii) and (iv) given in §2.1.1. In addition, we approximate the cocoon as sphere with a radius of R ($r_{\rm h} = r_{\rm c} = R$) for the sake of simplicity. This assumption will not cause a significant error as long as axial ratio is moderate. (e.g., ∼0.5-0.7 for Cygnus A, see Wilson

et al. 2006). Also we assume that the width of the shell, δR, is thin with respect to the radius of cocoon ($\delta R \ll R$). Hence, we ignore the difference between the radius of bow shock and contact surface when considering the dynamics of the expanding cocoon. This assumption is valid whenever the expansion velocity has a high Mach number, namely when the shock is strong. It is worth to note that this is also confirmed in the numerical simulations (e.g. Reynolds et al. 2001). A cartoon of the cocoon model is illustrated in Fig. 2.2.

2.2.2 Basic equations

Under the assumptions given in §2.2.1, Under these assumptions, we approximately describe the system of expanding of cocoon and shell by the following equations: (2.8) the equation of motion of the swept-up matter in the shell and (2.9) the energy equation. They are expressed, respectively, as

$$\frac{d}{dt}\left(M_{\rm s}(t)\dot{R}(t)\right) = 4\pi R(t)^2 P_{\rm c}(t), \tag{2.8}$$

$$\frac{d}{dt}\left(\frac{P_{\rm c}(t)V_{\rm c}(t)}{\hat{\gamma_{\rm c}}-1}\right) + P_c(t)\frac{dV_{\rm c}(t)}{dt} = L_{\rm j}, \tag{2.9}$$

where $\dot{R} \equiv dR/dt$ and $M_{\rm s}$, are the expansion velocity of the cocoon and the swept up mass within the shell, respectively. Note that Eq. (2.9) is identical to Eq. (2.3). Only the difference is that here we slightly change the definition of $L_{\rm j}$ as the total kinetic energy released by the pair of jets emanating in opposite direction merely for convenience. Hence, by replacing $L_{\rm j}$ in Eq. (2.9) to $2L_{\rm j}$, we obtain Eq. (2.3). As in §2.1, the mass density of the ambient medium, $\rho_{\rm a}$, is assumed to be given by $\rho_{\rm a}(r) = \rho_0(r/r_0)^{-\alpha}$, where r_0 and ρ_0 are the reference position and the mass density at r_0, respectively. The swept up mass of shell is given by $M_{\rm s} = \int_0^R 4\pi r'^2 \rho_{\rm a}(r')dr'$.

2.2.3 Analytical solution

Contrary to the model shown in §2.1, since the unknown physical quantity are two (R and $P_{\rm c}$), Eqs. (2.8) and (2.3) can be solved analytically without imposing an additional assumption. The obtained solution of R is given as

$$R(t) = C_R\, {r_0}^{\alpha/(\alpha-5)} \left(\frac{L_{\rm j}}{\rho_0}\right)^{1/(5-\alpha)} t^{3/(5-\alpha)}, \tag{2.10}$$

where C_R is a function of α and $\hat{\gamma_{\rm c}}$ which is given as

$$C_R = \left[\frac{(3-\alpha)(5-\alpha)^3(\hat{\gamma_{\rm c}}-1)}{4\pi\{2\alpha^2+(1-18\hat{\gamma_{\rm c}})\alpha+63\hat{\gamma_{\rm c}}-28\}}\right]^{1/(5-\alpha)}. \tag{2.11}$$

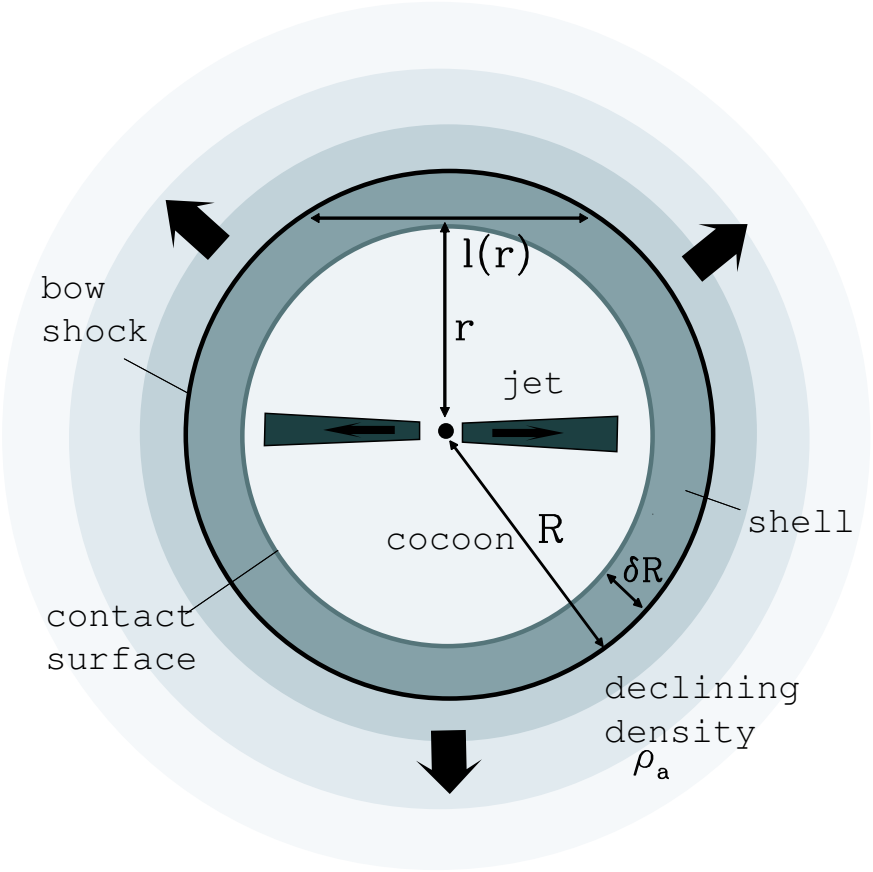

Figure 2.2: A geometry of the model for the shell. The relativistic jet from AGN interact with ISM/ICM, and overpressured cocoon drives a strong shock into the ambient medium.

Similarly, $P_{\rm c}$ is obtained as

$$P_{\rm c}(t) = \frac{3(7-2\alpha)}{(5-\alpha)^2(3-\alpha)} C_R^{(2-\alpha)/(5-\alpha)} {r_0}^{3\alpha/(5-\alpha)}\ {\rho_0}^{3/(5-\alpha)}\ L_{\rm j}^{(2-\alpha)/(5-\alpha)}\ t^{(\alpha+4)/(\alpha-5)}. \quad (2.12)$$

2.2.4 Evolution of shell

By assuming that the density, $\rho_{\rm s}$, and pressure, $P_{\rm s}$ is uniform within the shell, we estimate the evolution of the shell from the obtained solutions. Since we focus on the shell expanding with

high Mach number, $\rho_{\rm s}$ and $P_{\rm s}$, are determined by

$$\rho_{\rm s}(t) = \frac{\hat{\gamma}_{\rm a}+1}{\hat{\gamma}_{\rm a}-1}\rho_0 \left(\frac{R(t)}{r_0}\right)^{-\alpha}, \quad P_{\rm s}(t) = \frac{2}{\hat{\gamma}_{\rm a}+1}\rho_0 \left(\frac{R(t)}{r_0}\right)^{-\alpha} \dot{R}(t)^2, \tag{2.13}$$

where $\hat{\gamma}_{\rm a}$ is the specific heat ratio of ambient medium. In the above equations we have used the strong shock jump conditions in non-relativistic limit (Landau & Lifshitz 1959). When considering thermal radiation from the shell, temperature, $T_{\rm s}$, must be specified. By introducing an equation of state for ideal gas, the temperature of the shell, $T_{\rm s}$ is obtained as

$$k_{\rm B}T_{\rm s}(t) = \frac{2(\hat{\gamma}_{\rm a}-1)\mu m_{\rm H}}{(\hat{\gamma}_{\rm a}+1)^2}\dot{R(t)}^2, \tag{2.14}$$

where $k_{\rm B}$ and $\mu m_{\rm H}$ are the Boltzmann constant and the mean mass per particle of ambient medium, respectively.

The width of shell is estimated from the conservation of mass. By equating the swept-up mass with the total mass within the shell ($4\pi R^2 \delta R \rho_{\rm s} \simeq M_{\rm s}$), δR is given as

$$\frac{\delta R(t)}{R(t)} = \frac{\hat{\gamma}_{\rm a}-1}{(\hat{\gamma}_{\rm a}+1)(3-\alpha)}. \tag{2.15}$$

It can be seen that ratio of δR and R does not depend on time. Validity of the assumption $\delta R \ll R$ can be confirmed from the above equation by substituting plausible values in $\hat{\gamma}_{\rm a}$ and α. For example, when we assume $\alpha = 0$ and $\hat{\gamma}_{\rm a} = 5/3$, $\delta R/R = 1/12$ is obtained.

From Eqs. (2.13) and (2.10), the total internal energy stored in shell, $E_{\rm s}$, is obtained as

$$E_{\rm s} = f L_{\rm j} t, \tag{2.16}$$

where

$$f = \frac{18(\hat{\gamma}_{\rm c}-1)(5-\alpha)}{(\hat{\gamma}_{\rm a}+1)^2[2\alpha^2+(1-18\hat{\gamma}_{\rm c})\alpha+63\hat{\gamma}_{\rm c}-28]}. \tag{2.17}$$

From the above equations, it can be seen that a constant fraction f of total energy released by jet $L_{\rm j}t$ is converted to internal energy of the shell. Assuming $\hat{\gamma}_{\rm c} = 4/3$, $\hat{\gamma}_{\rm a} = 5/3$, f is a weak function of α. $f \simeq 0.1$ is obtained in the range of $0 \leqq \alpha \leqq 2$.

Chapter 3

COCOON DYNAMICS AS CALORIMETER OF AGN JETS

The total kinetic powers of AGN jets $L_{\rm j}$ is one of the most basic physical quantities characterizing the jet. A lot of authors have investigated $L_{\rm j}$ in various ways so far (e.g., Rawlings & Saunders 1991; Celotti & Fabian 1993; Willot et al. 1999). It is, however, difficult to estimate $L_{\rm j}$, since most of the observed emissions from AGN jets are of non-thermal electron origin, and it is hard to detect the electromagnetic signals from the thermal and/or proton components. Hence, the free parameter describing the amount of the invisible plasma components always lurks in the estimates of $L_{\rm j}$ based on the non-thermal emissions.

To conquer this difficulty, KK05 proposed a new method for estimating $L_{\rm j}$ of FR II radio galaxies by using the dynamical model of cocoon expansions. In their study, $L_{\rm j}$ and $t_{\rm age}$ are derived from the comparison of the cocoon model with the morphology of the cocoon obtained from radio observations. So far, however, this estimate of $L_{\rm j}$ has been applied only to Cygnus A. The expansion of the number of samples is evidently crucially important for exploring general characteristics of the powerful AGN jets.

In this chapter, we investigate the kinetic powers ($L_{\rm j}$) and ages ($t_{\rm age}$) of powerful jets in FR II radio galaxies based on their dynamics by using the model we have introduced in the previous chapter (§2.1) which is improved from that of KK05. We select four FR II radio sources (Cygnus A, 3C 223, 3C 284, and 3C 219), for which the mass-density profiles of intracluster medium (ICM) are known in the literature. It is stressed that the 'total' kinetic power can be constrained by this method since all particles contribute to the dynamics. In the following analysis, we assume constant aspect ratio $\mathcal{R}(t) = {\rm const}$ for the evolution of the cocoon in our model (see §2.1.4).

3.1 Extraction of the Key Quantities from the Observations

In determining $L_{\rm j}$ and $t_{\rm age}$, we essentially follow the same procedure taken in KK05. In this section, we explain in detail how to extract the key quantities utilized in the model from the observations.

3.1.1 ICM quantities

As for the mass-density profiles ($\rho_{\rm a}(r)$ and α) and pressures ($P_{\rm a}(r)$) of ICM, we adopt the values given in the literature (Reynolds & Fabian 1996; Smith et al. 2002 for Cygnus A, Croston et al. 2004 for 3C 223 and 3C 284, and Hardcastle & Worrall 1999 for 3C 219). In these papers, the X-ray surface brightness distribution of ICM was fitted by the isothermal β-model, which takes the form of $\rho_{\rm a}(r) = \rho_{\rm core}[1 + (r/r_{\rm core})^2]^{-3\beta/2}$ (Cavaliere & Fusco-Femiano 1978), where $\rho_{\rm core}$ and $r_{\rm core}$ are the core radius and density of the ICM, respectively. Since we employ the density profile of $\rho_{\rm a}(r) = \rho_{\rm a}(r_{\rm h})(r/r_{\rm h})^{-\alpha}$, a power-law approximation approximation of the β-model is necessary. The determination of $\rho_{\rm a}(r_{\rm h})$ is done simply by equating it with the density in the β-model at the corresponding radius $r_{\rm h}$, namely $\rho_{\rm core}(r_{\rm h}) = \rho_{\rm core}[1 + (r_{\rm h}/r_{\rm core})^2]^{-3\beta/2}$. In the case of $r_{\rm h} \gg r_{\rm core}$, it is clear that α can be approximated by 3β. However, only Cygnus A satisfies this condition. For the rest of the sources, $r_{\rm h}$ is comparable to $r_{\rm core}$: $r_{\rm core} \sim$ 340 kpc, 210 kpc, and 90 kpc for 3C 223, 3C 284, and 3C 219, respectively. It is obvious that the above approximation of $\alpha \approx 3\beta$ would cause an over estimation of density gradient in this case. Instead α should be taken to be a typical value in the ICM region swept by the expanding cocoon. Here we require that $\rho_{\rm a}$ coincide with the density in the β-model at $r = 0.5r_{\rm h}$ in addition to $r = r_{\rm h}$. Although there is no compelling reason for this choice, the estimations of $L_{\rm j}$ and $t_{\rm age}$ are affected little by this uncertainty. Once $\rho_{\rm a}$ is given, $P_{\rm a}$ is obtained by the equation of state, which is written as $P_a(r) = \frac{k_B T_{\rm a}}{\mu m_{\rm H}}\rho_a(r)$, where $T_{\rm a}$ and $\mu = 0.6$ are the temperature of and the mean molecular weight of ICM, respectively, and $m_{\rm H}$ is the mass of hydrogen. As in the β-model, we do not consider radial dependence for $T_{\rm a}$, and adopt the same temperature used in the model. In Table 3.1, we list the values of $\rho_{\rm a}(r_{\rm h})$, $P_{\rm a}(r_{\rm h})$, and α for each source.

3.1.2 $r_{\rm h}$ and $A_{\rm h}$

In Fig. 3.6, we show the VLA images of Cygnus A (Perley et al. 1984), 3C 223 (Leahy & Perley 1991), 3C 284 (Leahy et al. 1986), and 3C 219 (Clarke et al. 1992) in logarithmic scale. Contours in linear scale are also displayed to determine the position of hot spot accurately. The overlaid straight lines that cross each other at right angle on the hot spot are the lines we use to measure $r_{\rm h}$ and $A_{\rm h}$. For simplicity, we neglect the projection effect of $r_{\rm h}$, which would be at most a factor of a few if we believe the unified model of AGN (Urry & Padovani 1995). Moreover, even for $\theta \sim \pi/4$, $L_{\rm j}$ is decreased by a factor of $1/4$, and $t_{\rm age}$ is increased only by a factor of $2^{3/2}$. $r_{\rm h}$ and $A_{\rm h}$ for each source are summarized in Table 3.1.

In the above procedure, $A_{\rm h}$ is measured as a cross-sectional area of the radio lobe at the position of the hot spot. It is stressed that the plasma just around the hot spot is very fresh in sense that it directly traces the detailed shape of cocoon head without any significant synchrotron cooling. Therefore, we can safely determine $A_{\rm h}$ this way from Fig. 3.6 with little

Table 3.1: The quantities measured from observations.

Source (1)	$r_{\rm h}$ (kpc) (2)	$A_{\rm h}$ (kpc^2) (3)	$\rho_{\rm a}$ (g cm^{-3}) (4)	$P_{\rm a}$ (dyne cm^{-2}) (5)	α (6)	Ref. (7)
Cygnus A E	60	150	8.3×10^{-27}	8.0×10^{-11}	1.5	1,2
Cygnus A W	70	150	6.6×10^{-27}	6.4×10^{-11}	1.5	1,2
3C 223 N	340	4300	5.5×10^{-28}	1.2×10^{-12}	1.6	3
3C 223 S	340	1800	5.5×10^{-28}	1.2×10^{-12}	1.6	3
3C 284 E	260	4600	4.0×10^{-28}	6.4×10^{-13}	1.0	3
3C 284 W	380	6200	2.3×10^{-28}	3.7×10^{-13}	1.4	3
3C 219 W	210	5000	1.0×10^{-27}	1.6×10^{-12}	2.0	4

Note. —Column (1) shows the names of radio sources, and the following alphabet distinguishes the pair of jets (see Fig. 3.6). Columns (2) and (3) display, respectively, the cocoon lengths and the cross sectional areas of cocoon head measured from Fig. 3.6 . Columns (4) and (5) give the estimated ICM densities and pressures at $r = r_{\rm h}$. In Column(6), the estimated power-law indexes of the ICM density are presented. References for the density profiles and pressures are listed in column (7)

References. — (1)Reynolds & Fabian (1996); (2)Smith et al. (2002); (3)Croston et al. (2004); (4)Hardcastle & Worrall (1999).

ambiguity.

Next we address the issue determining $A_{\rm h}$ that arises from multiple hot spots. Double hot spots are actually observed in the radio lobes of Cygnus A (see, e.g., Carilli & Barthel 1996). In determining $A_{\rm h}$, we adopt the "disconnected-jet" model by Cox et al. (1991) to Cygnus A. The double hot spots are referred to as primary and secondary as follows. The primary hot spot is more compact and located in the inner part of the lobe, whereas the secondary spot is more diffuse and brighter and located in the outer part of the lobe. According to the disconnected-jet model, double hot spots are produced by the sudden change of the jet-orientation, or the disconnection, which leads the termination of energy supply to the original shock and the generation of a new jet. While the primary hot spot is produced by the terminal shock in the new jet, the secondary hot spot remains as a relic in the original jet. The schematic picture of the model is illustrated in Fig. 3.1. Since the primary hot spot is younger than the source age in this model, we employ the position of the secondary hot spot to determine $A_{\rm h}$. We will discuss this point in the following paragraphs.

The age of Cygnus A is the order of $t_{\rm age} \approx r_{\rm h}/\beta_{\rm hs}c \approx 2.0 \times 10^7(\beta_{\rm hs}/10^{-2})^{-1}$ yr, where $\beta_{\rm hs}c$ is the advance velocity of the hot spot. On the other hand, the age of the primary hot spot is $t_{\rm age} - t_{\rm disconn}$, where $t_{\rm disconn}$ is the time when disconnection has occurred. Since the primary hot spot is observed simultaneously with the secondary hot spot, it should be younger than the duration, $t_{\rm dur}$, in which the secondary spot is bright. $t_{\rm dur}$ is expressed as a sum of the time, $t_{\rm dis}$,

up to the shut off of the energy feed to the spot and the cooling time, $t_{\rm cool}$:

$$t_{\rm dur} = t_{\rm dis} + t_{\rm cool} \approx \max(t_{\rm dis}, t_{\rm cool}). \tag{3.1}$$

The cooling time is evaluated as $t_{\rm cool} = \min(t_{\rm syn}, t_{\rm ad})$, where $t_{\rm syn}$ and $t_{\rm ad}$ are the synchrotron cooling timescale and the adiabatic expansion timescale, respectively. A typical value of $t_{\rm syn}$ at the hot spot is estimated as $t_{\rm syn} \approx 1.0 \times 10^6 (B/10^{-4}{\rm G})^{-3/2} (\nu/1\ {\rm GHz})^{-1/3}$ yr, whilst $t_{\rm ad}$ is given by $t_{\rm ad} \approx r_{\rm hs}/c_{\rm s} = 5.6 \times 10^3 (r_{\rm hs}/1{\rm kpc})$ yr, where $r_{\rm hs}$ and $c_{\rm s} = c/\sqrt{3}$ are the size of the hot spot and the sound speed, respectively. These estimates lead to $t_{\rm cool} = t_{\rm ad}$ for the secondary hot spot. On the other hand, $t_{\rm dis}$ is given by $t_{\rm dis} = r_{\rm dis}/v_{\rm j}$ where $r_{\rm dis}$ is the distance from the tail to the hot spot in the disconnected jet. Although we do not know $r_{\rm dis}$ from observations, we can at least put the upper limit as $r_{\rm h} > r_{\rm dis}$. We then obtain $t_{\rm dis} < 2.0 \times 10^5 (r_{\rm h}/60\ {\rm kpc})(v_{\rm j}/c)^{-1}$ yr. From Eq. (3.1), we see that $t_{\rm dur}$ is in the range $\sim 5 \times 10^3$ - 2×10^5 yr. From these estimates, it is obtained that the age of the primary hot spot only makes up a small fraction of its whole lifetime. Therefore, we adopt the secondary spot for determination of $A_{\rm h}$, which reflects the whole evolution of the cocoon (Fig. 3.6).

3.1.3 $\mathcal{R}$

In contrast with $r_{\rm h}$ and $A_{\rm h}$, it is hard to measure the aspect ratio of cocoon, $\mathcal{R}$, from the VLA radio images, since the cocoon emission from the region far away from the hot spot is very dim at GHz frequency because of the synchrotron cooling (see Fig. 3.6). It is well known that this cooling effect can be used to infer the age of radio galaxy (the spectral ageing method, e.g., Carilli et al. 1991). So far little attention has been paid to observational features of the cocoons identified as the remnants of exhausted jet. A few authors have reported the existence of prolate cocoon, based on the observation at the relatively low radio frequency, 610 MHz band (e.g., Readhead et al. 1996). Indeed, the lower frequency image we utilize, the fatter the cocoon is expected to become, since lower-energy electrons have longer synchrotron cooling times (e.g., Carilli and Barthel 1996).

On the other hand, theoretical studies of jet propagation and cocoon formation with multi-dimensional hydrodynamic simulations clearly support the existence of cocoon for reasonably light beams going through surrounding ICM (Scheck et al. 2002; Aloy et al. 2000; Gomez et al. 1997; Komissarov & Falle 1997; Mioduszewski 1997). The intensity maps of the synchrotron emissivities obtained in these hydrodynamical simulations well reproduce the double lobe structures as observed (e.g., Fig. 10 of Scheck et al. 2002). Therefore, it seems natural to suppose that the cocoon is commonly produced although there is a room for further observational investigations. In the present study, we explore a wide range of $0.5 < \mathcal{R} < 1$ in order to take account of the large ambiguity on the shape of cocoon. It is worthwhile to note in this respect that the existence of cocoon can be confirmed for Cygnus A in the Chandra image

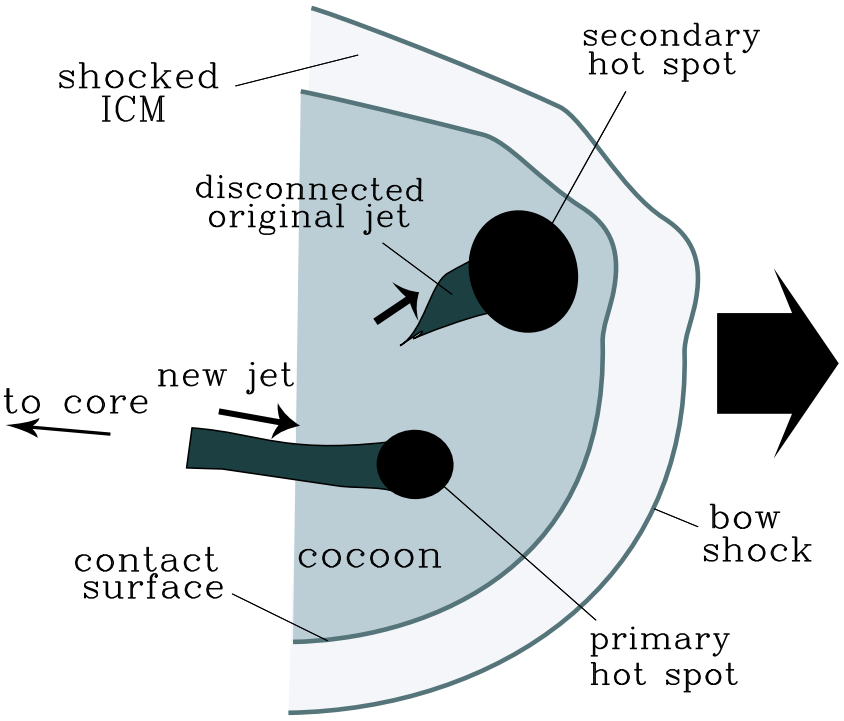

Figure 3.1: A cartoon around the double hot spots in the "disconnected-jet" model. As a result of altering orientation, jet becomes disconnected and forms the primary and the secondary hot spot which are the location of the present and the previous terminal shock, respectively.

(Wilson et al. 2000; Wilson et al. 2006) and that the obtained aspect ratio $\sim 0.5 - 0.7$ lies within the considered range.

3.2 Results

3.2.1 Total kinetic power and dynamical age

The resultant $L_{\rm j}$ and $t_{\rm age}$ are displayed in Figs. 3.2-3.5. Since most of the radio sources show asymmetries in the pair of lobes, we analyze each lobe independently. Three oblique lines in these figures are the obtained $L_{\rm j}$ and $t_{\rm age}$ for different α's, and their ranges reflect the uncertainty in $\mathcal{R}$. The thick solid line shows the result for the parameter set listed in Table 3.1. The other two lines correspond to the results obtained by varying α by $\pm$0.5. From the figures, it is confirmed that the results are rather insensitive to the value α. In each line, the power and age depend on the aspect ratio $\mathcal{R}$ as $L_{\rm j} \propto \mathcal{R}^{2\alpha-8}$ and $t_{\rm age} \propto \mathcal{R}^{4-\alpha}$, and, therefore,

satisfy $L_{\rm j} \propto t_{\rm age}^{-2}$. Since α does not exceed 4 in any of the four sources, a lower aspect ratio corresponds to a higher power with a lower age.

It should be noted that the uncertainty in the absolute values of $\rho_{\rm a}$ and $P_{\rm a}$ is not crucial, since $P_{\rm a}$ is used only to judge whether the over-pressure condition is satisfied or not, and the dependence of $L_{\rm j}$ and $t_{\rm age}$ on $\rho_{\rm a}$ is rather weak, $L_{\rm j} \propto \rho_{\rm a}$ and $t_{\rm age} \propto \rho_{\rm a}^0$. The line outside the shaded region must be discarded, since the over-pressure condition is violated. The Eddington luminosity, $L_{\rm Edd}$, of each source is also shown in these figures for comparison. In Table 3.2, we summarize the allowed values of $L_{\rm j}$ and $t_{\rm age}$ and other relevant physical parameters of cocoon obtained for the parameter set listed in Table 3.1.

Cygnus A is one of the vastly studied nearby FR II radio galaxies. Tadhunter et al. (2003) estimated the SMBH mass of Cygnus A as $2.5 \times 10^9 M_\odot$, based on the gas kinematics in the narrow-line region. Its linear size is measured as $r_{\rm h} = 70$ kpc for the western jet and $r_{\rm h} = 60$ kpc for the eastern jet. From the employed values of $r_{\rm h}$ and $A_{\rm h}$, the power and age are obtained as $L_{\rm j} = (0.35 - 1.1) \times 10^{46}$ ergs s^{-1} and $t_{\rm age} = 30 - 53$ Myr for the western jet and $L_{\rm j} = (0.4 - 2.6) \times 10^{46}$ ergs s^{-1} and $t_{\rm age} = 19 - 47$ Myr for the eastern jet. No significant difference is seen between the two jets, and we interpret that the actual age lies in these ranges. Note that $L_{\rm j}$ is decreased and $t_{\rm age}$ is increased from those in KK05 by the improvement of $V_{\rm c}$ and the inclusion of PdV work. In fact, while $L_{\rm j} = 1.3 \times 10^{48}$ ergs s^{-1} and $t_{\rm age} = 2.6$ Myr were obtained in KK05, we find $L_{\rm j} = 2.6 \times 10^{46}$ ergs s^{-1} and $t_{\rm age} = 19$ Myr in the present study when the identical values of $r_{\rm h} = 60$ kpc, $A_{\rm h} = 150$ kpc^2, and $\mathcal{R} = 0.5$ are employed.

3C 223 has radio lobes that extend up to $r_{\rm h} = 340$ kpc in both sides. Its SMBH mass is estimated as $1.4 \times 10^8 M_\odot$ by Woo & Urry (2002), based on the observed stellar velocity dispersions. As can be seen in Fig. 3.6, 3C 223 has asymmetry in $A_{\rm h}$. While a well developed cocoon head is seen at the northern hot spot ($A_{\rm h} = 4300$ kpc^2), the cocoon head at the southern hot spot is quite compact ($A_{\rm h} = 1800$ kpc^2). Reflecting this asymmetry, the obtained power and age show quite large difference: $L_{\rm j} = (0.15 - 2.9) \times 10^{46}$ ergs s^{-1} and $t_{\rm age} = 140 - 610$ Myr for the northern jet, and $L_{\rm j} = (0.71 - 2.0) \times 10^{45}$ ergs s^{-1} and $t_{\rm age} = 330 - 560$ Myr for the southern jet.

3C 284 shows asymmetry both in $r_{\rm h}$ and $A_{\rm h}$. While $r_{\rm h}$ and $A_{\rm h}$ in the western lobe are estimated as 380 kpc and 6200 kpc^2, respectively, the corresponding values for the eastern lobe are 260 kpc and 4600 kpc^2. The obtained power and age are $L_{\rm j} = (0.1 - 3.6) \times 10^{46}$ ergs s^{-1} and $t_{\rm age} = 100 - 630$ Myr for the western jet and $L_{\rm j} = (0.03 - 1.8) \times 10^{47}$ ergs s^{-1} and $t_{\rm age} = 32 - 260$ Myr for the eastern jet. Since there is no estimate of the SMBH mass of 3C 284 in the literature, we derive the mass from the B-band magnitude of the bulge estimated in Shi et al. (2005). By using the equation in Marchesini et al. (2004) which gives the correlation of the B-band magnitude with the BH mass, we obtain $M_{\rm BH} = 8.2 \times 10^8 M_\odot$.

In the case of 3C 219, we only analyze the jet in the western side, since the eastern lobe shows severe deformation (see Fig. 3.6). We could not determine $A_{\rm h}$ in the eastern side from its morphology. In the same way as in 3C 223, the central SMBH mass for 3C 219 is estimated

by Marchesini et al. (2004) as $6.3 \times 10^8\ M_\odot$. $r_{\rm h}$ and $A_{\rm h}$ of the western lobe are measured as 210 kpc and 5000 kpc^2. From these values, the jet kinetic power and age are obtained as $L_{\rm j} = (0.26 - 4.3) \times 10^{47}$ ergs s^{-1} and $t_{\rm age} = 37 - 150$ Myr, respectively.

Large asymmetry between the pair of lobes is observed especially in 3C 223 and 3C 284, and 3C 219. Since it seems natural to suppose that the jet properties are intrinsically symmetric and the power and age is identical on both sides, we expect that the asymmetry in the pair of lobes is due to the asymmetry and/or inhomogeneity of ICM density profile. Although this is an interesting subject, the detail is beyond the scope of the present study. Here we assume that the actual values of $L_{\rm j}$ and $t_{\rm age}$ are lying in the ranges obtained from both lobes.

In Table 3.2 (column 4), the total kinetic powers of jet normalized by the corresponding Eddington luminosity, $2L_{\rm j}/L_{\rm Edd}$, are displayed. It can be seen that $2L_{\rm j}/L_{\rm Edd}$ takes quite high values ranging from ~ 0.02 to ~ 10. In exploring the physical relations between the accretion power and the outflow, the total kinetic power of jet normalized by Eddington luminosity, $2L_{\rm j}/L_{\rm Edd}$, is one of the most fundamental parameters. We will return to this issue in §3.3.1.

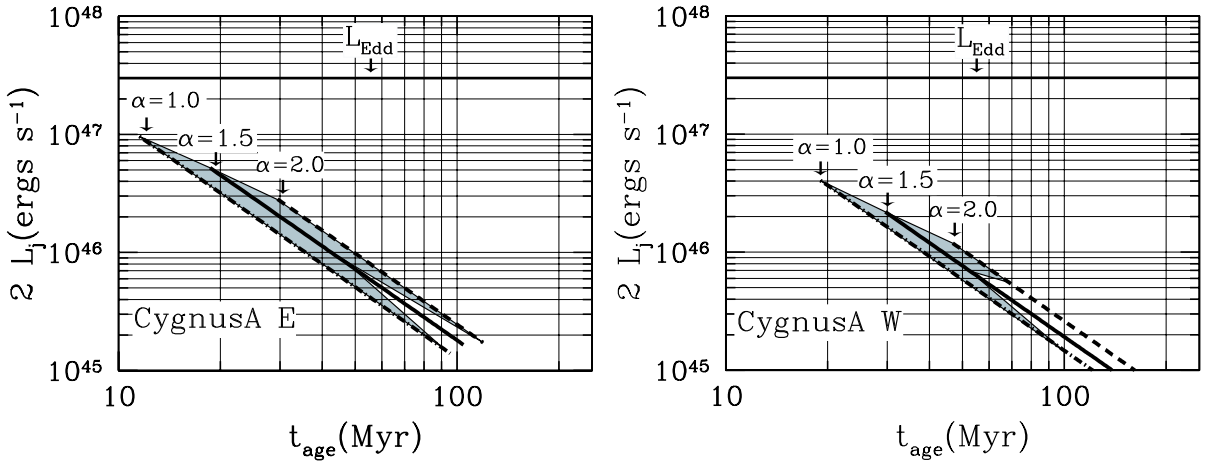

Figure 3.2: The obtained ranges of power and age of Cygnus A. The three oblique lines, which lie closely to each other are the solutions for the power-law index of the ICM density (α) shown by arrow; The solid line represents the solution for the estimated power-law index (see Table 3.1). The dashed and dot-dashed lines represent the solutions for the power-law index increased by 0.5 and decreased by 0.5, respectively. The shaded regions show allowed ranges where the overpressure condition ($P_{\rm c} > P_{\rm a}$) is satisfied. Also the Eddington luminosities are displayed by the horizontal lines for comparison.

Table 3.2: The obtained properties of the jet and the cocoon together with minimum energy of the radio lobe.

Source	$L_{\rm j}$ (10^{46} ergs s^{-1})	$t_{\rm age}$ (Myr)	$M_{\rm BH}$ ($M_\odot$)	$2L_{\rm j}/L_{\rm Edd}$	$E_{\rm c}$ (10^{60} ergs)	$E_{\rm min}$ (10^{60} ergs)	$\eta_{\rm c}$	
(1)	(2)	(3)	(4)	(5)	(6)	(7)	(8)	Ref.
Cygnus A E	0.4 - 2.6	19 - 47	2.5×10^9	0.025 - 0.16	6.2 - 16	1.4	4.4 - 11	2
Cygnus A W	0.35 - 1.1	30 - 53	2.5×10^9	0.021 - 0.068	6.1 - 11	1.4	4.3 - 7.8	2
3C 223 N	0.15 - 2.9	140 - 610	1.4×10^8	0.16 - 3.2	30 - 130	0.88	34 - 150	1
3C 223 S	0.071 - 0.2	330 - 560	1.4×10^8	0.078 - 0.22	12 - 22	0.88	14 - 25	1
3C 284 E	0.3 - 18	32 - 260	8.2×10^8	0.053 - 3.4	26 - 210	1.8	14 - 120	3,4
3C 284 W	0.1 - 3.6	100 - 630	8.2×10^8	0.018 - 0.67	21 - 130	3.0	7 - 43	3,4
3C 219 W	2.6 - 43	37 - 150	6.3×10^8	0.65 - 10	130 - 500	1.6	79 - 310	3

Note. — Column (1) shows the names of radio sources, and the following alphabet distinguishes the pair of jets (see Fig. 3.6). Columns (2) and (3) display, respectively, the total kinetic powers and ages of the radio jets. In column (4) and (5), the black hole mass and the kinetic powers normalized by the corresponding Eddington luminosity are displayed, respectively. References for the central SMBH mass are given in parentheses. In Columns (6) and (7), the total energies deposited in the cocoon and the minimum energies required for the synchrotron emission are displayed, respectively. Column (8) gives the ratios between $E_{\rm c}$ and $E_{\rm min}$.

References. — (1) Woo & Urry (2002); (2) Tadhunter et al. (2003); (3) Marchesini et al. (2004); (4) Shi et al. (2005).

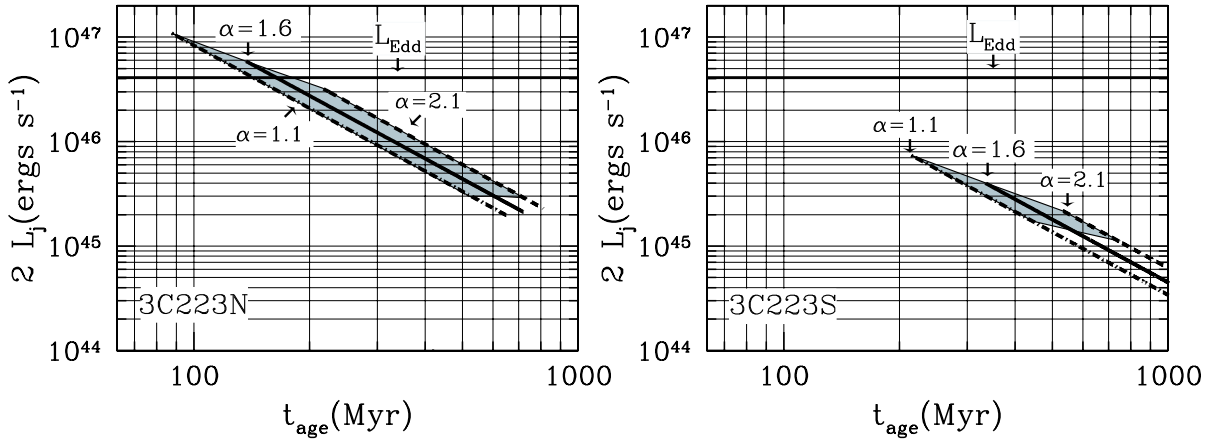

Figure 3.3: Same as Fig. 3.2, but for 3C 223.

3.2.2 Total internal energy vs. minimum energy

It is intriguing to compare the internal energy, $E_{\rm c}$, deposited in the cocoon with the widely discussed energy, $E_{\rm min}$, obtained from the minimum energy condition (e.g., Miley 1980). $E_{\rm c}$ is linearly proportional to the total energy injected in the cocoon ($2L_{\rm j}t_{\rm age}$) and is approximately given as $E_{\rm c} \simeq L_{\rm j}t_{\rm age}$. The dependence on the aspect ratio is given by $E_{\rm c} \propto L_{\rm j}t_{\rm age} \propto L_{\rm j}^{1/2} \propto \mathcal{R}^{\alpha-4}$ (§3.2.1). Hence, a smaller aspect ratio (or, equivalently, a larger power) corresponds to a larger internal energy. $E_{\rm min}$ is the minimum value of the total energy (the sum of the energies in radiating non-thermal electrons and magnetic fields) required for a given synchrotron luminosity and is evaluated as

$$E_{\rm min} = \frac{7}{24\pi} V_{\rm R}^{\frac{3}{7}} \left[6\pi f(\alpha_{\rm R}) (\nu_{\rm min}^{0.5-\alpha_{\rm R}} - \nu_{\rm max}^{0.5-\alpha_{\rm R}}) \nu^{\alpha_{\rm R}} L_\nu \right]^{\frac{4}{7}}, \tag{3.2}$$

where $V_{\rm R}$ is the volume of the emitting region, $\alpha_{\rm R}$ is the spectral index of the synchrotron emission, $f(\alpha_{\rm R})$ is a function of $\alpha_{\rm R}$, and L_ν is the synchrotron luminosity measured at frequency ν, and $\nu_{\rm min}$ and $\nu_{\rm max}$ are the lower and higher cut-offs in the synchrotron emission, respectively (see Appendix A for detail).

The values of the spectral index $\alpha_{\rm R}$ at the low frequency band (178–750 MHz) and the flux density, F_ν, at 178MHz are taken from Table 1 in Hardcastle et al. (1998). From the employed values of F_ν, the synchrotron luminosities are calculated as $L_\nu = 4\pi d_{\rm L}^2 F_\nu$, where $d_{\rm L}$ is the luminosity distance. Although L_ν is the sum of the luminosity from lobes, jets and hot spots, no significant overestimate of L_ν is expected because the radio emission is dominated by the lobe-component for most of FRII sources (Bridle et al. 1994; Hardcastle et al. 1998). The employed values of $\alpha_{\rm R}$, L_ν and other relevant quantities are summarized in Table 3.3. Here we

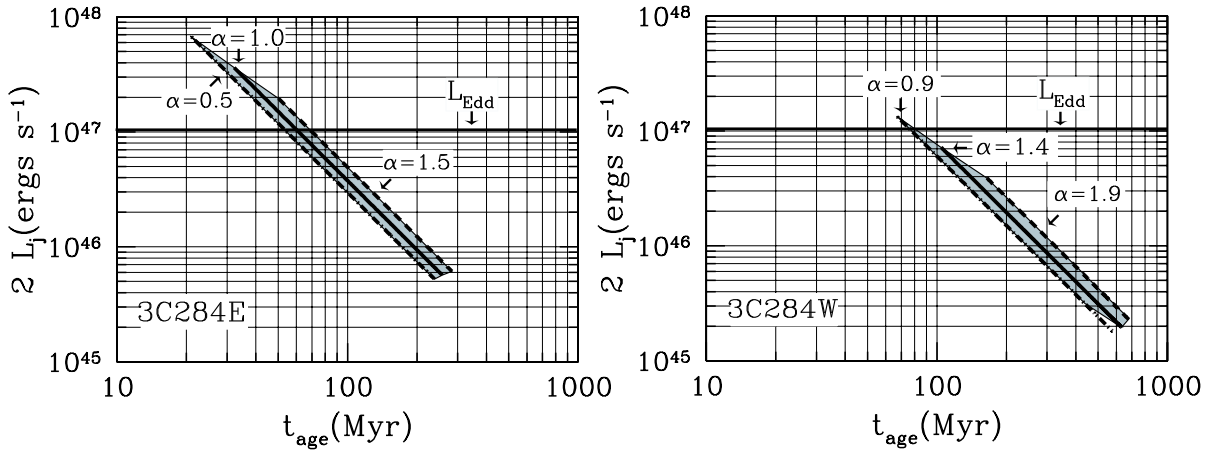

Figure 3.4: Same as Fig. 3.2, but for 3C 284.

neglect the second term in Eq. (3.2) in deriving $E_{\rm min}$, since $\alpha_{\rm R} > 0.5$ is satisfied in all sources. The lower cut-off frequency $\nu_{\rm min}$ is taken as 10^4 Hz. We will comment on this value in the next paragraph. As noted in §3.1.3, although GHz radio images do not show a cocoon-shape clearly and only a pair of lobes can be seen, it is known that radio images at lower frequencies reflect the cocoon shape more closely (e.g., Readhead et al. 1996; Carilli et al. 1991) because of the absence of efficient radiative coolings. Since we utilize a relatively low frequency (178MHz) band, the volume of the emission region can be approximated as $V_{\rm R} \sim V_{\rm c}$. Here we employ the median value of $\mathcal{R}$, i.e., $\mathcal{R} = 0.75$, in evaluating $V_{\rm R}$. We define the ratio of $E_{\rm c}$ to $E_{\rm min}$ as $\eta_{\rm c}$:

$$\eta_{\rm c} \equiv \frac{E_{\rm c}}{E_{\rm min}}. \tag{3.3}$$

The obtained values of $E_{\rm min}$, $E_{\rm c}$, and $\eta_{\rm c}$ are summarized in Table 3.2. We find that $E_{\rm c}$ is larger than $E_{\rm min}$ and $\eta_{\rm c}$ is in the range of $4 < \eta_{\rm c} < 310$. This implies that there is a substantial deviation from the minimum energy condition. We will discuss this topic more in detail in §3.3.2.

Lastly, we comment on the reliability of $\eta_{\rm c}$. The lower cut-off frequency, $\nu_{\rm min}$, is one of the ingredients, which introduce uncertainties in $\eta_{\rm c}$ because it is difficult to determine by radio observations. The value employed above is obtained from the following relation $\nu_{\rm min} \approx 10^4\ (B/10^{-5}\ {\rm G})(\gamma_{\rm e,min}/10)^2$ Hz, where $\gamma_{\rm e,min}$ is the minimum Lorentz factor of non-thermal electrons. Note that the the resultant $E_{\rm min}$ does not change significantly by the uncertainty in $\nu_{\rm min}$ because of its weak dependence. For example, when a typical value of $\alpha_{\rm R} = 0.8$ is employed $E_{\rm min} \propto (\nu_{\rm min}/10^4\ {\rm Hz})^{6/35}$. It should be also mentioned that the difference between the actual emission volume and the employed one, which we do not expect to vary by orders,

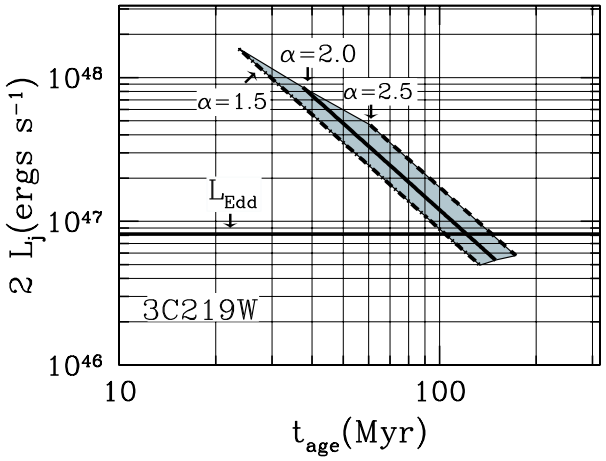

Figure 3.5: Same as Fig. 3.2, but for 3C 219.

does not affect our result, since the dependence of $E_{\rm min}$ on the emission volume $V_{\rm R}$ is weak, $E_{\rm min} \propto V_{\rm R}^{3/7}$. Hence the precise determination of the latter is not necessary.

3.2.3 On the estimation of $L_{\rm j}$ and $E_{\rm c}$

Upper limits and lower limits

It is important to consider the validity of the over-pressure condition (i.e. $P_{\rm c} > P_{\rm a}$), since the lower limits of $L_{\rm j}$ and $E_{\rm c}$ are determined by this condition in most cases (see Figs. 3.2-3.5). In our model, a larger $P_{\rm c}$ corresponds to a smaller $\mathcal{R}$. Though we explore a wide range of $\mathcal{R}$ (0.5 to ~ 1), it is intuitively more likely that $\mathcal{R}$ is smaller than unity, that is, the cocoon is prolate rather than spherical. Hence, the results of our analysis suggest that the sources examined in the present study are likely to be over-pressured indeed. Incidentally, the prolate shape of cocoon is endorsed by the fact that independent age estimations of Cygnus A (Carilli et al. 1991) and 3C 284 (Alexander & Leahy 1987) based on the spectral ageing method are more consistent with the results for the aspect ratio of 0.5 than for 1.0. (Unfortunately, the age estimations are not available for 3C 223 and 3C 219 in the literature).

In all cases, the maximum values of $L_{\rm j}$ and $E_{\rm c}$ correspond to the minimum value of $\mathcal{R}$ ($L_{\rm j} \propto \mathcal{R}^{2\alpha-8}$). Though $\mathcal{R} = 0.5$ is chosen as the lower limit in the present study (§3.1.3), the possibility of even smaller aspect ratios cannot be ruled out, since the radius of cocoon body $r_{\rm c}$ cannot be constrained very well from the radio images. It is emphasized again that smaller values of $\mathcal{R}$ predict larger $L_{\rm j}$ and $E_{\rm c}$.

Table 3.3: The observed radio information.

Source	z	d_L (Mpc)	F_ν (Jy)	α_R	L_ν (ergs $s^{-1}Hz^{-1}$)	L_R (ergs s^{-1})
(1)	(2)	(3)	(4)	(5)	(6)	(7)
Cygnus A	0.0565	249	9660	0.74	6.2×10^{35}	1.1×10^{44}
3C 223	0.1368	635	16.0	0.74	7.7×10^{33}	1.4×10^{42}
3C 284	0.2394	1182	12.3	0.95	1.0×10^{34}	1.8×10^{42}
3C 219	0.1744	829	44.9	0.81	3.7×10^{34}	6.5×10^{42}

Note. —Column (1) shows the names of radio sources. Columns (2) and (3) display, respectively, the redshift and the luminosity distance calculated for the cosmology with $H_0 = 71$km s^{-1}, $\Omega_M = 0.3$, and $\Omega_\Lambda = 0.7$. Columns (4) and (5) give the values of flux densities and spectral indexes at 178MHz, which are taken from the table (Table 1) of Hardcastle et al. (1998). In Column(6) and (7), the calculated luminosity densities at 178MHz and the radio luminosities, which we calculated from the relation $L_R = \nu L_\nu$ are presented, respectively.

Improvements from KK05

As mentioned in §2.1, we have improved the energy equation given in KK05 as follows: (i) a more accurate definition of V_c is employed, and (ii) the PdV work, which is done by the cocoon against the contact discontinuity between the cocoon and the shocked ambient medium, is taken into account. These corrections are necessary for an accurate estimate of the jet kinetic power, since the resultant change in the derived L_j turns out to be rather large. In fact, the estimated power is reduced by a factor of ~ 50 from the value in KK05 for Cygnus A after taking account of the corrections (see §3.2.1). As for modification (i), the main flaw in KK05 is the fact that they did not take into account the sideways expansion in the growth of V_c. In fact, they employed the equation, $dV_c/dt = 2\pi r_c^2 v_h$, whereas a more accurate expression is $dV_c/dt = (4/3)[\pi r_c^2 v_h + 2\pi r_c r_h v_c]$, which is adopted in the present study. As for modification (ii), it was assumed that all injected energy is converted to internal energy (namely, $E_c = 2L_j t_{age}$) in KK05. it is obvious, however, that a part of the injected energy is consumed for expansions and the PdV work should be included, particularly for quantitative estimations. As found in §2.2.3, these corrections are reflected only in the numerical factor $\mathcal{C}_{vh}$ in Eq. (2.6). The value of $\mathcal{C}_{vh}$ is reduced by a factor of ~ 3.5 owing to (i) and another factor of ~ 2 due to (ii) and, hence, by a factor of ~ 7 as a whole.

For a given geometry of cocoon (r_h, A_h, and $\mathcal{R}$) and ambient density profile (ρ_a and α), the derived power and age scale with the numerical factor as $L_j \propto \mathcal{C}_{vh}^2$ and $t_{age} \propto \mathcal{C}_{vh}^{-1}$, respectively. As a result, KK05 overestimated L_j by a factor of ~ 50. On the other hand, t_{age} was underestimated by a factor of ~ 0.14, which led to the overestimation of E_c by a factor of ~ 14, since the latter is obtained as $E_c = 2L_j t_{age}$ in KK05. It is also worthy to note that in the present study the following relation holds: $E_c \simeq L_j t_{age}$. The difference of the factor ~ 2

arises from the fact that about a half of the injected energy is used for the PdV work.

Kinetic energy in the cocoon

We have so far neglected the kinetic energy of bulk flows in the cocoon, assuming that the internal energy is dominated over the kinetic energy. This may be justified by the fact that the cocoon is filled with shocked jet matter, which are expected to flow subsonically. It is, however, important to estimate the possible changes in $L_{\rm j}$ and $E_{\rm c}$ that the inclusion of the kinetic energy in Eq. (2.3) (energy equation) may make, since our results are rather sensitive to the changes in the energy equation as mentioned above. Although the lack of our knowledge on the mass deposited in the cocoon makes it difficult to estimate the kinetic energy quantitatively, the changes in $L_{\rm j}$ and $E_{\rm c}$ are not significant for the conclusion of the present study even in the case, where the kinetic energy is comparable to the internal energy, as shown shortly.

As was mentioned previously, the modification in energy equation is reflected in the value of the numerical factor $\mathcal{C}_{\rm vh}$ of Eq. (2.6). Note that $\mathcal{C}_{\rm vh}$ depends linearly on the ratio of the total internal energy to the total injected energy, $\epsilon \equiv E_{\rm c}/(2L_{\rm j}t_{\rm age})$, which is $\sim 1/2$ in the present study, since roughly a half of the injected energy is consumed for the PdV work. The inclusion of the kinetic energy modifies ϵ as $\epsilon \sim 1/(2+f)$, where f is defined as the ratio of the kinetic energy to the internal energy and $\mathcal{C}_{\rm vh}$ is reduced from the value obtained in the present study by a factor of $\sim 2/(2+f)$. It is hence found that even if the kinetic energy is as large as the internal energy, namely $f \sim 1$, $L_{\rm j}(\propto \mathcal{C}_{\rm vh}^2)$ and $E_{\rm c}(\propto \mathcal{C}_{\rm vh})$ are reduced only by factors of $\sim 4/9$ and $\sim 2/3$, respectively. The inclusion of the kinetic energy, therefore, does not change the conclusion of this study.

3.3 Implications on the Energetics

In this chapter, we have investigated the total kinetic power and age of powerful FR II jets. We have selected four FR II radio galaxies (Cygnus A, 3C 223, 3C 284, and 3C 219), for which the surrounding ICM densities and pressures are known in the literature. Below we summarize our main results.

(I) *Large fractions of the Eddington power in the range of* $\gtrsim 0.02-0.7$ *are carried away as a kinetic power of jet in the FR II sources.*

(II) *The energy deposited in the cocoon,* $E_{\rm c}$*, exceeds the minimum energy,* $E_{\rm min}$*, by a factor of* $4-310$.

In the following, we will discuss some implications of our results. In §3.3.1, we address some issues concerning the ratio of $L_{\rm j}$ to $L_{\rm Edd}$ by referring to the studies of X-ray binaries. In §3.3.2, the plasma content in the cocoons is constrained from the obtained $\eta_{\rm c}$.

3.3.1 $L_{\rm j}/L_{\rm Edd}$

If we postulate that the relativistic jet emanating from the AGN is powered by a part of released gravitational energy ($L_{\rm acc}$) of the accreting matter (e.g., Marscher et al. 2002), $2L_{\rm j}/L_{\rm Edd}$ gives the minimum mass accretion rate normalized by the Eddington mass accretion rate. Our results then indicate that the mass accretion rates are super-Eddington for some FR II radio galaxies (3C 219 and 3C 284), since $2L_{\rm j}/L_{\rm Edd} \simeq 1$. Then the theory of accretion disk predicts that the accretion disk of these objects are optically-thick, called *slim-disk* (e.g., Abramowicz et al. 1988). From three distinctive X-ray properties (large photon index $\Gamma \gtrsim 2$, rapid variability and soft X-ray excess), narrow line Seyfert 1 galaxies (NLS1s) are considered to be super-Eddington objects and, therefore, are inferred to have slim-disk (e.g., Pounds et al. 1995; Boller et al. 1996; Mineshige et al. 2000; Collin & Kawaguchi 2004; Shemmer et al. 2006). If 3C 284 and 3C 219 are indeed super-Eddington objects, it is expected that they show the above mentioned X-ray features like NLS1s. However, 3C 219 has a relatively hard X-ray spectrum with $\Gamma = 1.58 < 2$ (Shi et al. 2005). Thus, the physical state of the accretion disk in 3C 219 could be different from those in NLS1s. (We have no X-ray data for 3C 284.)

In order to explore the nature of the accretion disk in 3C 219, we compare the characteristics of AGNs with those of X-ray binaries (XRB), since both of them have common physical processes such as disk accretions, relativistic jets, and quenching of these jets (e.g., Heinz & Sunyaev 2003; Ho 2005; McHardy et al. 2006). Thanks to their much shorter dynamical timescales, XRBs in various states have been observed in great detail and are found to occupy particular X-ray spectral states (Fender et al. 2004; Remillard & McClintock 2006 for a review) as follows;

(i) $L_{\rm acc}/L_{\rm Edd} \lesssim 0.01$ (low/hard state: LS),

(ii) $0.01 \lesssim L_{\rm acc}/L_{\rm Edd} \lesssim 0.3$ (high/soft state: HS),

(iii) $L_{\rm acc}/L_{\rm Edd} \gtrsim 0.3$ (very high state: VHS).

State (i) is usually accompanied by a jet. For $L_{\rm acc}/L_{\rm Edd} > 0.01$, the radio emission is quenched in state (ii), while in state (iii), soft VHS, which has an X-ray spectrum dominated by a steep power-law component (photon index $\Gamma > 2$), is radio quiet, and hard VHS and/or transitions from hard VHS to soft VHS are accompanied by a relativistic ejection events.

If the analogy between XRBs and AGNs holds, NLS1s may be soft VHS since many NLS1s have a steep power-law component and high Eddington ratio > 0.3 (e.g., Collin & Kawaguchi 2004), which is the upper limit for the stability of the standard disk (Shakura & Sunyaev 1973). On the other hand, 3C 219 (FR II) may correspond to hard VHS and/ or the transition state because it has a hard X-ray spectra and high Eddington luminosities. In order to judge whether AGNs are scaled-up XRBs, it is essential to confirm that radio loud AGNs have states analogous to the spectral states (especially VHS) in XRBs [1].

[1] It has been well established that low-luminosity AGNs are the high-mass counterpart of XRBs in LSs (Ho 2005)

The co-evolution of a central black hole (BH) and its host galaxy together with AGN feedbacks have been intensively studied in various ways (e.g., Silk & Rees 1998; Di Matteo et al. 2003; Granato et al. 2004). The intensive surveys of QSOs show that the number density of QSOs is peaked at $z \approx 2$ Fan et al. (2001). The existence at $z \gtrsim 2$ of QSOs with a central BH having a smaller mass than predicted from the bulge BH-mass relation is naturally expected in the build-up of SMBHs toward $z \approx 2$. For the exploration of the co-evolution processes, dusty spheroidal galaxies (e.g., galaxies emitting sub-millimeter radiations and ultra-luminous infrared galaxies) are the ones to be scrutinized, since the dusty-gas in them is one of the key quantities for the co-evolution. Kawakatu et al. (2003) pointed out the possibility of radio loud AGNs at high-z being QSOs in the early evolution phase (we call them proto-QSOs) that contain a growing BH. It is, however, difficult to explore the nature of proto-QSOs at high-z by observations in optical and X-ray bands owing to severe dust-absorptions. In contrast, the estimate of $L_{\rm j}$ and $t_{\rm age}$ presented in this work is applicable even to high-z sources (e.g., Schmidt et al. 2006) without the dust extinction. Therefore, the estimate of $L_{\rm j}/L_{\rm Edd}$ based on the cocoon dynamics is a potential new powerful tool to discover proto-QSOs among high-z radio loud AGNs.

3.3.2 The plasma content

Lastly, we discuss the plasma content in the cocoon using the obtained energy ratio $\eta_{\rm c} \equiv E_{\rm c}/E_{\rm min}$. Here, we express $E_{\rm c}$ by components as $E_{\rm c} = (U_{\rm e}^{\rm NT} + U_{\rm e}^{\rm T} + U_{\rm p}^{\rm T} + U_{\rm p}^{\rm NT})V_{\rm c}$, where $U_{\rm e}^{\rm T}$, $U_{\rm e}^{\rm NT}$, $U_{\rm p}^{\rm T}$ and $U_{\rm p}^{\rm NT}$, are the energy densities of the non-thermal leptons (electrons and positrons), the thermal leptons, the non-thermal protons, and thermal protons, respectively. In the following, we try to constrain the plasma content by considering the following four extreme cases;

(i) non-thermal leptons ($U_{\rm e}^{\rm NT}$) dominated,
(ii) thermal leptons ($U_{\rm e}^{\rm T}$) dominated,
(iii) non-thermal protons ($U_{\rm p}^{\rm NT}$) dominated, and
(iv) thermal protons ($U_{\rm p}^{\rm T}$) dominated.

The cocoon is filled with the shocked plasma produced at the tip of the relativistic jet. According to the recent studies of diffusive shock acceleration (DSA) in the relativistic regime, the non-thermal particle distribution is expected to be $n(\gamma)d\gamma \propto \gamma^{-{\rm s}}d\gamma$, $s \approx 2.2$ (Bednarz & Ostrowski 1998; Kirk & Duffy 1999; Achterberg et al. 2001), on which we focus here.

First, we consider case (i). It is useful to express $U_e^{\rm NT}/U_{\rm min}$ in terms of $U_e^{\rm NT}/U_{\rm B}$, where $U_{\rm B}$ is the energy density of magnetic field, since $U_e^{\rm NT}/U_{\rm B}$ is intensively investigated by a lot of authors (e.g., Isobe et al. 2002; Kataoka et al. 2003; Croston et al. 2004; Kataoka & Stawarz; Croston et al. 2005). For given $\nu_{\rm min}$, $\nu_{\rm max}$, and $\alpha_{\rm R}$, the synchrotron luminosity is given by $L_\nu \propto U_{\rm e}^{NT}U_{\rm B}^{4/3}V_{\rm c}$. Hence with L_ν and $V_{\rm c}$ given, $U_{\rm e}$ and $U_{\rm B}$ are not independent of each other. As a function of the strength of magnetic fields, B, the ratios of the energies

of non-thermal particles and magnetic fields to the minimum energy are given respectively as $U_{\rm e}^{\rm NT}/U_{\rm min} = (4/7)(B/B_{\rm min})^{-3/2}$ and $U_{\rm B}/U_{\rm min} = (3/7)(B/B_{\rm min})^2$, where $B_{\rm min}$ denotes the magnetic field strength when minimum energy condition is satisfied. The minimum energy condition ($d(U_{\rm e}^{\rm NT} + U_{\rm B})/dB = 0$) corresponds to the relation of $U_{\rm e}^{\rm NT} = (4/3)U_{\rm B}$. From the above equations, we can derive an equivalent equation as

$$\eta_{\rm c} = \frac{U_{\rm e}^{\rm NT}}{U_{\rm min}} \simeq 0.5 \left(\frac{U_e^{\rm NT}}{U_{\rm B}}\right)^{3/7}, \tag{3.4}$$

where the numerical factor comes from $0.5 \simeq (4/7) \times (3/4)^{3/7}$. We have also $U_{\rm B}/U_{\rm min} \simeq 0.5(U_{\rm e}^{\rm NT}/U_{\rm B})^{-4/7}$. Since recent studies show $1 \lesssim U_{\rm e}^{\rm NT}/U_{\rm B} \lesssim 10$ on average, the value of $\eta_{\rm c}$ is expected to be ~ 1 at most. Thus, case (i) is unlikely and non-thermal leptons are excluded as the main carrier of the missing kinetic power unless extremely large $U_{\rm e}^{\rm NT}/U_{\rm B}$ takes place in the cocoon.

Next we consider case (ii). The relation between the average Lorentz factor of non-thermal leptons and the temperature of thermal leptons is given by

$$\frac{k_{\rm B}T_{\rm e}}{m_{\rm e}c^2} \approx \gamma_{\rm e,min} = \frac{1}{6}\langle\gamma_{\rm e}\rangle, \tag{3.5}$$

where $\gamma_{\rm e,min}$, $\langle\gamma_{\rm e}\rangle$, $k_{\rm B}$, and $T_{\rm e}$, are the minimum Lorentz factor of non-thermal leptons, the average Lorentz factor of non-thermal leptons, the Boltzmann constant, and the temperature of thermal electrons, respectively. The first approximate relation in Eq. (3.5) is based on the standard DSA model, in which it seems natural to suppose that non-thermal electrons are originated from the high energy tail of the thermal Maxwellian distribution. From above relations, we obtain

$$\frac{n_{\rm e}^{\rm T}}{n_{\rm e}^{\rm NT}} \approx 12\eta_{\rm c} \left(\frac{U_{\rm B}}{U_{\rm e}^{\rm NT}}\right)^{3/7}, \tag{3.6}$$

where $n_{\rm e}^{\rm T}$ and $n_{\rm e}^{\rm NT}$ are the number densities of thermal leptons and non-thermal leptons, respectively, since $n_{\rm e}^{\rm T}/n_{\rm e}^{\rm NT}$ is proportional to $kT/\langle\gamma_{\rm e}\rangle$. For the proton population under the DSA process, we similarly estimate $k_{\rm B}T_{\rm p}/(m_{\rm p}c^2) \approx \gamma_{\rm p,min} = \langle\gamma_{\rm p}\rangle$/6, where $\gamma_{\rm p,min}$, $\langle\gamma_{\rm p}\rangle$, and $T_{\rm p}$ are the minimum Lorentz factor of non-thermal protons, the average Lorentz factor of non-thermal protons, and the temperature of thermal protons, respectively. From the obtained value of $\eta_{\rm c}$ and the expected value of $U_{\rm B}/U_{\rm e}^{\rm NT}$ (< 1), we see that the number density of thermal leptons is larger than that of non-thermal leptons. Similarly, for cases (iii) and (iv) we obtain

$$\frac{n_{\rm p}^{\rm NT}}{n_{\rm e}^{\rm NT}} \approx 1.0 \times 10^{-3} \left(\frac{U_{\rm B}}{U_{\rm e}^{\rm NT}}\right)^{3/7} \eta_{\rm c}, \qquad \frac{n_{\rm p}^{\rm T}}{n_{\rm e}^{\rm NT}} \approx 6.0 \times 10^{-3} \left(\frac{U_{\rm B}}{U_{\rm e}^{\rm NT}}\right)^{3/7} \eta_{\rm c}, \tag{3.7}$$

where $n_{\rm p}^{\rm T}$ and $n_{\rm p}^{\rm NT}$ are the number densities of thermal protons and non-thermal protons, respectively, Here we assume the relation between the two temperatures, $k_{\rm B}T_{\rm e} \approx (m_{\rm e}/m_{\rm p})k_{\rm B}T_{\rm p}$, since the coupling between electrons and protons is expected to be inefficient Kino et al. (2007). From the obtained value of $\eta_{\rm c}$, $n_{\rm p}^{\rm NT}/n_{\rm e}^{\rm NT}$ and $n_{\rm p}^{\rm T}/n_{\rm e}^{\rm NT}$ tend to be less than unity.

To sum up, non-thermal electrons are not likely to be energetically dominant, which implies that the energy is mainly carried by thermal leptons and/or protons. We stress that the proton number density tends to be less than that of non-thermal leptons ($n_{\rm p}/n_{\rm e} \sim 10^{-3} - 0.5$). Thus, within the framework of present study, the possibility that the plasma consists of normal composition (pure proton-electron) is ruled out. This is consistent with the previous works (Reynolds & Fabian 1996; Hirotani et al. 1999; Sikora & Madejski 2000; Kino & Takahara 2004). Tighter constraints on the plasma composition in jet are expected to be obtained by the detailed studies on the minimum Lorentz factor and the temperature of electrons and protons. We bear this in mind as an interesting subject for future investigations.

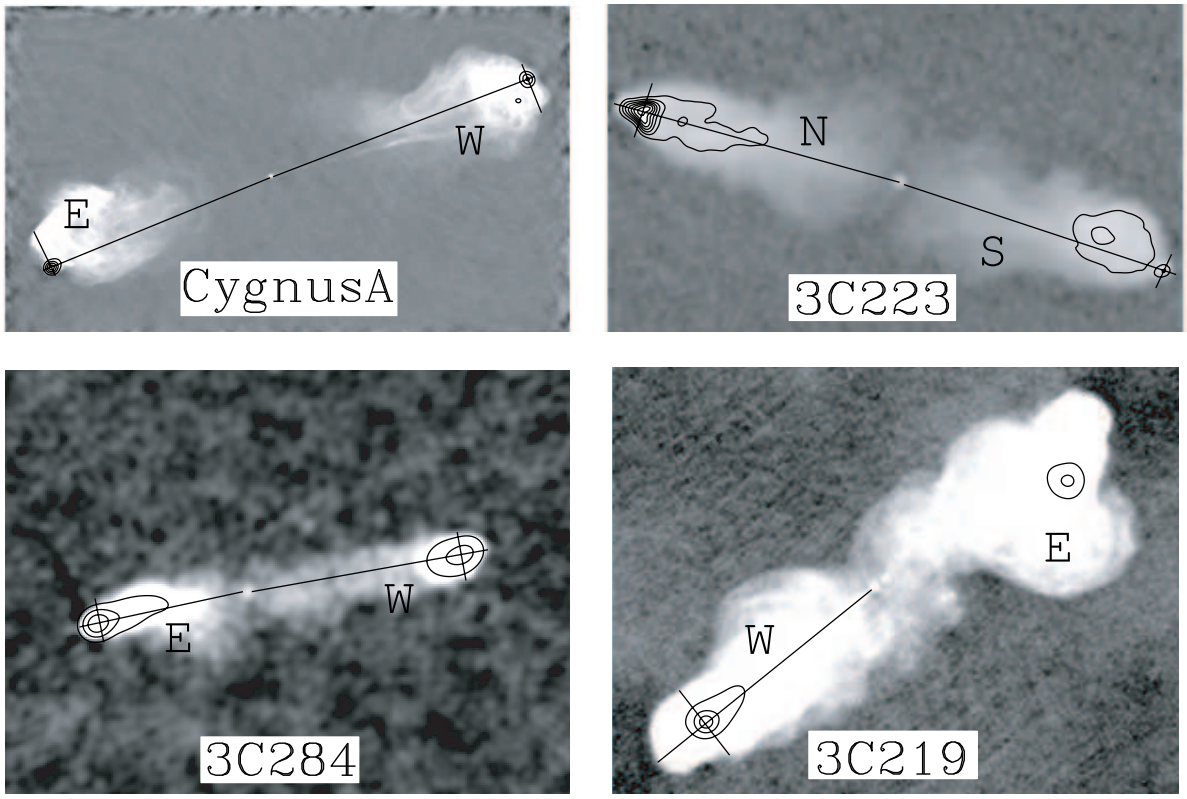

Figure 3.6: Logarithmic-scaled 5-GHz VLA map of Cygnus A (upper-left) and 1.5GHz VLA maps of 3C 223 (upper-right), 3C 284 (lower-left), and 3C 219 (lower-right) with linearly spaced contours are displayed. The straight lines overlaid in each map denote the lines we have used to measure $r_{\rm h}$ and $A_{\rm h}$.

Chapter 4

MeV γ RAY EMISSION FROM COCOON

Non-thermal emissions from radio lobes, which corresponds to the emissions originated within the cocoon, is a well-known characteristic of AGN jets (see §1.2.1). In any case, there is no direct evidence of the thermal emissions coming from the dilute thermal plasma within the cocoon. Therefore, little attention has been paid to the evolution of thermal temperature of the cocoon. In this chapter, based on the time-dependent dynamics of the cocoon expansion, we evaluate the thermal bremsstrahlung emissions from the cocoon. This leads to a new prediction of bright γ-ray emission from the young cocoon.

4.1 Thermal Evolution of Cocoon

The time-averaged mass and energy injections from the jet into the cocoon, which govern the cocoon pressure $P_{\rm c}$ and mass density $\rho_{\rm c}$ are approximately written as

$$\frac{\hat{\gamma}_c}{\hat{\gamma}_c - 1}\frac{P_{\rm c}(t)V_c(t)}{t} \approx 2T_{\rm j}^{01}(t)A_{\rm j}(t) \tag{4.1}$$

$$\frac{\rho_{\rm c}(t)V_c(t)}{t} \approx 2J_{\rm j}(t)A_{\rm j}(t), \tag{4.2}$$

where $T_{\rm j}^{01}$, $J_{\rm j}$ and $A_{\rm j}$, are the kinetic energy the mass flux, and the cross-sectional area of the jet, respectively. The total kinetic energy and mass flux of the jet are $T_{\rm j}^{01} = \rho_{\rm j}c^2\Gamma_{\rm j}^2 v_{\rm j}$, $J_{\rm j} = \rho_{\rm j}\Gamma_{\rm j}v_{\rm j}$ where $\rho_{\rm j}$, and $\Gamma_{\rm j}$ are mass density and bulk Lorentz factor of the jet (Blandford and Rees 1974). Hereafter we set $v_{\rm j} = c$. The total kinetic power of the relativistic jet is expressed in terms of $T_{\rm j}^{01}(t)$ and $A_{\rm j}(t)$ as $L_{\rm j} \equiv T_{\rm j}^{01}(t)A_{\rm j}(t)$. Although little attention has been payed to the mass injection Eq. (4.2), it is of great significance to take account of the Eq. (4.2) for deriving the cocoon temperatures. Hence we take up the the Eq. (4.2) to evaluate the temperatures of the cocoons. In contrast, the energy equation Eq. (4.1) has been widely

utilized in the literatures of the AGN bubbles in various ways (e.g., BC89; Dunn and Fabian 2004).

The jet is assumed to be cold since the hot plasma produced at the central engine usually cool down very quickly (e.g., Iwamoto & Takahara 2004). As for the mass and kinetic energy flux of powerful relativistic jets, numerical simulations tell us that no significant entrainment of the environmental matter takes place during the jet propagation (Scheck et al. 2002). According to this, the mass and kinetic energy flux of the jet are regarded as constant in time. Then, the conditions of $T_{\rm j}^{01} = {\rm const.}$, and $J_{\rm j} = {\rm const.}$ leads to the important relations of

$$\rho_{\rm j}(t) A_{\rm j}(t) = {\rm const}, \quad \Gamma_{\rm j}(t) = {\rm const}. \tag{4.3}$$

In fact, the constant $\Gamma_{\rm j}$ agrees with the relativistic hydrodynamic simulations (e.g., Marti et al. 1997; Scheck et al. 2002). We assume $A_{\rm h} = A_{\rm j}$ for the sake of simplicity throughout this chapter. In this case, the ram balance between the jet and the ambient ICM can be expressed by using the shock jump condition as $\Gamma_{\rm j}^2 \rho_{\rm j} = \beta_{\rm h}^2 \rho_{\rm ICM}$ (see Kawakatu and Kino 2006 for detail), where $\beta_{\rm h} = v_{\rm h}/c$ is the advance speed of the hot spot $\beta_{\rm h} = 10^{-2}\beta_{-2}$ (Liu et al. 1992; Scheuer 1995) and $\rho_{\rm ICM}$ is the mass density of ICM. Using, the jump condition, $L_{\rm j}$ is evaluated as

$$L_{\rm j} = 1.0 \times 10^{45}\ l_{\rm kpc}^2 \beta_{-2}^2 n_{-2}\ {\rm erg\ s^{-1}},$$

where we use $A_{\rm j}(t) = \pi l_{\rm hs}^2(t)$, and the hot spot radius $l_{\rm hs}$ is given by $l_{\rm kpc} = l_{\rm hs}(10^7\ {\rm yr})/1\ {\rm kpc}$. As a fiducial case, we set the number density of surrounding ICM as $n_{\rm ICM}(d) = \rho_{\rm ICM}(d)/m_p = 10^{-2}\ {\rm cm^{-3}} n_{-2} (d/30\ {\rm kpc})^{-2}$ where d is the distance from the center of ICM and cocoon. Since the change of the index from -2 does not change the essential physics discussed in this work, we focus on this case for simplicity. Since $2L_{\rm j}$ is the ultimate source of the phenomena associated with the cocoon, all of the emission powers which will appear in §4.2 should be less than $2L_{\rm j}$.

Considering the dynamical expansion of cocoon, we adopt the model described in §2.1 under the assumption of constant aspect ratio ($\mathcal{R} = {\rm const}$). Since the power-law index is given by $\alpha = 2$, the evolution of $A_{\rm j} (= A_{\rm h})$ is given by constant θ (see Fig.2.1), namely constant $l_{\rm hs}/r_{\rm h}$ in time, and also the hot spot advance velocity is constant in time ($\beta_{\rm h} = {\rm const}$). Hence, $r_{\rm h}$ and $l_{\rm hs}$ satisfies $r_{\rm h}(t) = \beta_{\rm h} ct$ and $l_{\rm hs}(t) = r_{\rm h}(t) {\rm tan}\theta = 1/30 (l_{\rm kpc}/r_{30}) \beta_{\rm h} ct$, where $r_{30} = r_{\rm h}(10^7\ {\rm yr})/30\ {\rm kpc}$, respectively. The number density of total electrons in the cocoon $n_e(t)$ is governed by the cocoon geometry and its plasma content. For convenience, we define the ratio of "the volume swept by the unshocked relativistic jet" to "the volume of the cocoon" as $\mathcal{A}(t)$. $\mathcal{A}(t)$ is evaluated as

$$\mathcal{A}(t) \equiv \frac{2 A_{\rm j}(t) v_{\rm j} t}{V_{\rm c}(t)} \approx 0.4\ \mathcal{R}^{-2} l_{\rm kpc}^2 r_{30}^{-2} \beta_{-2}^{-1}. \tag{4.4}$$

Note that, in the case, the time dependence of $\mathcal{A}$ is deleted since $V_{\rm c} \propto t^{-3}$ and $A_{\rm j} \propto t^2$. We stress that this case satisfies the observational indication of $v_{\rm hs} = {\rm const}$ (e.g., Conway 2002).

Eq. (4.4) tells us that $\mathcal{A}$ is of order unity. Actually it is seen in some numerical simulations (e.g., in Fig. 2 of Scheck et al. 2002). The cocoon mass density $\rho_c(t)$ is controlled by the mass injection by the jet and it can be expressed as

$$\begin{aligned} \rho_{\rm c}(t) &\approx \Gamma_{\rm j}\rho_{\rm j}(t)\mathcal{A} \\ &= \beta_{\rm h}^2\Gamma_{\rm j}^{-1}\rho_{\rm ICM}(r_{\rm h}(t))\mathcal{A}, \end{aligned} \tag{4.5}$$

where we use the shock condition of $\Gamma_{\rm j}^2\rho_{\rm j} = \beta_{\rm h}^2\rho_{\rm ICM}$. Adopting typical quantities of FR II sources (Begelman, Blandford & Rees 1984; Miley 1980; Bridle & Perley 1984), we obtain

$$n_e(t) \approx 4\times10^{-5}\bar{\mathcal{A}}n_{-2}\Gamma_{10}\beta_{-2}^2\left(\frac{t}{10^7\ {\rm yr}}\right)^{-2}{\rm cm}^{-3} \tag{4.6}$$

where $\Gamma = 10\Gamma_{10}$, and $\bar{\mathcal{A}} = \mathcal{A}/0.4$. Here we assume that the mass density of the $e^{\pm}$ pair plasma is heavier than that of electron-proton one, and then we adopt $\rho_{\rm c} \approx 2m_e n_e$ in the light of previous works (Reynolds et al. 1996; Wardle et al. 1998; Sikora & Madejski 2000; Kino & Takahara 2004). However, the mixture ratio of $e^{\pm}$ pair and electron-proton is still open. If we assume completely pure electron-proton content in the jet, too small n_e is required and it conflict with that of non-thermal electrons (Kino & Takahara 2004).

Let us estimate the electron (and positron) temperature (T_e) and proton temperature (T_p). From Eqs. (4.1) and (4.2) together with the equation of state

$$P_{\rm c} \approx 2n_e kT_e, \tag{4.7}$$

we can directly derive the temperatures as

$$kT_e \approx 1\ \Gamma_{10}\ {\rm MeV}, \quad kT_p \approx 2\ \Gamma_{10}\ {\rm GeV} \tag{4.8}$$

where we adopt the two temperatures condition of $kT_e \approx (m_e/m_p)kT_p$. It should be stressed that the temperatures are governed only by $\Gamma_{\rm j}$. It is also worth noting that the geometrical factors in Eqs. (4.1) and (4.2) are completely canceled out. Actually, the $\Gamma_{\rm j}$ dependence of Eq. (4.8) well coincide with the result of hydrodynamic simulations of relativistic outflows (Fig. 5 in Martí et al. 1997). One can naturally understand these properties by comparing the well-established properties such as supernovae and GRBs. Constant temperature in AGN jet can be realized by the "continuous" energy injection into the expanding cocoon whilst temperatures of astrophysical explosive sources such as gamma-ray bursts and supernovae would be decreased because of "impulsive" injection of the energy. Since the shock dissipation of the relativistic flow into non-relativistic one, in general, requires the energy conversion of whole kinetic energy density $\Gamma_{\rm j}\rho_{\rm j}c^2$ into internal one (Piran 1999). Thus the resultant temperatures are uniquely governed by $\Gamma_{\rm j}$ and they remain to be constant in time. Similarly, in the studies of

continuous stellar winds, the constant temperature has been predicted for a hot interior consist of the shocked wind (Weaver et al. 1977).

Here we examine the time scale of the Coulomb interaction between protons and electrons. The time-scale of energy transfer from the protons to electrons is given by $t_{ep} \approx (n_p \sigma_t c)^{-1}$ where $\sigma_t = 4\pi(e^2/kT_e)^2 \ln \Lambda_c$ is the transport cross section for electron-proton collision. The coulomb logarithm is written as $\ln \Lambda_c \approx \ln(3kT_e\lambda_D/e^2)$ where $\lambda_D = (kT_e/4\pi n_e e^2)^{1/2}$ is the Debye length (Totani 1998). A typical case of hot spots in AGN jets, we obtain $\ln \Lambda_c \sim 50$. Therefore, even using the maximal proton number density $n_p \approx n_e$, t_{ep} satisfies

$$\frac{t_{ep}(t)}{t} \sim 5 \times 10^3 \, \Theta_{10}^2 \bar{n}_e^{-1} \left(\frac{t}{10^7 \text{ yr}} \right) \tag{4.9}$$

where $\Theta_e \equiv kT_e/m_e c^2 = 10\Theta_{10}$, and $\bar{n}_e \equiv n_e(10^7 \text{ yr})/4 \times 10^{-5} \text{ cm}^{-3}$, are the electron temperature in unit of $m_e c^2$, and normalized number density of thermal electrons, respectively. As mentioned before, recent studies suggest the existence of large amount of $e^{\pm}$ pairs in AGN outflows which lead to much smaller n_p. Hence Eq. (4.9) shows the minimum value of $t_{ep}(t)/t$. Thus the energy transfer from protons to electrons is inefficient by the Coulomb coupling unless the cocoon is much younger than $t \sim 10^4$ yr.

Next we evaluate the time scale of thermal bremsstrahlung cooling in the cocoons. It is well known that thermal bremsstrahlung is inefficient for the dilute plasma since its emissivity shows $\propto n_e^2(t)$ where $n_e(t)$ is the electron number density in the cocoon. For the shock-heated electrons with the temperature of $\Theta_e \approx \Gamma_{\rm j}$, the cooling time of the bremsstrahlung per unit volume is estimated as $t_{\rm brem} \approx \Gamma m_e c^2 n_e / \epsilon_{\rm brem}$ where the bremsstrahlung emissivity in the relativistic regime is $\epsilon_{\rm brem} = 1.3 \times 10^{-22} \Theta_e^{1/2} n_e^2 (1 + 2.6\Theta_e)$ erg cm^{-3} s^{-1} with the Gaunt factor of 1.2 (Rybicki & Lightman 1979). The condition of $t_{\rm brem}(t) > t$

$$\frac{t_{\rm brem}(t)}{t} \approx 5 \times 10^4 \, \Theta_{10}^{-1/2} \bar{n}_e^{-1} \left(\frac{t}{10^7 \text{ yr}} \right) \tag{4.10}$$

actually holds. Therefore most of the shock dissipation energy is deposited into the cocoon without suffering strong radiative cooling and our treatment of adiabatic energy injection in Eq. (4.1) is verified for $t < t_{\rm brem}(t)$. We limit our attention on this case in the present work.

On the thermalizations of electrons and protons, it is worth to refer the recent studies with the particle-in-cell (PIC) simulations, since we only examine the simple case of the classical Coulomb interaction. PIC simulations begin to shed light on the complicated microscopic dynamics with in the relativistic collisionless shock. Using one-dimensional PIC simulations, Shimada & Hoshino (2000) revealed that the collision and merging processes among the coherent waves are accompanied by the strong thermalization of electrons. The results of three-dimensional PIC simulations (Nishikawa et al. 2003; Frederiksen et al. 2004) also tell us that electron populations are quickly thermalized whilst ion population tend to retain distinct bulk

speed and thermalize slowly. In the result of Shimada & Hoshino (2000), (Fig. 4 in their paper), we see that the proton energy is transferred to the electrons, then the electrons are heated-up by protons. To sum up, PIC simulations imply the quick thermalization of electron populations by plasma waves and their associated instabilities such as the two-stream instability. Therefore, our estimate of T_e would correspond to the lower limit of T_e. It is not the purpose of the present study to derive more realistic T_e in detail.

4.2 Emissions from a Young Cocoon

4.2.1 Thermal MeV bremsstrahlung emission

The time-dependence of the thermal bremsstrahlung luminosity $L_{\rm brem}$ is given by $L_{\rm brem}(t) \propto n_e^2(t) T_e^{3/2} V_{\rm c}(t) \propto t^{-1}$ based on the cocoon expansion shown in the previous section. Hence it is clear that a younger cocoons are brighter bremsstrahlung emitters than older cocoons. In a similar way, brighter synchrotron luminosity has been expected for younger radio galaxies (Readhead et al. 1996; Begelman 1996). With relativistic thermal bremsstrahlung emissivity (Rybicki & Lightman 1979), the luminosity of the optically thin thermal bremsstrahlung emission νL_ν at energies $\sim 1\ {\rm MeV}$ is estimated as

$$L_{\rm brem}(t) \approx 2 \times 10^{40}\ \bar{n}_e^2 \mathcal{R}^2 \Theta_{10}^{3/2} \left(\frac{t}{10^7\ {\rm yr}} \right)^{-1}\ {\rm erg\ s^{-1}}. \tag{4.11}$$

Here we omit the redshift (z) factor merely for simplicity. Eq. (4.11) explains the reasons why for the no detection of the thermal emission from older cocoons. One is simply because it is not very bright. The other is because the predicted energy range is $\sim 1\ {\rm MeV}$, the MeV-γ astronomy is still immature and it is sometimes called as "sensitivity gap" compared with the energy range below 10 keV and above GeV ranges (Takahashi et al. 2004).

For example, the bremsstrahlung emission from the cocoon located at a typical distance of $D = 10^3\ {\rm Mpc}$ (O'Dea & Baum 1997) is examined here. In Fig. 1, we show the predicted values of νF_ν for the cocoons with $t = 10^7\ {\rm yr}$ and $t = 10^4\ {\rm yr}$. The cocoon with $t = 10^7\ {\rm yr}$ have $\nu F_\nu \sim 10^{-14}\ {\rm erg\ cm^{-2} s^{-1}}$. The detection threshold of SPI instrument on board the INTEGRAL satellite is about $\nu F_\nu \sim 10^{-9}\ {\rm erg\ cm^{-2} s^{-1}}$ at $\sim 1\ {\rm MeV}$. For a young cocoon with $t = 10^4\ {\rm yr}$, the predicted luminosity is $\sim 10^3$ times larger than that $\nu F_\nu \sim 10^{-11}\ {\rm erg\ cm^{-2} s^{-1}}$. This is still less than the threshold of INTEGRAL. This may be the reason why no clear detection of MeV emission from young cocoons up to now. Fig. 1 shows that the XMM/Newton satellites can detect the low energy part of the thermal bremsstrahlung from young cocoons in principle. Hence some of extragalactic unidentified X-ray sources could be attributed as the low energy tail of the bremsstrahlung emissions. Interestingly, the recent observation by XMM/Newton reveals that the spectrum of young radio-loud AGN B1358+624 actually shows the power-law slope close to the bremsstrahlung's one (Vink at al. 2006).

In MeV energy band, a proposed mission of detector SGD on board the NeXT satellite with the eye up to ~ 0.6 MeV (Takahashi et al. 2004) could detect the thermal MeV emission from those located slightly closer and/or younger with smaller Lorentz factor. Lastly, other future mission, Advanced Compton Telescope (ACT), is worth to be noticed. The sensitivity of ACT is expected to be a significantly improved compared with INTEGRAL one (http://heseweb.nrl.navy.mil/gamma/detector/3C /3C_sens.htm). Although they focus on the super-nova science (Milne et al. 2002) for the moment, the ACT would be a promising tool also for the young cocoon science.

At a glance, one may think it hard to distinguish overlapping emissions from the core of the AGN with limited spacial angular resolution of current satellites. Time variabilities of observed spectra is the key to distinguish them. It is obvious that the cocoon emission is constant in time whilst various emissions from the core of AGN should be highly variable. Hence steady emissions are convincingly originated in cocoons. Furthermore, the averaged spectral index of AGN core emissions at X-ray band (Koratkar and Blaes 1999; Kawaguchi et al. 2001) are softer than the bremsstrahlung emission discussed in the present work. Hence the difference of the spectral index is also a useful tool to figure out the origin of the emission.

4.2.2 Non-thermal emissions

Non-thermal emission from AGN jets is another key ingredient to investigate their physics. Non-thermal synchrotron emission from the radio lobes due to the relativistic electrons is well known characteristic of AGN jets (Miley 1980; Bridle and Perley 1984). Recently, inverse-Compton (IC) emissions from large scale jets have been also intensively explored both theoretically and observationally (e.g., Celotti & Fabian 2004; Croston et al. 2005).

The properties of IC emissions from young cocoons is discussed here. For this purpose, we firstly consider the properties of the synchrotron emission. The magnetic flux conservation is assumed here during the jet propagation which is given by

$$B_{\rm hs}(t) l_{\rm hs}^{Y}(t) = const. \quad (1 \leq Y \leq 2)$$

where Y is a parameter expressing the configuration of the magnetic field in the hot spot. The magnetic flux from the central engine is assumed to be constant in time. The case of constant $Y = 1$ shows the purely toroidal-dominated magnetic field whilst $Y = 2$ is relevant to the purely poloidal-dominated magnetic field. Using Y, the time dependence of the synchrotron luminosity at the hot spot $L_{\rm hs,syn}(t)$ may be given by $L_{\rm hs,syn}(t) \propto l_{\rm hs}^{3}(t)\gamma^{2}B_{\rm hs}^{2}(t)n_{e}^{\rm NT}(\gamma,t) \propto t^{-2Y+1}$ where we assume that the number density of the non-thermal electrons $n_{e}^{\rm NT}(\gamma,t)$ is proportional to $n_e(t)$, and γ is constant in time because the synchrotron cooling time tend to be longer than the sound crossing time at the hot spot (e.g., KT04). Taking the observational fact of the large number of the CSOs in spite of their young age, the larger synchrotron luminosity

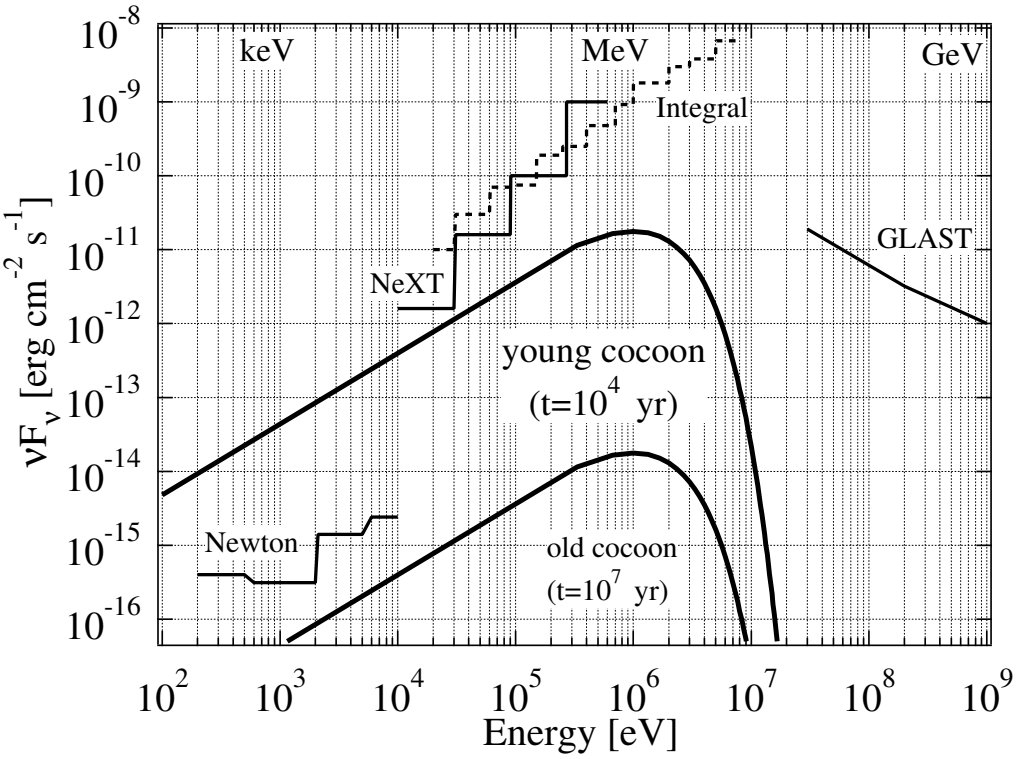

Figure 4.1: Model prediction of MeV-peaked thermal bremsstrahlung emission from cocoons located at $D = 10^3$ Mpc. The predicted emission from young cocoon is brighter enough to detect in X-ray band whilst that from an old cocoon is much darker than the detection limits (Hasinger et al. 2001; Roques et al. 2003; Takahashi et al. 2004).

is required for younger sources (Begelman 1996; Readhead at al. 1996). Qualitatively, the model well reproduce this observational properties of young radio galaxies.

To evaluate IC emission of the cocoon, it may be useful to define the quantities of $f_{\rm ssc}(t) \equiv U_{\rm ssc}(t)/U_{\rm syn}(t)$ and $f_{\rm IC/CMB}(t) \equiv U_{\rm IC/CMB}(t)/U_{\rm syn}(t)$, where $U_{\rm syn}$, $U_{\rm ssc}$, and $U_{\rm IC/CMB}$, are the energy densities of synchrotron photons, those of synchrotron-self Compton (SSC), and those of IC scattering of the Cosmic-Microwave Background (CMB), respectively. Photons with larger density is the dominant seed photons for IC scattering. We denote that the IC luminosities for synchrotron photons and the CMB as $L_{\rm ssc}$ and $L_{\rm IC/CMB}$, respectively.

For $U_{\rm ssc}(t) < U_{\rm CMB}$, we see that $f_{\rm IC/CMB}(t) \propto t^{2Y}$ which implies that younger cocoon produce less IC/CMB photons in contrast to the case of bremsstrahlung ones. It is of great importance to examine whether the predicted frequency of IC/CMB emission overlapping in MeV band or not. According to the standard diffusive shock acceleration, the acceleration time scale

is estimated as $t_{\rm acc} = (20\xi\gamma_e m_e c)/(3eB_{\rm hs})$, where ξ is the parameter characterizing the mean free path for the scattering (e.g., Drury 1983). The maximum Lorentz factor of electrons γ can be obtained by the equating $t_{\rm acc}$ to the synchrotron cooling time $t_{\rm syn} = (6\pi m_e c^2)/(\sigma_{\rm T}\gamma c B_{\rm hs}^2)$. This shows the $B_{\rm hs}$ dependence of γ as

$$\gamma(t) \propto B_{\rm hs}^{-1/2}(t). \tag{4.12}$$

Assuming that the strength of magnetic field in the cocoon $B(t)$ is proportional to the one in the hot spot, the maximum frequency of the IC/ICM emission $\nu_{\rm IC/CMB} \propto \gamma^2\nu_{\rm CMB}$ can be estimated as

$$\nu_{\rm IC/CMB}(t) \sim 1\times10^{19}\gamma_4^2\left(\frac{t}{10^7\ {\rm yr}}\right)^Y\ {\rm Hz}, \tag{4.13}$$

where we denote $B(t) \propto B_{\rm hs}(t) \propto l_{\rm hs}^{-Y}(t) \propto t^{-Y}$, $\gamma(t) = 10^4\gamma_4(t/10^7\ {\rm yr})^{Y/2}$, and $\gamma_4 = \gamma/10^4$. The typical value of γ is adopted from Blandford et al. (1990). From this, one can find that $\nu_{\rm IC/CMB}(t)$ of young cocoons much smaller than $1\ {\rm MeV} = 2\times10^{20}$ Hz.

In the case of $U_{\rm syn}(t) > U_{\rm CMB}$, the behavior of $U_{\rm syn}(t)$ is given by $L_{\rm syn}(t) \propto cZ_{\rm h}^2(t)U_{\rm syn}(t) \propto \epsilon_{\rm syn}(t)V_{\rm c}(t)$. From this we obtain $U_{\rm syn}(t) \propto U_{\rm B}(t)t^{-1}$. The model predicts that $f_{\rm ssc}(t) \propto t^{-1}$ in time and younger cocoon yields more SSC photons. Using this, $L_{\rm ssc}$ can be estimated as $L_{\rm ssc}(t) \propto t^{-2Y}$. The maximum frequency of the SSC emission $\nu_{\rm ssc}$ can be evaluated with Eq. (4.12). $\nu_{\rm ssc} \sim \gamma^2\nu_{\rm syn} \sim 1\times10^6\ \gamma^4 B$ Hz can be evaluated as

$$\nu_{\rm ssc}(t) \sim 1\times10^{17}\gamma_4^4 B_{-5}\left(\frac{t}{10^7\ {\rm yr}}\right)^Y\ {\rm Hz} \tag{4.14}$$

where we use Eq. (4.12) and the typical value of B is set as $B(t) = 10^{-5}\ B_{-5}(t/10^7\ {\rm yr})^{-Y}$ G based on Blandford et al. (1990). Thus, it is found that non-thermal emissions from younger cocoon reside in much lower energy band than MeV.

Chapter 5

EMISSIONS FROM SHELL

As mentioned in §1.2.2, recent X-ray observations enabled to resolve the bow shock associated with the cavities. In theoretical point of view, large number of analytical models has been proposed to describe the evolution of overpressured cocoons and their non-thermal emissions (e.g. Scheuer 1974; Begelman 1996; Kaiser & Alexander 1997; Bicknell et al. 1997; Blundell et al. 1999; Manolakou & Kirk 2002; KK05). However, relatively few of them focused on the evolution of the shell composed of shocked ambient gas (e.g. Heinz et al. 1998; Kaiser & Alexander 1999; Alexander 2002).

In this chapter, we explore emissions from the shells based on the model given in §2.2. Bremsstrahlung emission from shock heated thermal electrons and synchrotron emission from shock accelerated non-thermal electrons are considered. As for the thermal bremsstrahlung emission, we evaluate the effect of radiative coolings on the dynamics. As for the non-thermal synchrotron emission, we evaluate the spectrum by using the parameters ϵ_e which gives the fraction of shock dissipated energy converted into that of non-thermal electrons and ξ which characterizes mean free path of electrons for scattering. We also discuss how the observation of synchrotron emission can be used as a probe for the physics of electron acceleration.

5.1 Mach Number Limit

Since we assume that the bow shock is strong, our model is not applicable when the Mach number of expansion velocity, $\mathcal{M} \equiv \dot{R}/c_{\rm s}$, is low. Here $c_{\rm s}$ is the sound speed of the ambient medium which is given by $c_{\rm s} = [(\hat{\gamma}_{\rm a} k_{\rm B} T_{\rm a})/(\mu m_{\rm H})]^{1/2}$. In the present study, we set $\mathcal{M} = \mathcal{M}_*$ as the lower limit of Mach number in our model and only focus on the phase when the condition $\mathcal{M} > \mathcal{M}_*$ is satisfied. We define the transition time $t_{\mathcal{M}}$ to be the time when $\mathcal{M} = \mathcal{M}_*$ is satisfied. Under assumption of isothermal ambient medium ($T_{\rm a} = {\rm constant}$), $t_{\mathcal{M}}$ is derived as

$$t_{\mathcal{M}} = C_M \, r_0^{\alpha/(\alpha-2)} \left(\frac{L_{\rm j}}{\rho_0}\right)^{1/(2-\alpha)} (k_{\rm B} T_{\rm a})^{(5-\alpha)/(2\alpha-4)} \mathcal{M}_*^{(\alpha-5)/(2-\alpha)}, \tag{5.1}$$

where

$$C_M = \left[\frac{3C_R}{5-\alpha} \left(\frac{\mu m_{\rm H}}{\hat{\gamma}_{\rm a}} \right)^{1/2} \right]^{(5-\alpha)/(2-\alpha)}, \tag{5.2}$$

Since the time-dependence of the Mach number is given by $\mathcal{M} \propto \dot{R} \propto t^{(\alpha-2)/(5-\alpha)}$. When $\alpha < 2$, which corresponds to the case we focus in the present study, $\mathcal{M}$ decreases with time. Hence, our model becomes invalid when $t > t_{\mathcal{M}}$. Note that $\alpha = 2$ corresponds to the case of constant $\mathcal{M}$ and therefore $t_{\mathcal{M}}$ cannot be determined.

5.2 Evolution of Radiation From Shell

Here we consider the temporal evolution of bremsstrahlung radiation from thermal electrons and synchrotron radiation from non-thermal electrons from the obtained solution in §2.2. Hereafter, we focus on the case of $0 \leqq \alpha \leqq 2$, fairly wide range which is expected in the environment of radio sources.

5.2.1 Thermal bremsstrahlung emission

Since the temperature of ISM and ICM in which radio sources are embedded is typically $\sim \mathrm{keV}$, $T_{\rm s}$ is higher than keV. Above keV, emission from dilute (optically thin) plasma is expected to be dominated by thermal bremsstrahlung (e.g., Raymond et al. 1976). The emissivity of thermal bremsstrahlung is well approximated as $\epsilon_{\rm brem} \approx 3.0 \times 10^{-27} n_{\rm e} n_{\rm p} T^{1/2} \mathrm{erg\ cm^{-3}\ s^{-1}}$, where $n_{\rm e}$ and $n_{\rm p}$ are the number density of electrons and protons, respectively, and T is the temperature (Rybicky & Lightman 1979). Hence, total luminosity from the shell is given by

$$L_{\rm brem} = \epsilon_{\rm brem} 4\pi R^2 \delta R \ \propto \ \rho_{\rm s}^2 T_{\rm s}^{1/2} R^3 \ \propto \ t^{(7-5\alpha)/(5-\alpha)}. \tag{5.3}$$

In the above equation we have used Eqs. (2.10), (2.13), and (2.14).

$L_{\rm brem}$ increases with time, for $\alpha < 7/5$ and, on the other hand, decreases for $\alpha > 7/5$. This tendency can be understood as follows. When density gradient is shallow ($\alpha < 7/5$), $L_{\rm brem}$ increases since the growth in the volume of the shell ($\propto R^3$) can dominate over the decrease of emissivity ($\propto \rho_{\rm s}^2 T_{\rm s}^{1/2}$), and opposite is true for steeper density gradient ($\alpha > 7/5$). In the case of $\alpha = 7/5$, decrease in emissivity is balanced by the increase in the volume and $L_{\rm brem}$ maintains a constant value throughout the evolution. In the case of $\alpha = 7/5$, $L_{\rm brem}$ maintains a constant value throughout the evolution.

Considering the effects of radiation on the dynamics of the shell, radiative cooling becomes non-negligible when cooling timescale is shorter than the dynamical timescale. The cooling

timescale of the shell is estimated as $t_{\rm brem} = E_{\rm s}/L_{\rm brem}$. Thus, from Eqs. (2.16) and (5.3), the ratio of the cooling time to the dynamical time is given by

$$\frac{t_{\rm brem}}{t} = \frac{fL_{\rm j}}{L_{\rm brem}} \propto t^{(5\alpha-7)/(5-\alpha)}. \tag{5.4}$$

Since $fL_{\rm j}$ is constant, the time dependence of $t_{\rm brem}/t$ is determined by $L_{\rm brem}^{-1}$. When $L_{\rm brem}$ increases with time ($\alpha < 7/5$) cooling of the shell is negligible initially (adiabatic) and then eventually becomes becomes important (radiative). On the other hand, when $L_{\rm brem}$ decreases with time ($\alpha > 7/5$), shell is initially radiative and then becomes adiabatic. Thus, if we define the transition time $t_{\rm r}$ to be the time when $t_{\rm brem}$ is equal to t, the shell is classified as follows:

$$\begin{aligned} \frac{t_{\rm brem}}{t} &= \begin{cases} > 1 \ \text{adiabatic} & t < t_{\rm r} \\ < 1 \ \text{radiative} & t > t_{\rm r} \end{cases} \quad (\text{for } \alpha < 7/5), \\ &= \begin{cases} < 1 \ \text{radiative} & t < t_r \\ > 1 \ \text{adiabatic} & t > t_r \end{cases} \quad (\text{for } \alpha > 7/5). \end{aligned} \tag{5.5}$$

Note that in the case of $\alpha = 7/5$, shell is either always adiabatic or radiative depending on the value of $L_{\rm j}$, ρ_0 and r_0. However, the shell is always adiabatic in this case when reasonable values of for radio sources are substituted. When the shell becomes radiative, their width become thin as discussed in the case of shells in the stellar wind (e.g., Weaver et al. 1977). In this case although the large-scale expansion rate are expected to remain nearly unchanged, the adiabatic shock jump condition imposed in Eqs. (2.13) and (2.14) becomes invalid and need to be modified.

5.2.2 Synchrotron radiation

Since we consider a shocks propagating with a high Mach number, it is natural to assume that electrons are accelerated at the shock as in the case of a supernova remnant (SNRs). Here we evaluate the evolution of synchrotron emission from the non-thermal electron under assumption that a constant fraction, $\epsilon_e \equiv E^{\rm NT}/E_{\rm s}$, of total internal energy is converted into that of the non-thermal electrons, $E^{\rm NT}$, via diffusive shock acceleration (DSA) process (Bell 1978; Drury 1983; Blandford & Eichler 1987). Here we assume that the spatial distribution of magnetic field in the ambient medium is uniform and consider that the compressed magnetic field within the shell is constant in time.

Energy spectrum of non-thermal electrons

Based on the theory of DSA, we assume that the energy spectra of non-thermal electrons injected into the shock are given by

$$N(\gamma_e) = K\gamma_e^{-p} \ \text{ for } \ \gamma_{\rm min} \leqq \gamma_e \leqq \gamma_{\rm max}, \tag{5.6}$$

where γ_e is the Lorentz factor of non-thermal electron, and $\gamma_{\rm min}$ and $\gamma_{\rm max}$ correspond to the minimum and the maximum Lorentz factor, respectively. Index p depends on the compression ratio of the shock and are determined by $p = (3\hat{\gamma}_{\rm a} - 1)/2$ in the case of a strong shock. Since we deal with non-relativistic temperature (i.e., $\hat{\gamma}_{\rm a} = 5/3$) in the present study, $p = 2$ is obtained. In this case, the total energy of non-thermal electrons is well approximated by $E^{\rm NT} = \int_{\gamma_{\rm min}}^{\gamma_{\rm max}} (\gamma_e - 1) m_e c^2 N(\gamma_e) d\gamma_e \approx K m_e c^2 {\rm ln}\gamma_{\rm max}$, when $\gamma_{\rm max} \gg 1$ and $\gamma_{\rm min} \sim 1$ are assumed. Here m_e and c are the rest mass of electron and the speed of light, respectively. Hence, when $\gamma_{\rm max}$ and ϵ_e are given, K is obtained as

$$K \simeq \frac{\epsilon_e E_{\rm s}}{m_e c^2 {\rm ln}(\gamma_{\rm max})} \quad {\rm for} \quad p = 2. \tag{5.7}$$

Assuming the standard manner for the diffusion coefficient, acceleration time of the non-thermal electrons with Lorentz factor of γ_e is given by $t_{\rm acc}(\gamma_e) = [20\xi\gamma_e m_e c^3]/[3eB\dot{R}^2]$, where $-e$ and B are the electron charge and the magnetic field strength in the shell, respectively. The factor ξ depends on the mean free path of electrons. Using the above acceleration time, we estimate $\gamma_{\rm max}$ from the relation of $\gamma_{\rm max} = \min(\gamma_{\rm max1}, \gamma_{\rm max2})$, where $\gamma_{\rm max1}$ and $\gamma_{\rm max2}$ are the Lorentz factor of electron estimated by equating $t_{\rm acc}$ with the dynamical time t and synchrotron cooling time $t_{\rm syn}(\gamma_e) \sim \gamma_e^{-1}$, respectively, and are given by

$$\gamma_{\rm max1} = \frac{3eB\dot{R}^2}{20\xi m_e c^3} t \propto t^{(1+\alpha)/(5-\alpha)} \qquad \gamma_{\rm max2} = \left[\frac{9\pi e}{10B\sigma_{\rm T}\xi}\right]^{1/2} \frac{\dot{R}}{c} \propto t^{(\alpha-2)/(5-\alpha)}. \tag{5.8}$$

Since we are considering the case of $0 \leqq \alpha \leqq 2$, $\gamma_{\rm max1}$ increases with time, while $\gamma_{\rm max2}$ decreases or remains constant. Hence, in the early stage of evolution, $\gamma_{\rm max}$ is determined by $\gamma_{\rm max1}$, and, in the later stage, by $\gamma_{\rm max2}$. From Eq. (5.8), the transition time is derived as

$$t_{\rm br} = C_{\rm br}\, \xi^{(5-\alpha)/6} B^{(\alpha-5)/2} {r_0}^{\alpha/3} \rho_0^{1/3} L_{\rm j}^{-1/3}, \tag{5.9}$$

where

$$C_{\rm br} = \left[\frac{5(5-\alpha)^2 m_e^4 c^8}{3C_R^2\, e^5}\right]^{(5-\alpha)/6}. \tag{5.10}$$

Thus, $\gamma_{\rm max}$ is given as

$$\gamma_{\rm max} = \begin{cases} \gamma_{\rm max1} & {\rm for}\ \ t < t_{\rm br} \\ \gamma_{\rm max2} & {\rm for}\ \ t_{\rm br} < t \end{cases} \quad (0 \leqq \alpha \leqq 2). \tag{5.11}$$

In the later stage ($t_{\rm br} < t$), the effect of radiative cooling also modifies the high energy part of the injected spectrum of electrons in the following way. A Lorentz factor of electron which cools on the dynamical timescale is given by

$$\gamma_{\rm br} = \frac{6\pi m_e c}{\sigma_{\rm T} B^2 t} \propto t^{-1}, \tag{5.12}$$

where $\sigma_{\rm T}$ is the Thompson cross section. The electron spectrum with energy above $\gamma_{\rm br}$ steepens by 1 in the power-law index because the cooling time is inversely proportional to its energy ($t_{\rm syn} \propto \gamma_e^{-1}$). Hence, in the later stage, the energy spectrum is given by a form of broken-power law ($N(\gamma_e) \propto \gamma_e^{-(p+1)}$ for $\gamma_e > \gamma_{\rm br}$).

Spectrum of synchrotron radiation

As a result, reflecting the energy spectrum of electrons mentioned above, the synchrotron spectrum can classified in two cases as

$$\begin{aligned} L_\nu &= A(p)B^{(p+1)/2}K\nu^{-(p-1)/2} \quad (\nu < \nu_{\rm max}) \quad \text{for } t < t_{\rm br}, \\ &= \begin{cases} A(p)B^{(p+1)/2}K\nu^{-(p-1)/2} & (\nu < \nu_{\rm br}) \\ A(p)B^{(p+1)/2}K\nu_{\rm br}^{1/2}\nu^{-p/2} & (\nu_{\rm br} < \nu < \nu_{\rm max}) \end{cases} \quad \text{for } t_{\rm br} < t, \end{aligned} \tag{5.13}$$

where $\nu_e(\gamma_e) \simeq 0.29(3\gamma_e^2 eB)/(4\pi m_e c)$ is the typical frequency emitted from the electron with Lorentz factor $\gamma_{\rm e}$. $\nu_{\rm max}$ and $\nu_{\rm br}$ are the frequencies given by $\nu_e(\gamma_{\rm max})$ and $\nu_e(\gamma_{\rm br})$, respectively, Here $\nu_e(\gamma_e) \simeq 0.29(3\gamma_e^2 eB)/(4\pi m_e c)$ is the typical frequency emitted from the electron with Lorentz factor $\gamma_{\rm e}$. $A(p)$ is a function of p which is defined as

$$A(p) = \frac{(3\pi)^{1/2}e^3}{2m_e c^2}\left(\frac{2\pi m_e c}{3e}\right)^{-(p-1)/2}\frac{\Gamma(\frac{p}{4}+\frac{19}{12})\Gamma(\frac{p}{4}-\frac{1}{12})\Gamma(\frac{p}{4}+\frac{5}{4})}{(p+1)\Gamma(\frac{p}{4}+\frac{7}{4})}, \tag{5.14}$$

where Γ is the usual gamma function (see Appendix for detail).

Focusing on the case of $p = 2$, let us consider the evolution of luminosity νL_ν. From Eq. (5.13) the spectrum is expressed as

$$\nu L_\nu = L_{\rm peak}\left(\frac{\nu}{\nu_{\rm br}}\right)^{1/2} \quad (\nu < \nu_{\rm max}) \ \text{ for } t < t_{\rm br}, \tag{5.15}$$

$$\nu L_\nu = \begin{cases} L_{\rm peak}\left(\frac{\nu}{\nu_{\rm br}}\right)^{1/2} & (\nu < \nu_{\rm br}) \\ L_{\rm peak} & (\nu_{\rm br} < \nu < \nu_{\rm max}) \end{cases} \quad \text{for } t_{\rm br} < t. \tag{5.16}$$

Here $L_{\rm peak}$ is given by

$$L_{\rm peak} = A(2)B^{3/2}K\nu_{\rm br}^{1/2} = F\left\{\ln(\gamma_{\rm max})\right\}^{-1}\epsilon_e L_{\rm j} \tag{5.17}$$

where $F \simeq (2.8\pi^{1/2}A(2)f)/(m_e^{1/2}c^{3/2}\sigma_{\rm T})$. In deriving Eq. (5.17), we used Eqs. (2.16), (5.7), and (5.12). As is shown in Eq. (5.16), $L_{\rm peak}$ corresponds to the peak spectrum luminosity which extends from $\nu_{\rm br}$ to $\nu_{\rm max}$ for $t > t_{\rm br}$,. Since $L_{\rm peak}$ depend on $\gamma_{\rm max}$ logarithmically, they are quite insensitive to the variance in $\gamma_{\rm max}$. Therefore, we approximate as

$\ln(\gamma_{\rm max}) \approx {\rm constant}$ merely for simplicity from now on. Under the above assumption, we find that $L_{\rm peak}$ is a constant in time. This is simply because the increase in electron number due to the injection from the shock ($N(\gamma_{\rm e}) \propto K \propto t$) balances with the decrease due to the effect of radiative coolings for electrons with $\gamma_{\rm e} > \gamma_{\rm br}$. Moreover, it is worth noting that $L_{\rm peak}$ is solely determined by $L_{\rm j}$ and ϵ_e with linear dependence ($L_{\rm peak} \propto \epsilon_e L_{\rm j}$), and has no dependence on either ρ_0, r_0, or B. Independence on ρ_0 and r_0 are due to the independence of K and $\nu_{\rm br}$ on these quantities. On the other hand, independence on B is a consequence of the assumption of $p = 2$, since the dependence of L_ν on B for $\nu > \nu_{\rm br}$ is given by $L_\nu \propto B^{(p+1)/2}\nu_{\rm br}^{1/2} \propto B^{(p-2)/2}$. The temporal evolution of νL_ν is simply given as

$$\begin{aligned} \nu L_\nu &\propto t\nu^{1/2} \ (\nu < \nu_{\rm max}) && \text{for } t < t_{\rm br}, \\ &\propto \begin{cases} t\nu^{1/2} & (\nu < \nu_{\rm br}) \\ \text{constant} & (\nu_{\rm br} < \nu < \nu_{\rm max}) \end{cases} && \text{for } t_{\rm br} < t. \end{aligned} \tag{5.18}$$

The schematic picture of spectrum is shown in Fig 5.1. The evolution of spectrum is classified into two stages. In the initial stage ($t < t_{\rm br}$), the spectrum is given by single power-law. In this stage, the luminosity and the maximum frequency increase with time as $\nu L_\nu \propto t$ and $\nu_{\rm max} \propto t^{(2+2\alpha)/(5-\alpha)}$, respectively. In the later stage ($t_{\rm br} < t$), the spectrum is expressed by broken power-law with break frequency given by $\nu_{\rm br}$. νL_ν increases with linearly with time for frequencies below $\nu_{\rm br}$, whilst for frequencies above $\nu_{\rm br}$, remains constant. In this stage, the maximum and break frequencies decreases with time as $\nu_{\rm max} \propto t^{(2\alpha-4)/(5-\alpha)}$ and $\nu_{\rm br} \propto t^{-2}$, respectively.

Surface brightness distribution

Surface brightness of the shell is evaluated by integrating the emissivity along the line of sight. Since we are considering a uniform shell, the emissivity is given by $\epsilon_\nu = L_\nu/(4\pi R^2 \delta R)$. Hence, by defining $l(r)$ as the thickness of the shell at a distance r from the center of the system (see Fig. 2.2), the surface brightness is given by

$$\Sigma_\nu = \frac{1}{4\pi}\epsilon_\nu l(r), \tag{5.19}$$

where

$$l(r) = 2R \times \begin{cases} \left\{1 - \left(\frac{r}{R}\right)^2\right\}^{1/2} & \text{for } \ R - \delta R \le r \le R, \\ \left[\left\{1 - \left(\frac{r}{R}\right)^2\right\}^{1/2} - \left\{\left(1 - \frac{\delta R}{R}\right)^2 - \left(\frac{r}{R}\right)^2\right\}^{1/2}\right] & \text{for } \ 0 \le r \le R - \delta R. \end{cases}$$

Here we omit the redshift factor merely for simplicity. Fig. 5.2 shows the resultant radial profile of surface brightness at an arbitrary frequency and time. The brightness distribution is

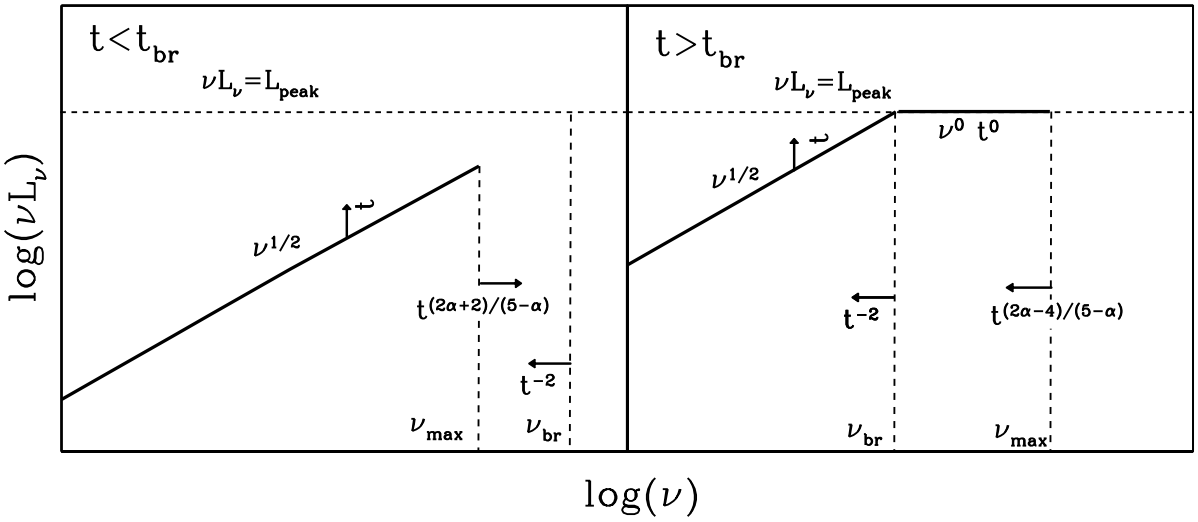

Figure 5.1: Evolution of synchrotron spectra from shock injected power-law electron distribution in the shell. The above and below panel corresponds to the early stage ($t < t_{\rm br}$) and later stage ($t < t_{\rm br}$) of the evolution, respectively.

relatively flat in the inner part ($r < R - \delta R$), and Σ_ν approaches asymptotically to $\Sigma_{\nu,0} \equiv \epsilon_\nu l(0)/(4\pi) = L_\nu/(8\pi^2 R^2)$ as r decreases. The brightness shows a sharp peak at $r = R - \delta R$, which corresponds to the radius of the contact discontinuity between the cocoon and the shell, and its value is given by $\Sigma_{\nu,\rm CD} = (2R/\delta R - 1)^{1/2}\Sigma_{\nu,0}$. In the outer part ($R - \delta R < r$), the brightness decreases abruptly and approaches zero at $r = R$.

5.3 Application to the Radio Sources

From the obtained results in the previous section, we apply the results obtained in the previous section to the radio sources. Hereafter, we set $\hat{\gamma}_{\rm c} = 4/3$, $\hat{\gamma}_{\rm a} = 5/3$, and $\mu = 0.6$.

5.3.1 On the radiative cooling by thermal bremsstrahlung

Radio sources are embedded in X-ray emitting hot gas with temperature of $k_{\rm B}T_{\rm a} \sim {\rm keV}$ in elliptical galaxies and clusters. The large scale density distribution of these hot gas is usually fitted by β-model which takes the form of $\rho_{\rm a}(r) = \rho_0[1 + (r/r_0)^2]^{-\alpha/2}$, where r_0 is the core radius (e.g., Mulchaey & Zabludoff 1998; Fukazawa et al. 2004). Therefore, environment in the scale larger than r_0 can be approximated by the form we have imposed in the previous sections ($\rho_{\rm a} = \rho_0(r/r_0)^\alpha$). On the other hand, roughly constant density is expected in the scale

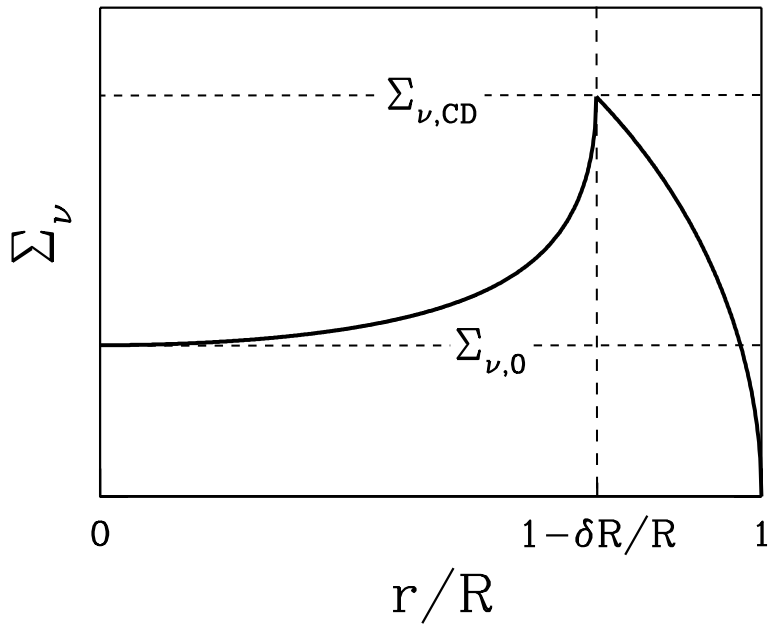

Figure 5.2: The radial profile of surface brightness at an arbitrary time and frequency. $\Sigma_{\nu,0}$ and $\Sigma_{\nu,\mathrm{CD}}$ is the surface brightness at $r = 0$ and $r = R - \delta R$, respectively.

smaller than r_0 from the model. Since the core radius of elliptical galaxies is typically $\sim$ kpc, here we discuss the effect of of radiation cooling in the source with size $R > \mathrm{kpc}$ and $R < \mathrm{kpc}$ separately.

First, we consider radio sources with size of kpc-Mpc scale. Here we set the density gradient as $\alpha = 1.5$ since it corresponds to typical value at this scale. In this case, the evolution of R is given by

$$R(t) \approx 2.2 \times 10 r_{\mathrm{kpc}}^{-3/7} \rho_{0.1}^{-2/7} L_{45}^{2/7} t_7^{6/7} \ \mathrm{kpc}, \tag{5.20}$$

where $\rho_{0.1} = \rho_0/0.1 m_{\mathrm{H}}\ \mathrm{cm}^{-3}$, $r_{\mathrm{kpc}} = r_0/1\ \mathrm{kpc}$, $L_{45} = L_{\mathrm{j}}/10^{45}\ \mathrm{ergs\,s}^{-1}$, and $t_7 = t/10^7\ \mathrm{yr}$ respectively. The chosen fiducial parameters are fairly typical condition for external medium of radio sources.

By setting the limit of Mach number as $\mathcal{M}_* = 2\mathcal{M}_2$ (§5.1), $t_{\mathcal{M}}$ is given by $t_{\mathcal{M}} \approx 4.8 \times 10^8\ \mathrm{yr}\ r_{\mathrm{kpc}}^{-3} \rho_{0.1}^{-2} L_{45}^2 T_{\mathrm{keV}}^{-7/2} \mathcal{M}_2^{-7}$, where $T_{\mathrm{keV}} = k_{\mathrm{B}} T_{\mathrm{a}}/1\ \mathrm{keV}$. The corresponding radius $R_{\mathcal{M}} \equiv R(t_{\mathcal{M}})$ are given by $R_{\mathcal{M}} \approx 6.1 \times 10^2\ \mathrm{kpc}\ r_{\mathrm{kpc}}^{-3} \rho_{0.1}^{-2} L_{45}^2 T_{\mathrm{keV}}^{-3} \mathcal{M}_2^{-6}$. From Eq. (5.5), the shell is radiative when $t < t_{\mathrm{r}}$ and becomes adiabatic in the later stage. The transition time t_r is estimated by $t_{\mathrm{r}} \approx 2.2 \times 10^{-14}\ \mathrm{yr}\ r_{\mathrm{kpc}}^{18} \rho_{0.1}^{12} L_{45}^{-5}$, where we approximated the number density of

electrons and protons as $n_{\rm e} = n_{\rm peak} \approx 0.5\rho_{\rm s}/\mu m_{\rm H}$ when evaluating $L_{\rm brem}$. The corresponding radius, $R_{\rm r} \equiv R(t_{\rm r})$, is given by $R_{\rm r} \approx 4.3 \times 10^{-17}$ kpc $r_{\rm kpc}^{15}\rho_{0.1}^{10}L_{45}^{-4}$. Hence, conditions for the shell to have radiative regime when $R(t) > {\rm kpc}$ are given by $R_{\rm r}, R_{\mathcal{M}} \gtrsim {\rm kpc}$. These conditions are written as

$$\rho_{0.1} \lesssim 2.5 \times 10\, r_{\rm kpc}^{-3/2} T_{\rm keV}^{-3/2} \mathcal{M}_2^{-3} L_{45} \quad \rho_{0.1} \gtrsim 4.3 \times 10\, r_{\rm kpc}^{-3/2} L_{45}^{2/5}. \tag{5.21}$$

Clearly, the fiducial parameters do not satisfy the above criterion. In Fig. 5.3, the range which satisfy the above condition is displayed as shaded region. The figure is illustrated under assumption of $r_0 = 1{\rm kpc}$, $T_{\rm a} = 1{\rm keV}$, and $\mathcal{M}_* = 2$. The shaded region corresponds to the range where Eq. (5.21) is satisfied. Quite large power and ambient density are required for the shell to have radiative regime. Since these parameter ranges are quite unlikely, it is confirmed that radiative regime can be discarded for the radio sources with size of $R > 1{\rm kpc}$.

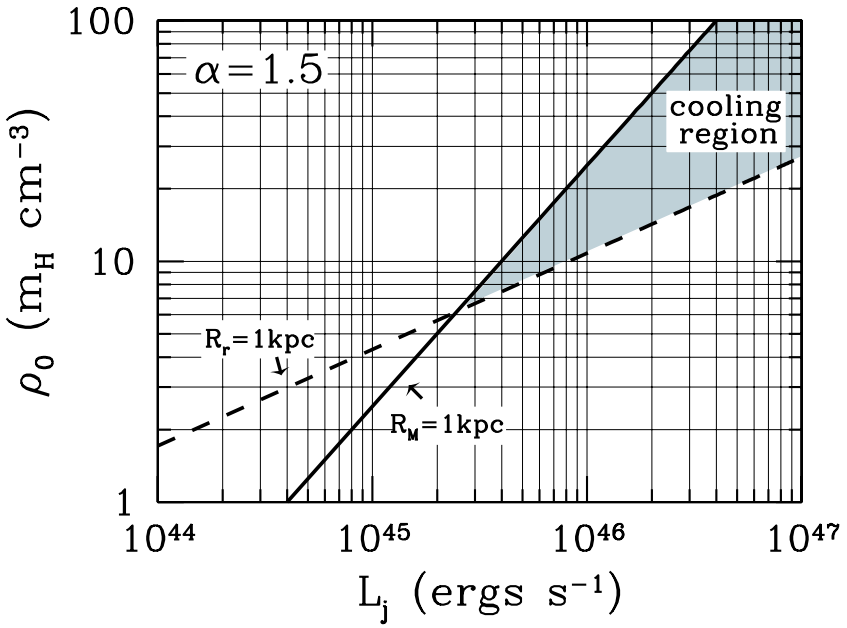

Figure 5.3: The ranges of $L_{\rm j}$ and ρ_0 which satisfy Eq. (5.21) in the case of $\alpha = 1.5$. Here $r_0 = 1{\rm kpc}$, $T_{\rm a} = 1{\rm keV}$, and $\mathcal{M}_* = 2$ are assumed. The solid line represents $R_{\mathcal{M}} = 1{\rm kpc}$. The dashed line represents $R_{\rm r} = 1{\rm kpc}$. The regions below the solid line and above the dashed line correspond to region of $R_{\mathcal{M}} > 1{\rm kpc}$ and $R_{\rm r} > 1{\rm kpc}$, respectively. The shaded region shows the ranges of $L_{\rm j}$ and ρ_0 where $R_{\mathcal{M}}, R_{\rm r} > 1{\rm kpc}$ are satisfied.

Note that the above result is insensitive to the change of density gradient α from 1.5. When α is in the range of $7/5 < \alpha$, similar result can be derived from the same procedure. On the

other hand, in the case of $\alpha < 7/5$, different criterion must be considered since the radiative regime corresponds to the later stage ($R(t) > R_{\rm r}$). In this case, the conditions for the shell to have radiative regime when $R(t) > {\rm kpc}$ are given by $R_{\mathcal{M}} \gtrsim {\rm kpc}$ and $R_{\mathcal{M}} \gtrsim R_{\rm r}$. As in the case of $\alpha > 7/5$, these conditions are not satisfied when a reasonable range of parameters are employed. For example, when $\alpha = 1.0$ is employed, these conditions can be written as $25 r_{\rm kpc}^{-1} T_{\rm keV}^{-3/2} \mathcal{M}_2^{-3} L_{45} \gtrsim \rho_{0.1} \gtrsim 72 r_{\rm kpc}^{-1} T_{\rm keV} \mathcal{M}_2$. It can be seen that quite large external density is required.

Next, let us consider the sources with size smaller than kpc. Although relatively little is known about the ambient density profile in these scale, roughly constant density is expected from the β-model. Therefore, we set $\alpha = 0$. The expansion of the source is given by

$$R(t) \approx 1.7 \times 10^{-1} \rho_{0.1}^{1/5} L_{45}^{1/5} t_4^{3/5} \ {\rm kpc}, \tag{5.22}$$

where $t_4 = t/10^4 {\rm yr}$. In this case $R_{\mathcal{M}}$ and $R_{\rm r}$ are given by $R_{\mathcal{M}} \approx 4.8 \, {\rm kpc} \, \rho_{0.1}^{-1/2} L_{45}^{1/2} T_{\rm keV}^{-3/4} M_2^{-3/2}$ and $R_{\rm r} \approx 1.68 \times 10 \, {\rm kpc} \, \rho_{0.1}^{-6/7} L_{45}^{1/7}$, respectively. Since we are considering the case of flat density profile, from Eq. (5.5), radiative cooling becomes important when $R > R_{\rm r}$. Hence, the conditions for the shell to have radiative regime when the source size is $R < 1 {\rm kpc}$ is given by $R_{\rm r} < 1 {\rm kpc}$ and $R_{\rm r} < R_{\mathcal{M}}$ which are expressed as

$$\rho_{0.1} \gtrsim 2.7 \times 10 \ L_{45}^{1/6} \qquad \rho_{0.1} \gtrsim 3.5 \times 10^2 \ L_{45}^{-1} T_{\rm keV}^{7/2} \mathcal{M}_2^7. \tag{5.23}$$

Under assumption of $T_{\rm a} = 1 {\rm keV}$, and $\mathcal{M}_* = 2$, the range of $L_{\rm j}$ and ρ_0 which satisfy the above condition is illustrated in Fig. 5.4. As in the case of large scale source, quite large jet power and ambient density are required to satisfy Eq. (5.23).

This result is also not the consequence of the choice $\alpha = 0$. For example, if we increase the α to 0.5, the condition for $R_{\rm r} < 1 {\rm kpc}$ and $R_{\rm r} < R_{\mathcal{M}}$ is given by $\rho_{0.1} \gtrsim 5.0 \times 10 r_{\rm kpc}^{-1/2} L_{45}^{2/5}$ and $\rho_{0.1} \gtrsim 1.49 \times 10^2 r_{\rm kpc}^{1/2} L_{45}^{1/2} T_{\rm keV}^{9/4} \mathcal{M}_2^{9/2}$, respectively. It can be confirmed that these conditions are also unlikely to be satisfied. Hence, the shells of small scale sources are also likely to be adiabatic. Thus, we conclude that dynamical feedback from thermal radiation can be ignored in the shell associated with the radio sources of any scale. We can also justify the usage of adiabatic shock jump condition (§2.2.4) in the present model.

5.3.2 Quantitative estimation of the synchrotron emission

Here we quantitatively evaluate the synchrotron emissions from the shells associated with radio sources by applying the model described in §5.2.2. Since the size R is the direct observable quantity, hereafter we express the emission spectrum as a function of the size R instead of the age t merely for convenience. Since the shocks driven into the ambient medium is non-relativistic, we assume $p = 2$ from now on. As a fiducial case, we set the power-law index of

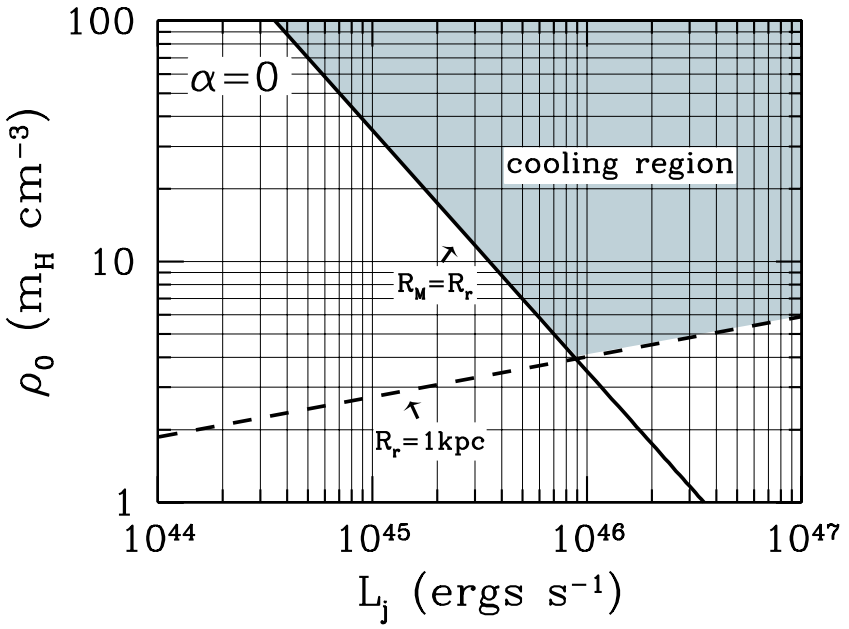

Figure 5.4: The ranges of $L_{\rm j}$ and ρ_0 which satisfy Eq. (5.23) in the case of $\alpha = 0$. Here $T_{\rm a} = 1{\rm keV}$, and $\mathcal{M}_* = 2$ are assumed. The solid line represents $R_{\rm r} = R_{\mathcal{M}}$. The dashed line represents $R_{\rm r} = 1{\rm kpc}$, respectively. The regions above the solid and the dashed line correspond to region of $R_{\rm r} < R_{\mathcal{M}}$ and $R_{\rm r} < 1{\rm kpc}$, respectively The shaded region shows the ranges of $L_{\rm j}$ and ρ_0 where $R_{\rm r} < 1{\rm kpc}$ and $R_{\rm r} < R_{\mathcal{M}}$ are satisfied.

the ambient density profile as $\alpha = 1.5$, since the variance of index from 1.5 does not change the essential features discussed in this study. Hence, the relation between R and t is given by Eq. (5.20).

Based on observational and theoretical estimates (e.g., Moss & Shukurov 1996; Vikhlinin et al. 2001; Carilli & Taylor 2002; Schekochihin et al. 2005), the magnetic field strengths in elliptical galaxies and clusters of galaxies are typically in the vicinity of few μG. In the following discussion we choose $B = 10\mu{\rm G}$ as a fiducial value since the magnetic field in the postshock region increase by a factor between 1 and 4 from that of the ambient medium (depending on the obliquity of the shock against the field line). The parameters ϵ_e and ξ, which characterize the electron acceleration process, are treated as a free parameters.

As mentioned in §5.2.2, we treat $\ln(\gamma_{\rm max})$ which appears in Eq. (5.17) as a constant. From Eq. (5.11), the maximum Lorentz factor $\gamma_{\rm max}$ is given as: for $R < R_{\rm br}$, $\gamma_{\rm max} \approx 8.7 \times 10^{10}\, \xi^{-1} B_{-5} r_{\rm kpc}^{-1/2} \rho_{0.1}^{-1/3} L_{45}^{1/3} R_5^{5/6}$; for $R_{\rm br} < R$, $\gamma_{\rm max} \approx 1.1{\times}10^{8}\, \xi^{-1/2} B_{-5}^{-1/2} r_{\rm kpc}^{-1/2} \rho_{0.1}^{-1/3} L_{45}^{1/3} R_5^{-1/3}$, where $B_{-5} = B/10\mu{\rm G}$, $R_5 = R/5{\rm kpc}$ and $R_{\rm br} = R(t_{\rm br})$. Hence, we approximate as

$\ln(\gamma_{\rm max}) \sim 20$. As a result, we obtain

$$\begin{aligned} L_{\rm peak} &\approx 2.4\times10^{42}\epsilon_e L_{45}\ {\rm ergs\ s^{-1}}, \\ \nu_{\rm br} &\approx 2.3\times10^{11}B_{-5}^{-3}r_{\rm kpc}^{-1}\rho_{0.1}^{-2/3}L_{45}^{2/3}R_5^{-7/3}\ {\rm Hz}, \\ \nu_{\rm max} &\approx \begin{cases} 9.3\times10^{22}\xi^{-2}B_{-5}^{3}r_{\rm kpc}^{-1}\rho_{0.1}^{-2/3}L_{45}^{2/3}R_5^{5/3}\ {\rm Hz} & {\rm for}\ R<R_{\rm br}, \\ 1.5\times10^{17}\xi^{-1}r_{\rm kpc}^{-1}\rho_{0.1}^{-2/3}L_{45}^{2/3}R_5^{-1/3}\ {\rm Hz} & {\rm for}\ R_{\rm br}<R, \end{cases} \end{aligned} \tag{5.24}$$

Depending on its size, the spectrum of synchrotron emission is determined by substituting the above quantities in either Eq. (5.15) ($R < R_{\rm br}$) or Eq. (5.16) ($R_{\rm br} < R$). The source size at the transition time $R_{\rm br}$ is given by

$$R_{\rm br} \approx 6.3\xi^{1/2}B_{-5}^{-3/2}{\rm pc}.$$

Hence, transition occurs in the early stage of the evolution when their overall size is quite compact ($2R < 1{\rm kpc}$). In Fig. 5.5, we display the resultant spectrum for radio sources with size of $2R = 10{\rm kpc}$. In the figure, νL_ν is evaluated from the fiducial values given in Eqs. (5.24). Wide range of parameter space is employed for ϵ_e, and each displayed line represents the spectrum for the corresponding values of ϵ_e. The spectrum is brightest ($\nu L_\nu = L_{\rm peak}$) in the frequencies ranging from radio band ($\nu_{\rm br} \sim 10^{11}{\rm Hz}$) up to soft X-ray band ($\nu_{\rm max} \sim 10^{17}{\rm Hz}$) for the given fiducial parameters. It should be noted that the spectrum at low frequency range is quite sensitive to the size due to the strong dependence of the break frequency on R ($\nu_{\rm br} \propto R^{-7/3}$). On the other hand, as long as $R_{\rm br} < R$ is satisfied, the spectrum at high frequency range quite insensitive to the age since the maximum frequency depends weakly on it ($\nu_{\rm max} \propto R^{-1/3}$). As noted in §5.3.2, magnitude of $L_{\rm peak}$ is solely determined by the acceleration efficiency ϵ_e and the jet kinetic power $L_{\rm j}$ ($L_{\rm peak} \propto \epsilon_e L_{\rm j}$). Higher values of ϵ_e and $L_{\rm j}$ are favored for detection since they lead to brighter luminosity.

To investigate the observational significance of the emission, surface brightness must be considered since radio sources extend in large scales ($\sim {\rm kpc} - {\rm Mpc}$). The evolution of surface brightness at $r = R - \delta R$, which corresponds to the brightest feature (see Fig. 5.2), is given by

$$\begin{aligned} \nu\Sigma_{\nu,{\rm CD}} &= \Sigma_{\rm peak}\left(\frac{\nu}{\nu_{\rm br}}\right)^{1/2} \quad (\nu<\nu_{\rm max}) && {\rm for}\ R<R_{\rm br}, \\ \nu\Sigma_{\nu,{\rm CD}} &= \begin{cases} \Sigma_{\rm peak}\left(\frac{\nu}{\nu_{\rm br}}\right)^{1/2} & (\nu<\nu_{\rm br}) \\ \Sigma_{\rm peak} & (\nu_{\rm br}<\nu<\nu_{\rm max}) \end{cases} && {\rm for}\ R_{\rm br}<R, \end{aligned} \tag{5.25}$$

where

$$\Sigma_{\rm peak} \approx 1.0\times10^{-14}\epsilon_{\rm e}L_{45}R_5^{-2}\ {\rm ergs\ s^{-1}cm^{-2}arcsec^{-2}}.$$

Note that there are no significant difference in the brightness from the above values at the inner region ($r < R - \delta R$). For instance, the lowest brightness at the center of the source $\Sigma_{\nu,0}$ is

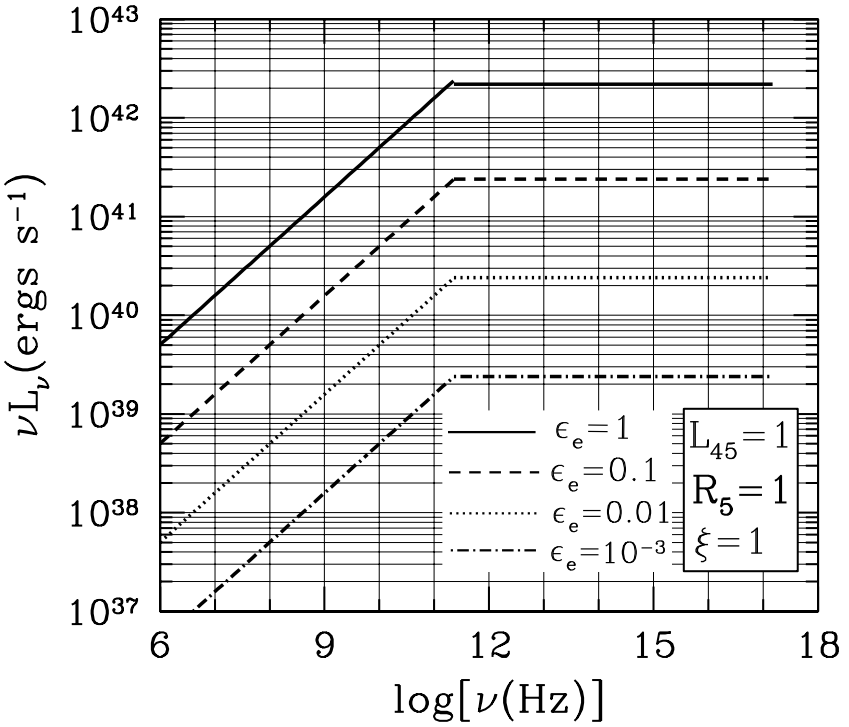

Figure 5.5: The synchrotron spectrum for the source with $L_{\rm j} = 10^{45}{\rm ergs\,s^{-1}}$ and $2R = 10{\rm kpc}$. Spectrum for various ϵ_e is displayed. Here $\alpha = 1.5$, $\rho_0 = 0.1 m_{\rm H}{\rm cm}^{-3}$, $r_0 = 1{\rm kpc}$, $\xi = 1$,and $B = 10\mu{\rm G}$ are assumed.

differs only by a constant factor of $(2R/\delta R - 1)^{-1/2} \sim 0.3$ at an arbitrary frequency. As is obvious, higher values of ϵ_e and $L_{\rm j}$ lead to higher surface brightness since the luminosity is proportional to $\epsilon_e L_{\rm j}$. Smaller (younger) sources have higher surface brightness due to there smaller solid angle as mentioned in §5.2.2. In Fig. 5.6, we display $\nu\Sigma_{\nu,{\rm CD}}$ for different acceleration efficiency $\epsilon_{\rm e}$ (i.e., 10^{-3}, 0.01, 0.1, and 1) and size R (i.e., $0.5{\rm kpc}$, $5{\rm kpc}$, $50{\rm kpc}$, and $500{\rm kpc}$).

5.3.3 Synchrotron emission as a probe of electron acceleration

The predicted spectrum extends in broad band. Since the spectrum depends crucially on the parameters ϵ_e and ξ, observations of the emissions provide us a opportunity to quantify the key parameters which provide an important information on the physics of electron acceleration at non-relativistic shocks. Here we show how we can evaluate ϵ_e and ξ from the observed emission.

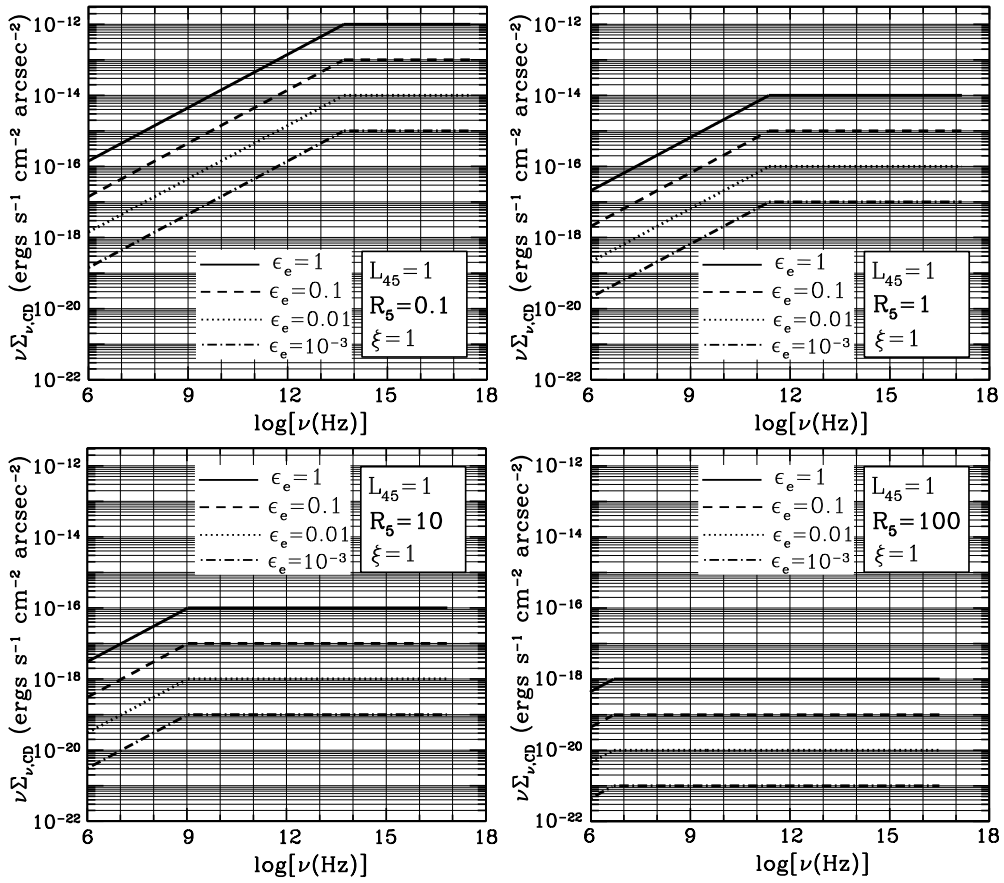

Figure 5.6: Surface brightness of the shell at $r = R - \delta R$ with different size R (0.5kpc, 5kpc, 50kpc, and 500kpc). Here $L_{\rm j} = 10^{45}{\rm ergs\,s^{-1}}$, $B = 10\mu$G, $\alpha = 1.5$, $\rho_0 = 0.1 m_{\rm H}{\rm cm^{-3}}$, $r_0 = 1$kpc, $\xi = 1$ are assumed.

When the emission from the shell is observed and confirmed as a synchrotron origin, comparison of the detected surface brightness with Eq. (5.25) gives a direct constraint on ϵ_e. For instance, let us consider a shell with observed surface brightness of $\Sigma_{\nu,\rm obs}$ and size of $R_{\rm obs}$. Depending on whether the observed frequency $\nu_{\rm obs}$ is above the break frequency $\nu_{\rm br}$ or not, from Eq. (5.25), the evaluation ϵ_e from the observables is classified into to two cases as

$$\epsilon_e \approx \begin{cases} \left(\frac{\nu_{\rm obs}\Sigma_{\nu,\rm obs}}{1.0\times10^{-14}{\rm ergs\ s^{-1}cm^{-2}arcsec^{-2}}}\right)\left(\frac{\nu_{\rm obs}}{2.3\times10^{11}{\rm Hz}}\right)^{-1/2}\left(\frac{R_{\rm obs}}{5{\rm kpc}}\right)^{5/6} r_{\rm kpc}^{-1/2}\rho_{0.1}^{-1/3}B_{-5}^{-3/2}L_{45}^{-2/3} & \text{for } \nu_{\rm obs} < \nu_{\rm br}, \\ \left(\frac{\nu_{\rm obs}\Sigma_{\nu,\rm obs}}{1.0\times10^{-14}{\rm ergs\ s^{-1}cm^{-2}arcsec^{-2}}}\right)\left(\frac{R_{\rm obs}}{5{\rm kpc}}\right)^{2} L_{45}^{-1} & \text{for } \nu_{\rm br} < \nu_{\rm obs}. \end{cases} \tag{5.26}$$

Even in the case when $\nu_{\rm br}$ is unknown, the observational diagnostic for which equation in Eq. (5.26) to be used can be obtained from the form of the spectrum. In the case when the observed emission show a flat spectrum ($\nu\Sigma_\nu \propto \nu^0$), the below equation is applicable. On the other hand, the above equation is applicable if the spectrum is observed as a form of power-law of the frequency with spectral index near $1/2$ ($\nu\Sigma \propto \nu^{1/2}$). While an independent estimate of jet kinetic power ($L_{\rm j}$) is required for the evaluation of ϵ_e in the case of $\nu_{\rm br} < \nu_{\rm obs}$, also the magnetic field strength and the ambient density profile (B, r_0, and ρ_0) need to be specified in addition for $\nu_{\rm obs} < \nu_{\rm br}$. Therefore, observation at the frequency above the break frequency is favored for the evaluation of ϵ_e since only one parameter needs to be determined.

In a similar way, constraint on ξ is also obtained by the detection of the shell. If the measurement of maximum cut-off frequency in the spectrum is possible by multiwavelength observation, ξ can be constrained from Eq. (5.24). Depending on whether the form of the spectrum is given by single power-law ($R_{\rm obs} < R_{\rm br}$) is or broken power-law ($R_{\rm obs} < R_{\rm br}$), the evaluation of ξ from the observables is classified into to two cases as Depending on the size of the system, evaluation of ξ is classified into two cases as

$$\xi \approx \begin{cases} \left(\frac{\nu_{\rm max,obs}}{9.3\times10^{22}{\rm Hz}}\right)^{-1/2} \left(\frac{R_{\rm obs}}{5{\rm kpc}}\right)^{5/6} B_5^{3/2} r_{\rm kpc}^{-1/2} \rho_{0.1}^{-1/3} L_{45}^{1/3} & \text{for } R_{\rm obs} < R_{\rm br}, \\ \left(\frac{\nu_{\rm max,obs}}{1.5\times10^{17}{\rm Hz}}\right)^{-1} \left(\frac{R_{\rm obs}}{5{\rm kpc}}\right)^{-1/3} r_{\rm kpc}^{-1} \rho_{0.1}^{-2/3} L_{45}^{2/3} & \text{for } R_{\rm br} < R_{\rm obs}, \end{cases} \tag{5.27}$$

where $\nu_{\rm max,obs}$ is the maximum cut-off frequency measured from observation. Note that, even in the case when the maximum frequency is not measured, the detection of the shell at an arbitrary frequency gives at least an upper limit on ξ, since the observed frequency must satisfy $\nu_{\rm obs} < \nu_{\rm max}$. The value of the upper limit can be obtained from the right hand side of Eq. (5.27) by simply substituting the observed frequency $\nu_{\rm obs}$ in $\nu_{\rm max,obs}$. As in the above discussion on the evaluation of ϵ_e, the criterion for determining which equation in Eq. (5.27) is applicable can be obtained from the observed spectral index. When the observed spectrum below $\nu_{\rm max,obs}$ is flat ($\nu\Sigma_\nu \propto \nu^0$ for $\nu < \nu_{\rm max,obs}$), the below equation is applicable, since this implies that the spectrum is given by a broken power-law ($R_{\rm br} < R_{\rm obs}$). On the other hand, if the spectral index is estimated to be $1/2$ ($\nu\Sigma_\nu \propto \nu^{1/2}$ for $\nu < \nu_{\rm max,obs}$), then the above equation is applicable. In both cases, the jet kinetic power ($L_{\rm j}$) and ambient density profile ($\rm r_0$ and ρ_0) need to be determined for evaluation of ξ. Since magnetic field strength need to be specified in addition in the case of $R_{\rm obs} < R_{\rm br}$, the case of $R_{\rm br} < R_{\rm obs}$ is relatively useful for the estimation of ξ.

Next we discuss the detectability of the shell in various frequencies and investigate how the observations at each frequency range can serve as probe of ϵ_e and ξ. To sum up in advance, among all frequencies, we expect observation in optical/UV band is suited for the detection of synchrotron emission from the shell since radio emissions within the radio lobe and the thermal X-ray emissions from ambient ISM/ICM and thermal electrons within the shell becomes hampers the detection at the lower (radio) and higher (X-ray) frequencies. Moreover, for given

values of ϵ_e and $L_{\rm j}$, compact (young) radio sources ($2R \lesssim 10{\rm kpc}$) are favored rather than the extended (old) radio sources due to their higher surface brightness.

Radio

From Fig. 5.5, it can be seen that shells have potential to be observed in radio frequency. On the other hand, however, while radio observations revealed large number of radio lobes which corresponds to the emission within the cocoon, radio emissions from shell have not been reported so far (Carilli et al. 1988). There are two possibilities for the consequence. One is simply that the acceleration efficiency ϵ_e is too low and the emission is below the detection threshold. Second is that, although ϵ_e is high enough for detection, ξ is too large and the emission spectrum does not extend to radio frequency (or possibly both). Considering the constraints on ξ and ϵ_e. an upper limit on ϵ_e can be obtained in the first case, while or lower limit on ξ is obtained in the second case. However, we consider that the second possibility is quite unlikely since the condition requires extremely large value for ξ ($\gtrsim 10^7$) in contrast to the other astrophysical shocks. For example, recent studies (e.g., Yamazaki et al. 2004; Stage et al. 2006; Tanaka et al. 2008), suggest that the shocks associated with SNRs are in nearly Bohm limit ($1 \lesssim \xi \lesssim 10$), while in the case of the shocks in the heliosphere, reported values are $10 \lesssim \xi \lesssim 100$ (e.g., Shimada et al. 1999). Hence, we focus on the first case in the following.

Let us consider the condition on ϵ_e for the shell associated with radio sources to be observed at radio frequency. A typical noise in the spatially resolved radio observations of powerful radio galaxies ($2R \sim 100{\rm kpc} - 1{\rm Mpc}$) observed by VLA, for example, is $\sim 30\mu{\rm Jy/beam}$ with beam width of $0.23{\rm arcsec}$ at $\nu \sim 8.4{\rm GHz}$ (Hardcastle et al. 1997). By employing the above value to determine the detection threshold, 3σ detection limit is given by $[\nu\Sigma_\nu] \sim 1.8 \times 10^{-16}\ {\rm erg\ s^{-1}cm^{-2}arcsec^{-2}}$. Hence, from Eq. (5.26) the condition for the emission to be above the detection limit is given by

$$\epsilon_e \gtrsim \begin{cases} 9.4 \times 10^{-2} R_5^{5/6} r_{\rm kpc}^{-1/2} \rho_{0.1}^{-1/3} B_{-5}^{-3/2} L_{45}^{-2/3} & \text{for } R < R_*, \\ 1.8 \times 10^{-2} R_5^2 L_{45}^{-1} & \text{for } R_* < R, \end{cases} \tag{5.28}$$

where $R_* \sim 20 B_{-5}^{-9/7} r_{\rm kpc}^{-3/7} \rho_{0.1}^{-2/7} L_{45}^{2/7} {\rm kpc}$ is the source size at the time when the break frequency becomes equal to $8.4{\rm GHz}$. From the above equation, it can be seen that, for typical observed sizes of radio galaxies $2R \sim 100{\rm kpc} - {\rm Mpc}$, only very powerful source with jet with kinetic power kinetic power of $L_{\rm j} \gtrsim 10^{45}{\rm erg\ s^{-1}}$ can give constraint on ϵ_e,r since emission cannot be detected even in the case of maximum acceleration efficiency ($\epsilon_e = 1$) for $L_{\rm j} \lesssim 10^{45}{\rm erg\ s^{-1}}$. For example, in the case of most powerful source with kinetic power of $L_{\rm j} \sim 10^{47}{\rm ergss^{-1}}$ (see §3), the allowed range for detection is $\epsilon_e \gtrsim 3.0 \times 10^{-2}$. Hence, the lack of prominent emission from the shell in these sources requires lower value for ϵ_e. Much lower values of ϵ_e are allowed for detection when the source size are compact, since the surface

brightness is higher for a given value of $L_{\rm j}$ as mentioned in §5.3.2. Therefore, observation of compact radio sources may be more useful for giving constraint on ϵ_e than the larger sources.

Although we employed a certain value evaluated from the data given in Hardcastle et al. (1997) as the detection threshold in the above discussion, note that it can vary largely among individual sources since the noise in the radio observation is induced by the brighter emissions originated within the radio lobes. Hence, one need to bear in mind that for radio sources with a higher surface brightness leads to a larger noise in the radio image. This is particularly relevant for the discussion on compact sources since much higher surface brightness is observed in compact radio sources namely GHz peaked spectrum (GPS) and Compact steep spectrum (CSS) sources ($2R \lesssim 20{\rm kpc}$) than that of the larger radio galaxies (O'Dea & Baum 1997). Hence, although the surface brightness of the shell is expected to be higher for smaller sources, the detection limit is likely to increase for compact radio sources. Therefore, observation of shell in radio observation have difficulty in that the detection is inevitably hampered by the emission from the coexisting radio lobes.

IR/Optical/UV

In contrast with radio, observations at higher frequencies, from infrared (IR) to ultraviolet (UV) band ($\sim 10^{12} - 10^{16}{\rm Hz}$), are expected to be better indicter of synchrotron emission from shell. There are two advantages for the detection. One is simply that the luminosity tends to be larger, since the emissions at higher frequencies reach the peak luminosity $L_{\rm peak}$ in the earlier stage of the evolution (see Fig. 5.6). Second is that their are no bright prominent emission within the lobe in these frequencies which may hamper the detection of the shell unlike in radio. Hence, observations of shell at these frequencies can be useful for probing ϵ_e. Also it is expected that an important constraint on ξ, at least an upper limit, can be obtained.

At these frequencies, detectors such as Subaru Telescope is expected to be useful due to its high sensitivity. For example, detection limit of Subaru prime-focus camera (Supreme-Cam) on the Subaru Telescope at $\nu \sim 4\times10^{14}{\rm Hz}$ is given by $\nu\Sigma_\nu \sim 3\times10^{-16}{\rm ergs\ s^{-1}cm^{-2}arcsec^{-2}}$. For the detection, surface brightness must exceed the detection threshold, and also the maximum frequency must be above the observed frequency ($\nu_{\rm max} \gtrsim 4 \times 10^{14}{\rm Hz}$). From Eqs. (5.26) and (5.27), these two conditions gives a lower limit and upper limit on ϵ_e and ξ, respectively, for the shell to be observed. Focusing on the extended sources with size larger than R_{**}, where $R_{**} \sim 0.2B_{-5}^{-9/7}r_{\rm kpc}^{-3/7}\rho_{0.1}^{-2/7}L_{45}^{2/7}{\rm kpc}$ is the source size at the time when the break frequency becomes equal to the observed frequency ($\nu_{\rm br} \sim 4 \times 10^{14}{\rm Hz}$), these limits are given by

$$\begin{aligned} \epsilon_e &\gtrsim 3.0 \times 10^{-2} L_{45}^{-1} R_5^2, \\ \xi &\lesssim 3.8 \times 10^2 R_5^{-1/3} r_{\rm kpc}^{-1} \rho_{0.1}^{-2/3} L_{45}^{2/3}. \end{aligned} \quad \text{for } R_{**} < R \tag{5.29}$$

As is common at all frequencies, smaller sources with larger kinetic power are favored for

constraining ϵ_e and ξ, since it allow lower value for ϵ_e and higher value for ξ for detection. From the above equation, it can be seen that ξ is likely to be above the lower limit, if its value is in the ranges observed in other astrophysical object such as in SNRs and heliosphere ($1 \lesssim \xi \lesssim 10^2$). Hence, observations at this frequency gives an important information on whether the shocks driven by AGN jets can accelerate the electrons efficiently as in the other astrophysical shocks or not. Considering the condition on ϵ_e, while there is only slight difference in the lower limit for detection from that of the radio observation given previously in the case of large extended source, much lower values are allowed at this frequency in the case of compact sources ($R < R_*$). This is simply because the surface brightness at this frequency is higher for $R < R_*$, while there are no difference for $R_* < R$ (see Fig. 5.6). For example, in the case of powerful source with jet kinetic power of $L_{\rm j} \sim 10^{47}{\rm ergs\,s^{-1}}$ and size of $2R \sim 1{\rm kpc}$, ϵ_e can be as low as $\sim 3 \times 10^{-6}$ for detection at $\nu \sim 4 \times 10^{14}{\rm Hz}$ whereas ~ 200 times larger value is required at $\nu \sim 8.4{\rm GHz}$. for given set of fiducial parameters. Therefore, it is suggested that observations of compact sources (i.e., GPS/CSS sources) at this frequency are suited for giving constraints on ϵ_e as well as ξ.

Although the sensitivity is relatively poor compared with that of Subaru, Hubble Space Telescope (HST) is useful for detecting small source since it have higher spatial resolution. Interestingly, recent observation by HST reveals a extended emission source in near UV band with luminosity in the range of $\sim 10^{40} - 10^{42}{\rm ergs\,s^{-1}}$ which are associated with several GPS/CSS sources (Labiano et al. 2008) with some of the them (1443+77, 1814-637, and 2352+495) showing similar size in radio and UV image. While Labiano et al. (2008) argued that these emissions are due to burst of star formation, it is worth noting that the emission can be attributed to the emission from the shell. In Fig. 5.7, we display the spectra for a given set of R, $L_{\rm j}$, and ϵ_e which reproduce the observed luminosities and linear sizes of 1443+77 ($2R = 8.1{\rm kpc}$), 1814-637 ($2R = 0.5{\rm kpc}$), and 2352+495 ($2R = 0.9{\rm kpc}$). If the observed emissions are indeed synchrotron emissions from the shell, in the case of $L_{\rm j} \sim 10^{45}{\rm ergss^{-1}}$, the values of ϵ_e and ξ are constrained as $\epsilon_e \sim 0.75$ and $\xi \lesssim 180$ for 1443+77, $\epsilon_e \sim 1$ and $\xi \lesssim 380$ for 1814-637, and $\epsilon_e \sim 0.04$ and $\xi \lesssim 370$ for 2352+495. However, for firm constraint, independent estimate of $L_{\rm j}$ is important since the required values of ϵ_e and ξ vary sensitively with the $L_{\rm j}$ as is shown. For higher $L_{\rm j}$, lower value of ϵ_e and higher upper limit of ξ are obtained .

X-ray

Since the maximum cut-off frequency $\nu_{\rm max}$ increases until the source size reaches $R_{\rm br}$ and decreases thereafter, the attainable maximum frequency throughout the evolution is evaluated by $\nu_{\rm max}$ at the time when is $R = R_{\rm br}$. From Eq. (5.24), the frequency is given by $\nu \sim 1.3 \times 10^{18} \xi^{-7/6} B_5^{1/2} r_{\rm kpc}^{-1} \rho_{0.1}^{-1} L_{45}^{2/3}{\rm Hz}$. Hence, at least for radio sources with kinetic power of $L_{\rm j} \gtrsim 10^{44}{\rm ergs\,s^{-1}}$, since the spectrum with peak luminosity can extend up to $\nu_{\rm max} \sim$

$10^{17} - 10^{18}$Hz, detections of shell at X-ray frequency can also be used for probing the electron acceleration. While the parameter ϵ_e can also be constrained as in the case of lower frequencies, the observation at this band is particularly intriguing in the respect of constraining ξ, since the measurement of maximum frequency $\nu_{\rm max}$ can be used as diagnostics of Bohm diffusion ($\xi \sim 1$). From Eq. (5.27), the detection of synchrotron X-ray emission implies that the magnetic fluctuation by the accelerated particles are efficient and nearly Bohm diffusion limit ($1 \lesssim \xi \lesssim 10$), is realized as in the case of shocks associated with SNRs. On the other hand, in the case of non-detection, it is either ξ is large or $\epsilon_e L_{\rm j}$ is too small to emit a observable signature. To break the degeneracy, observation at lower frequencies is important.

It should be noted, however, that the detection at this band has difficulty since the contamination from ambient gas since the radio sources generally reside in X-ray emitting ISM/ICM with typical temperature of $\sim {\rm keV}$. Also theoretical studies (Heinz et al. 1998; Reynolds et al. 2001; Zanni et al. 2003) predict that enhanced X-ray emission originate from the shock heated thermal electrons within the shell which in turn may overwhelm the non-thermal emissions. Although the numbers are few, the thermal X-ray emission from the shocked shell has been confirmed in recent X-ray observations (Croston et al. 2007; Kraft et al. 2007). Therefore, the distinction between the non-thermal component from that of the thermal component is required for the study of electron acceleration.

Centaurus A is the first and the best example of radio galaxy which have been extensively studied on the X-ray emission within the shocked shell (Kraft et al. 2003; Kraft et al. 2007). Since the high quality data reveal clear evidence of strong shock this source is also an ideal candidate for the particle acceleration. However, one needs to bear in mind that Centaurus A is classified as "weak" (FRI) radio source, and hence low kinetic power, much below the employed fiducial value ($L_{\rm j} < 10^{45}{\rm ergss}^{-1}$), is expected (e.g., Allen et al. 2006; Bîrzan et al. 2008) which in turn makes the observations of synchrotron emission difficult. A rough estimation of the kinetic power using $L_{\rm j} t \sim 4 P_{\rm c} V_{\rm c} \sim 4 P_{\rm s} V_{\rm c}$ gives a kinetic power of $L_{\rm j} \sim 3 \times 10^{41} {\rm ergs\ s}^{-1}$. In the above equation, we used the evaluated thermal pressure of the shell ($\sim 2 \times 10^{-10} {\rm dyne\ cm}^{-2}$) from the X-ray data together with the estimated size and age of the source ($R \sim 6{\rm kpc}$ and $t \sim 2 \times 10^6 {\rm yr}$). Hence, from Eq. (5.24), it is evident that the synchrotron emission cannot be observed in X-ray since the maximum frequency is evaluated as $\nu_{\rm max} \sim 1.6 \times 10^{15} \xi^{-1} {\rm Hz}$, where we used $r_0 \sim 6{\rm kpc}$ and $\rho \sim 1.7 \times 10^{-3} m_{\rm H} {\rm cm}^{-3}$ based on the X-ray data. Indeed, the observed X-ray spectrum of the shell is confirmed to be a thermal origin and non-thermal spectrum is absent. Note that detections at frequencies below $\nu_{\rm max}$ are also difficult due to its low power. Substituting the estimated values of $L_{\rm j}$ and R in Eqs. (5.28) and (5.29), the required value of ϵ_e for detection exceeds unity which is clearly unphysical. Therefore, we suggest that Centaurus A is not suited for constraining ϵ_e and ξ from the observations.

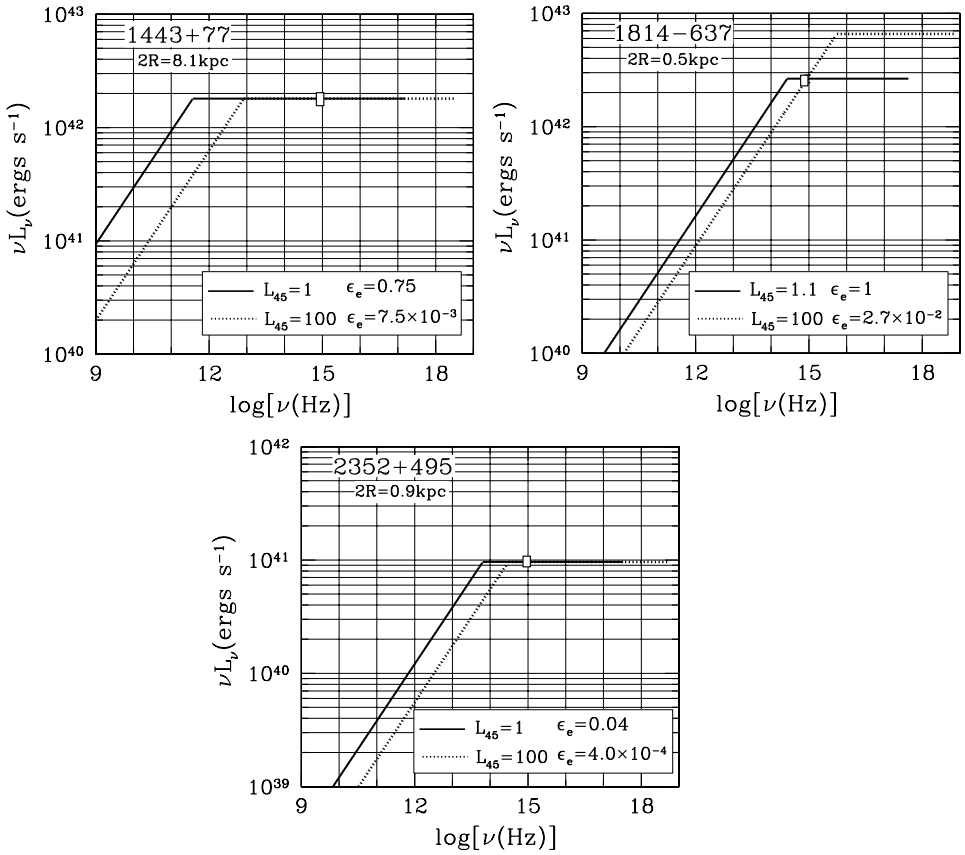

Figure 5.7: Spectrum of the shell with sizes of $2R = 8.1\mathrm{kpc}$ (upper left panel), $2R = 0.5\mathrm{kpc}$ (upper right panel), and $2R = 0.9\mathrm{kpc}$ (lower panel) which correspond to the linear size of 1443+77, 1814-637, and 2352+495, respectively. Together with the spectra, we display the observed luminosities (open square) of these sources at near UV-band (Labiano et al. 2008). Here $B = 10\mu\mathrm{G}$, $\alpha = 1.5$, $\rho_0 = 0.1 m_{\mathrm{H}} \mathrm{cm}^{-3}$, $r_0 = 1\mathrm{kpc}$, and $\xi = 1$ are assumed.

Chapter 6

CONCLUSIONS

Based on the large-scale dynamics of AGN jet, we investigated the physical properties of the jet and the emission properties of the cocoon and shell formed via interaction between the jet and the ambient gas. The dynamical expansion of cocoon inflated by powerful FRII jet was described by the analytical model which approximate the cocoon as rotational ellipsoid elongated in the direction of jet axis. On the other hand, by neglecting the elongation for simplicity, the evolution of the shell composed of shocked ambient gas which envelopes the cocoon was described by the analytical model of spherical expansion. In both cases, we solve all physical quantities in functions of the kinetic power of jet and source age. Based on these models we discovered following major results:

(I) Total kinetic powers in FRII jets

By a detail comparison of observed radio morphology of FRII sources with the analytical model of cocoon expansion, we evaluate the kinetic power of jets and age. We select four bright FRII radio sources (Cygnus A, 3C 223, 3C 284, and 3C 219), for which the mass-density profiles of ICM are known. As a result, it is found that large fractions $\gtrsim 0.02 - 0.7$ of the Eddington luminosity ($L_{\rm Edd}$) are carried away as a kinetic power of jet. The upper limit of estimated $2L_{\rm j}/L_{\rm Edd}$ are larger than unity ($\lesssim 10$). Since the quantity $2L_{\rm j}/L_{\rm Edd}$ directly gives the required minimum rate of mass accretion on to the SMBH normalized by the corresponding Eddington mass accretion rate, this results suggest the possibility of super-Eddington mass accretions. As a consequence of the large powers, we also find that the total energy stored in the cocoon ($E_{\rm c}$) largely exceeds the energy derived from the minimum energy condition for the energy of non-thermal electrons and magnetic fields ($E_{\rm min}$): $4 < E_{\rm c}/E_{\rm min} < 310$. Since it is reported that roughly equipartition between the non-thermal electrons and magnetic fields is realized in the radio lobes, this implies that most of the energy in cocoon is carried by invisible (unobserved) components such as thermal leptons (electron and positron) and/or protons.

(II) MeV γ-ray emission from cocoon

Based on the model of FRII radio sources, we evaluated the thermal evolution of the cocoon. Interestingly, we find that the temperatures of cocoon are governed only by the bulk Lorentz factor of the jet $\Gamma_{\rm j}$. The electron temperature T_e is typically predicted in the range of MeV for $\Gamma_{\rm j} \sim 10$. Constant temperatures of plasma in the cocoon can be realized because of the continuous energy injection by the jet with constant $\Gamma_{\rm j}$. As a result, we predict, for the first time, the bremsstrahlung emission peaked at MeV-γ band. Since larger number densities of thermal electrons are predicted for younger cocoons, brighter thermal bremsstrahlung emission than that of older cocoon is naturally expected.

Additionally, non-thermal IC emissions from young cocoons are also investigated. Importantly, in contrast to the case of MeV thermal emission, the typical frequency of SSC and IC/CMB emissions are predicted to be decreased for younger cocoon, since the maximum Lorentz factor of relativistic electrons are decreased. Therefore the typical frequencies of IC from a younger cocoon are at much lower than MeV ranges.

(III) Emissions from shell of shocked ambient medium

Based on the model which describes the dynamical evolution of the shell, we explored the properties of emissions from the shell. In this study, we considered two radiation processes: (i) bremsstrahlung emission from the thermal electrons and (ii) synchrotron emission from non-thermal electrons.

As for the thermal bremsstrahlung emission, we evaluate the effect of radiative cooling. Focusing on the early stage when expansion velocity has a high Mach number ($\mathcal{M} > 2$), we find that radiation effect can be ignored for a reasonable range of kinetic power of jet and mass density profile of ambient medium. Hence, the bow shocks associated with the radio sources expanding with high Mach number is expected to be adiabatic.

As for the synchrotron emission, we evaluate the evolution of the spectrum by assuming that constant fraction ϵ_e of internal energy in the shell is converted into that of non-thermal electrons with distribution function of form $N(\gamma_e) \propto \gamma_e^{-2}$. Taking into account of radiative cooling effects, we find that the evolution of the spectrum is classified into two stages. In the initial stage, synchrotron luminosity increases linearly with time in all frequencies and form of the spectrum is simply given by a power-law ($\nu L_\nu \propto \nu^{1/2} t$ for $\nu < \nu_{\rm max}$). In the late stage, increase in the luminosity ceases and remain constant above the break frequency ($\nu_{\rm br} \propto t^{-2}$) due to the effect of radiative cooling ($\nu L_\nu = L_{\rm peak} \propto \nu^0 t^0$ for $\nu_{\rm br} < \nu < \nu_{\rm max}$). The resultant spectrum is broad and can extend up to X-ray band ($\nu_{\rm max} \sim 10^{17} - 10^{18}$Hz) when Bohm limit ($\xi = 1$) is assumed. The plateau of peak luminosity which extends from $\nu_{\rm br}$ to $\nu_{\rm max}$ is solely determined by the jet kinetic power and the acceleration efficiency with linear dependence ($L_{\rm peak} \approx 2.4 \times 10^{42} \epsilon_e L_{\rm j}$).

Since the spectrum of the synchrotron emissions depends crucially of the parameters ξ and

ϵ_e which characterizes the acceleration efficiency, detection of the emission can be used as a probe for the physics of electron acceleration. Considering the detectability, smaller (younger) sources are favored for probing the electron acceleration, since the surface brightness decreases with the source size owning to the growth of the solid angle of the emission region ($\propto R^2$). Moreover, among all frequencies, observations at IR/optical/UV band are favored, since observation at lower (radio) and higher (X-ray) is likely to be hampered by the emissions from radio lobe and the thermal emissions from the ambient gas and co-existing thermal electrons within the shell, respectively. Based on the evaluated spectrum, the detectors such as Subaru Telescope and Hubble Space Telescope have enough sensitivity to be used for constraining the parameters ϵ_e and ξ through observations. Especially, observations of compact radio sources ($\lesssim 10\mathrm{kpc}$) are expected to give crucial constraints on these parameters. Although not confirmed, some of the extended near-UV emission associated with compact radio sources recently reported by Labiano et al. (2008) may be candidates for the synchrotron emission originated within the shell.

Although our models are based on simple assumptions and need more sophistication, these results have significant implications on the properties of relativistic jets and its large-scale evolution. Since our present study predicts photon sources in the universe which has not been reported so far, detail comparisons with future observations are expected to bring valuable informations.

Appendix A

The Minimum Energy Condition For Synchrotron Radiation

Synchrotron spectrum is a inseparable function of the magnetic field strength and the energy spectrum of the radiating electrons. Therefore, magnetic field strength and energy of electrons at the source cannot be obtained from the observed spectrum. To progress further it is usual to assume that the source is radiating such that its combined energy in particles and magnetic field is a minimum (e.g., Burbidge 1956). In this situation the energy in the magnetic field is $\sim 3/4$ of the energy in the particles, and so this is almost identical to the condition of equipartition. Here we review the derivation of minimum energy for electrons with power-law distribution.

First, we summarize the basic features of synchrotron radiation (e.g., Rybicki & Lightman 1979). The total power emitted by a single electron (or positron) with Lorentz factor γ_e is given by

$$P_{\rm syn} = 2\sigma_{\rm T} c \beta_e^2 U_{\rm B} \gamma_e^2 {\rm sin}^2\alpha. \tag{A.1}$$

where β_e and α are the speed of electrons in units of c and the pitch angle between the direction of motion and the magnetic field, respectively. When averaged over isotropic pitch angle,

$$P_{\rm syn} = \frac{4}{3}\sigma_{\rm T} c \beta_e^2 U_{\rm B} \gamma_e^2. \tag{A.2}$$

The spectrum from single electron is rather broad. The total emitted power per frequency is given by

$$P(\nu, \nu_{\rm c}) = \frac{3^{1/2} e^3 B {\rm sin}\alpha}{2\pi m_e c^2} F(\nu/\nu_{\rm c}). \tag{A.3}$$

Here $F(x)$ is a function defined as

$$F(x) \equiv x \int_x^\infty K_{5/3}(\zeta) d\zeta, \tag{A.4}$$

where $K_{5/3}$ is the modified Bessel function of order $5/3$. $\nu_{\rm c}$ is the critical frequency given as

$$\nu_{\rm c}(\gamma_e) = \frac{3}{2}\gamma_e^2 \nu_{\rm g} {\rm sin}\alpha \;\approx\; 4.199 \times 10^6 \gamma_e^2 B {\rm sin}\alpha \;\; {\rm Hz}. \tag{A.5}$$

where $\nu_{\rm g}$ is the non-relativistic gyration frequency of the electron which is given by $\nu_{\rm g} = eB/(2\pi m_e c)$. The peak frequency of the spectrum is given by

$$\nu_{\rm m}(\gamma_e) \simeq 0.29\nu_{\rm c}(\gamma_e) \approx 1.2177 \times 10^6 \gamma_e^2 B{\rm sin}\alpha \ {\rm Hz}. \tag{A.6}$$

When the number density of electrons with Lorentz factor between γ_e and $\gamma_e + d\gamma_e$ is given as $N(\gamma_e)d\gamma_e$, the emissivity per unit frequency is given by $J_\nu = \int P_{\nu,\nu_{\rm c}} N(\gamma_e) d\gamma_e$. For a power-law distribution of form

$$N(\gamma_e) = C\gamma_e^{-p}, \tag{A.7}$$

an analytical results can be found as

$$\begin{aligned} J_\nu &= \int_0^\infty P(\nu,\nu_{\rm c}) C\gamma_e^{-p} d\gamma_e \\ &= \frac{3^{1/2}e^3}{2\pi m_e c^2(p+1)} \left(\frac{2\pi m_e c}{3e}\right)^{-(p-1)/2} \Gamma\left(\frac{p}{4}+\frac{19}{12}\right)\Gamma\left(\frac{p}{4}-\frac{1}{12}\right) \\ &\quad (B{\rm sin}\alpha)^{(p+1)/2} C\nu^{-(p-1)/2}, \end{aligned} \tag{A.8}$$

where Γ is the Gamma function. In the above equation, we have used Eq. (A.3). Note that above equation is derived under the assumption of constant pitch angle, and therefore the emissivity depends strongly on α. For isotropic distribution, the probability for the particle to have pitch angle between α and $\alpha + d\alpha$ is given by $1/2{\rm sin}\alpha d\alpha$. By using the result

$$\frac{1}{2}\int_0^\pi ({\rm sin}\alpha)^{(p+3)/2} d\alpha = \frac{\pi^{1/2}\Gamma(\frac{p}{4}+\frac{5}{4})}{2\Gamma(\frac{p}{4}+\frac{7}{4})},$$

the emissivity for isotropic distribution is given by

$$\begin{aligned} J_\nu &= \frac{3^{1/2}e^3}{m_e c^2}\left(\frac{2\pi m_e c}{3e}\right)^{-(p-1)/2} a(p) B^{(p+1)/2} C\nu^{-(p-1)/2} \\ &\approx 2.344 \times 10^{-22} (8.397\times 10^6)^{(p-1)/2} a(p) \\ &\quad B^{(p+1)/2} C\nu^{-(p-1)/2} \ {\rm ergs\,s^{-1}\,cm^{-3}\,Hz^{-1}}, \end{aligned} \tag{A.9}$$

where $a(p)$ is the function of index p which is given by

$$a(p) = \frac{\pi^{1/2}}{2}\frac{\Gamma(\frac{p}{4}+\frac{19}{12})\Gamma(\frac{p}{4}-\frac{1}{12})\Gamma(\frac{p}{4}+\frac{5}{4})}{(p+1)\Gamma(\frac{p}{4}+\frac{7}{4})}.$$

Appropriate values of $a(p)$ are given in Table. A.1. Numerical integration are needed for more complicated electron distribution. From Eqs. (A.8) and (A.9), it can be seen that power-law radiation spectrum is obtained from electrons with power-law energy distribution. Usually

the symbol α is used to denote the spectral index ($J_\nu \propto \nu^{-\alpha}$), where α is related to particle distribution index p by

$$\alpha = \frac{p-1}{2}. \tag{A.10}$$

Table A.1: Values of constant $a(p)$

p	$a(p)$	p	$a(p)$	p	$a(p)$
1	2.056	2.5	0.359	4	0.186
1.5	0.909	3	0.269	4.5	0.167
2	0.529	3.5	0.217	5	0.157

Based on the above results, let us consider the minimum energy condition for synchrotron radiation. Suppose there is a source with a luminosity density (luminosity per unit frequency) $L_\nu \propto \nu^{-\alpha}$. When the distribution of the electrons are spatially uniform, the luminosity density is simply given by

$$L_\nu = J_\nu V = \mathcal{A}(\alpha) B^{1+\alpha} V C \nu^{-\alpha}, \tag{A.11}$$

where V is the volume of the source and $\mathcal{A}(\alpha)$ is a constant given by

$$\mathcal{A}(\alpha) = \frac{3^{1/2} e^3}{m_e c^2} \left(\frac{2\pi m_e c}{3e} \right)^{-\alpha} a(2\alpha + 1).$$

In the above equations, we have used Eqs. (A.9) and (A.10). The total energy present in the source is given by

$$E_{\rm tot} = (\eta U_e + U_B) V = \left(\eta \int_{\gamma_{\rm min}}^{\gamma_{\rm max}} \gamma_e m_e c^2 N(\gamma_e) d\gamma_e + \frac{B^2}{8\pi} \right) V, \tag{A.12}$$

where U_e and $U_{\rm B}$ denote the energy density of relativistic electrons and magnetic field which are responsible for the synchrotron radiation, respectively. Here η is the factor which takes into account of the energy density of particles such as protons and thermal electrons which do not contribute to the synchrotron radiation. Total energy given by Eq. (A.12) depend upon the unknown quantities C and B, but they are related through Eq. (A.11) for the observed luminosity of the source. From Eq. (A.6), here we define the typical frequency from electron with Lorentz factor γ_e as

$$\nu_e(\gamma_e) = 0.29 \frac{3}{2} \gamma_e^2 \nu_{\rm g} = 0.29 \frac{3e}{4\pi m_e c} \gamma_e^2 B = 1.2177 \times 10^6 \gamma_e^2 B = H \gamma_e^2 B. \tag{A.13}$$

From the above equation, the maximum and minimum frequencies of the synchrotron spectrum, $\nu_{\rm max}$ and $\nu_{\rm min}$, are related to the Lorentz factor as

$$\gamma_{\rm max} = \left(\frac{\nu_{\rm max}}{HB}\right)^{1/2} \qquad \gamma_{\rm min} = \left(\frac{\nu_{\rm min}}{HB}\right)^{1/2}. \tag{A.14}$$

Using $\nu_{\rm max}$ and $\nu_{\rm min}$, the total energy of particles in the source is expressed as

$$E_{\rm particle} = \eta V \int_{\gamma_{\rm min}}^{\gamma_{\rm max}} \gamma_e m_e c^2 C \gamma_e^{-p} d\gamma_e = \frac{\eta V C}{(p-2)} (HB)^{(p-2)/2} m_e c^2 [\nu_{\rm min}^{(2-p)/2} - \nu_{\rm max}^{(2-p)/2}].$$

From Eq (A.11), C can be expressed in terms of L_ν and B as

$$C = \frac{L_\nu}{\mathcal{A}(\alpha) B^{1+\alpha} V \nu^\alpha}.$$

Hence, $E_{\rm particle}$ can be expressed as

$$E_{\rm particle} = G(\alpha) \eta L_\nu B^{-3/2}, \tag{A.15}$$

where $G(\alpha)$ is a constant given by

$$\begin{aligned} G(\alpha) &= \frac{H^{(2\alpha-1)/2} m_e c^2}{(2\alpha-1)\mathcal{A}(\alpha)} [\nu_{\rm min}^{(1-2\alpha)/2} - \nu_{\rm max}^{(1-2\alpha)/2}] \nu^\alpha \\ . &= \frac{1}{(2\alpha-1)a(2\alpha+1)} [\nu_{\rm min}^{(1-2\alpha)/2} - \nu_{\rm max}^{(1-2\alpha)/2}] \nu^\alpha \left(\frac{4\pi m_e^5 c^9}{9e^7}\right)^{1/2} (0.29)^{(2\alpha-1)/2} 2^{-\alpha} \\ &= \frac{1}{(2\alpha-1)a(2\alpha+1)} [\nu_{\rm min}^{(1-2\alpha)/2} - \nu_{\rm max}^{(1-2\alpha)/2}] \nu^\alpha \\ &\quad \times 3.493 \times 10^{15} (1.2177 \times 10^6)^{(2\alpha-1)/2} (8.397 \times 10^6)^{-\alpha} \\ &= \frac{1}{(2\alpha-1)a(2\alpha+1)} [\nu_{\rm min}^{(1-2\alpha)/2} - \nu_{\rm max}^{(1-2\alpha)/2}] \nu^\alpha 3.165 \times 10^{12} (0.145)^\alpha. \end{aligned} \tag{A.16}$$

In the above equation, we have used Eqs. (A.9), (A.13), and (A.10). Thus, total energy is given by

$$E_{\rm tot} = G(\alpha) \eta L_\nu B^{-3/2} + V \frac{B^2}{8\pi} \tag{A.17}$$

Minimum energy can be found by minimizing Eq. (A.17) with respect to B. The magnetic field strength is given by

$$B_{\rm min} = \left[\frac{6\pi G(\alpha) \eta L_\nu}{V}\right]^{2/7}. \tag{A.18}$$

Note that $B_{\rm min}$ corresponds to approximate equality of the energy of particles and magnetic fields. From Eqs. (A.15) and (A.18), the total energy density of particles $U_{\rm particle} = \eta U_e$ is given by

$$U_{\rm particle} = \frac{G(\alpha)\eta L_\nu}{V} B^{-3/2} = \frac{1}{6\pi} B_{\rm min}^{7/2} B^{-3/2}.$$

When $B = B_{\rm min}$ we obtain

$$U_{\rm particle} = \frac{4}{3}\frac{B_{\rm min}^2}{8\pi} = \frac{4}{3} U_B. \tag{A.19}$$

From Eqs. (A.18) and (A.19), the minimum total energy is given by

$$E_{\rm min} = \frac{7}{3} U_B V = \frac{7}{24\pi} [6\pi G(\alpha)\eta L_\nu]^{4/7} V^{3/7}. \tag{A.20}$$

Thus, when L_ν, $\nu_{\rm max}$, and $\nu_{\rm min}$ are known, we can estimate the minimum energy and the minimum magnetic field strength from Eqs. (A.20) and (A.18) for a given value of η.

It is often cumbersome to calculate $G(\alpha)$. In the followings, we will show an example of a simplified calculation. Here we assume that the spectral index is given by $\alpha \approx 0.75$, and that the relation $\nu_{\rm max} \gg \nu_{\rm min}$ is satisfied. In this case, from Eq. (A.16), we can neglect $\nu_{\rm max}$ in comparison with $\nu_{\rm min}$ when calculating $G(\alpha)$. Then, if we evaluate the luminosity density L_ν at the frequency of $\nu = \nu_{\rm min}$/ the minimum energy is simply given as

$$E_{\rm min} \approx 8.0 \times 10^6 \eta^{4/7} V^{3/7} \nu^{2/7} L_\nu^{4/7} \ \ {\rm ergs}.$$

The minimum magnetic field strength is given as

$$B_{\rm min} \approx 9.3 \times 10^3 \left(\frac{\eta L_\nu}{V}\right)^{2/7} \nu^{1/7} \ \ {\rm G}.$$

References

Abramowicz, M. A., Czerny, B., Laosta, J. P., & Szuszkiewicz, E. 1988, ApJ, 332, 646

Achterberg, A., Gallant, Y. A., Kirk, J. G., & Guthmann, A. W. 2001, MNRAS, 328, 393

Alexander, P. 2002, MNRAS, 335, 610

Alexander, P., & Leahy, J. P. 1987, MNRAS, 225, 1

Allen, S. W., Dunn, R. J. H., Fabian, A. C., Taylor, G. B., & Reynolds, C. S. 2006, MNRAS, 372, 21

Aloy, M. A., Gomez, J. L., Ibanez, J. M., Marti, J. M., & Muller, E. 2000, ApJ, 528, 85

Antonucci, R. 1993, ARA&A, 31, 473

Bednarz, J., & Ostrowski, M. 1998, Phys. Rev. Lett., 80, 3911

Begelman, M. C. 1996, Cygnus A – Studay of a Radio Galaxy, 209

Begelman, M. C., Blandford, R. D., & Rees, M. J. 1984, Rev. Mod. Phys., 56, 255

Begelman, M. C., & Cioffi, D. F. 1989, ApJ, 345, 21

Bell, A. R. 1978, MNRAS, 182, 443

Bicknell, G. V. 1984, ApJ, 286, 68

Bicknell, G. V. 1994, ApJ, 422, 542

Bicknell, G. V. 1995, ApJS, 101, 29

Bicknell, G. V., Dopita, M. A., & O'Dea, C. P. 1997, ApJ, 485, 112

Birkinshaw, M. 1991, Beams and Jets in Astrophysics, 278

Bîrzan, L., McNamara, B. R., Nulsen, P. E. J., Carilli, C. L., & Wise, M. W. 2008, ApJ, 686, 859

Bîrzan, L., Rafferty, D. A., McNamara, B. R., Wise, M. W., & Nulsen, P. E. J. 2004, ApJ, 607, 800

Blandford, R. D., & Eichler, D. 1987, Phys. Rep., 154, 1

Blandford, R. D., Netzer, H., Woltjer, L., Courvoisier, T. J.-L., & Mayor, M. 1990, Active Galactic Nuclei,

Blandford, R. S., & Rees, M, J. 1974, MNRAS, 169, 395

Blundell, K. M., Rawlings, S., & Willott, C. J. 1999, AJ, 117, 677

Böhringer, H., Voges, W., Fabian, A. C., Edge, A. C., & Neumann, D. M. 1993, MNRAS, 264, 25

Boller, T., Brandt, W. N., & Fink, H. 1996, A&A, 305, 53

Bowman, M., Leahy, J. P., & Komissarov, S. S. 1996, MNRAS, 279, 899

Bridle, A. H., Hough, D. H., Lonsdale, C. J., Burns, J. O., & Laing, R. A. 1994, AJ, 108, 766

Bridle, A. H., & Perley, R. A. 1984, ARA&A, 22, 319

Burbidge, G. R. 1956, ApJ, 124, 416

Carilli, C. L., & Barthel, P. D. 1996, A&A Rev, 7, 1

Carilli, C. L., Perley, R. A., & Dreher, J. H. 1988, ApJ, 334, L73

Carilli, C. L., Perley, R. A., Dreher, J. W., & Leahy, J. P. 1991, ApJ, 383, 554

Carilli, C. L., & Taylor, G. B. 2002, ARA&A, 40, 319

Carvalho, J. C. 1985, MNRAS, 215, 463

Cavaliere, A., & Fusco-Femiano, R. 1978, A&A, 70, 677

Celotti, A., & Fabian, A. C. 1993, MNRAS, 264, 228

Celotti, A., & Fabian, A. C. 2004, MNRAS, 353, 523

Celotti, A., Ghisellini, G., & Chiaberge, M. 2001, MNRAS, 321, L1

Cioffi, D. F., & Blondin, J. M. 1992, ApJ, 392, 458

Clarke, D. A., Bridle, A. H., Burns, J. O., Perley, R. A., & Norman, M. L. 1992, ApJ, 385, 173

Collin, S., & Kawaguchi, T. 2004, A&A, 426, 797

Conway, J. E. 2002, New Astronomy Review, 46, 263

Cox, C. I., Gull, S. F., & Scheuer, P. A. G. 1991, MNRAS, 252, 558

Croston, J. H., Birkinshaw, M., Hardcastle., M. J., & Worrall, D. M. 2004, MNRAS, 353, 879

Croston, J. L., Hardcastle, M. H., Harris, D. E., Besole, E., Birkinshaw, M., & Worrall, D. M. 2005, ApJ, 626, 733

Croston, J. H., Kraft, R. P., & Hardcastle, M. J. 2007, ApJ, 660, 191

De Young, D. S. 1996, Energy Transport in Radio Galaxies and Quasars, 100, 261

de Young, D. S. 2002, The physics of extragalactic radio sources, by David S. De Young. Chicago, Ill. : University of Chicago Press, 2002.,

Di Matteo, T., Croft, R. A. C., Springel, V., & Hernquist, L. 2003, ApJ, 593, 56

Drury, L. O. 1983, Reports on Progress in Physics, 46, 973

Dunn, R. J. H., & Fabian, A. C. 2004, MNRAS, 355, 862

Fabian, A. C., Celotti, A., Blundell, K. M., Kassim, N. E., & Perley, R. A. 2002, MNRAS, 331, 369

Fabian, A. C., Sanders, J. S., Taylor, G. B., Allen, S. W., Crawford, C. S., Johnstone, R. M., & Iwasawa, K. 2006, MNRAS, 366, 417

Falle, S. A. E. G. 1991, MNRAS, 250, 581

Fan, X., et al. 2001, AJ, 122, 2833

Fanaroff, B. L., & Riley, J. M. 1974, MNRAS, 167, 31P

Fanti, C., Fanti, R., Dallacasa, D., Schilizzi, R. T., Spencer, R. E., & Stanghellini, C. 1995, A&A, 302, 317

Fender, R. P., Belloni, T. M., & Gallo, E. 2004, MNRAS, 355, 1105

Ferrarese, L., & Merritt, D. 2000, ApJ, 539, L9

Forman, W., et al. 2005, ApJ, 635, 894

Frederiksen, J. T., Hededal, C. B., Haugbølle, T., & Nordlund, Å. 2004, ApJ, 608, L13

Fukazawa, Y., Makishima, K., & Ohashi, T. 2004, PASJ, 56, 965

Gebhardt, K., et al. 2000, ApJ, 539, L13

Gomez, J. L., Marti, J. M., Marscher, A. P., Ibanez, J. M., & Alberdi, A. 1997, ApJ, 482, 33

Granato, G. L., De Zotti, G., Silva, L., Bressan, A., & Danese, L. 2004, ApJ, 600, 580

Gugliucci, N. E., Taylor, G. B., Peck, A. B., & Giroletti, M. 2005, ApJ, 622, 136

Hardcastle, M. J., Alexander, P., Pooley, G. G., & Riley, J. M. 1997, MNRAS, 288, 859

Hardcastle, M. J., Alexander, P., Pooley, G. G., & Riley, M. J. 1998, MNRAS, 296, 445

Hardcastle, M. J., & Worrall, D. M. 1999, MNRAS, 309, 969

Heinz, S., & Sunyaev, R. A. 2003, MNRAS, 343, L59

Hasinger, G., et al. 2001, A&A, 365, L45

Heinz, S., Reynolds, C. S., & Begelman, M. C. 1998, ApJ, 501, 126

Hirotani, K., Iguchi, S., Kimura, M., & Wajima, K. 1999, PASJ, 51, 263

Ho, L. C. 2005, Ap&SS, 300, 219

Isobe, N., Tashiro, M., Makishima, K., Iyomoto, N., Suzuki, M., Murakami, M. M., Mori, M., & Abe, K. 2002, ApJ, 580, L111

Ito, H., Kino, M., Kawakatu, N., Isobe, N., & Yamada, S. 2008, ApJ, 685, 828

Iwamoto, S., & Takahara, F. 2004, ApJ, 601, 78

Kaiser, C. R., & Alexander, P. 1997, MNRAS, 286, 215

Kaiser, C. R., & Alexander, P. 1999, MNRAS, 305, 707

Kataoka, J., et al. 2003, A&A, 410, 833

Kataoka, J., & Stawarz, L. 2005, ApJ, 622, 797

Kawaguchi, T., Shimura, T., & Mineshige, S. 2001, ApJ, 546, 966

Kawakatu, N., Umemura, M., & Mori, M. 2003, ApJ, 583, 85

Kawakatu, N., & Kino, M. 2006, MNRAS, 370, 1513

Kino, M., & Kawakatu, N. 2005, MNRAS, 364, 659

Kino, M., Kawakatu, N., & Ito, H. 2007, MNRAS, 376, 1630

Kino, M., & Takahara, F. 2004, MNRAS, 349, 336

Kirk, J. G., & Duffy, P. 1999, J. Phys. G, 25, 163

Komissarov, S. S. 1994, MNRAS, 269, 394

Komissarov, S. S., & Falle, S. A. E. G. 1997, MNRAS, 288, 833

Koratkar, A., & Blaes, O. 1999, PASP, 111, 1

Kraft, R. P., Nulsen, P. E. J., Birkinshaw, M., Worrall, D. M., Penna, R. F., Forman, W. R., Hardcastle, M. J., Jones, C., & Murray, S. S. 2007, ApJ, 665,1129

Kraft, R. P., Vázquez, S. E., Forman, W. R., Jones, C., Murray, S. S., Hardcastle, M. J., Worrall, D. M., & Churazov, E. 2003, ApJ, 592, 129

Krolik, J. H. 1999, Active galactic nuclei : from the central black hole to the galactic environment /Julian H. Krolik. Princeton, N. J. : Princeton University Press, c1999.,

Labiano, A., O'Dea, C. P., Barthel, P. D., de Vries, W. H., & Baum, S. A. 2008, A&A, 477, 491

Laing, R. A., & Bridle, A. H. 2002a, MNRAS, 336, 328

Laing, R. A., & Bridle, A. H. 2002b, MNRAS, 336, 1161

Laing, R. A., & Bridle, A. H. 2004, MNRAS, 348, 1459

Landau, L., & Lifshitz, F. M. 1959, Fluid Mechanics (London: Pergamon)

Leahy, J. P., & Gizani, N. A. B. 2001, ApJ, 555, 709

Leahy, J. P., & Perley, R. A. 1991, AJ, 102, 537

Leahy, J. P., Pooley, G. G., & Riley, M. 1986, MNRAS, 222, 753

Ledlow, M. J., & Owen, F. N. 1996, AJ, 112, 9

Liu, X., Cui, L., Luo, W.-F., Shi, W.-Z., & Song, H.-G. 2007, A&A, 470, 97

Longair, M. S. 1994, High Energy Astrophysics (Cambridge: Cambridge Univ. Press)

Manolakou, K., & Kirk, J. G. 2002, A&A, 391, 127

Marchesini, D., Celotti, A., & Ferrarese, L. 2004, MNRAS, 351, 733

Marscher, A. P., Jorstad, S. G., Gomez, J., Aller, M. S., Terasranta, H., Lister, M. L., & Stirling, A. M. 2002, Nature, 417, 625

Marti, J. M. A., Mueller, E., Font, J. A., Ibanez, J. M. A., & Marquina, A. 1997, ApJ, 479, 151

McHardy, M., Koerding, E., Knigge, C., Uttley, P., & Fender, R. P. 2006, Nature, 444, 730

Miley, G. 1980, ARA&A, 18, 16

Milne, P. A., Kroeger, R. A., Kurfess, J. D., & The, L.-S. 2002, New Astronomy Review, 46, 617

Mineshige, S., Kawaguchi, T., Takeuchi, M., & Hayashida, K. 2000, PASJ, 52, 499

Mioduszewski, A. J., Hughes, P. A., & Duncan, G. C. 1997, ApJ, 476, 649

Moss, D., & Shukurov, A. 1996, MNRAS, 279, 229

Mulchaey, J. S., & Zabludoff, A. I. 1998, ApJ, 496, 73

Murgia, M., Fanti, C., Fanti, R., Gregorini, L., Klein, U., Mack, K.-H., & Vigotti, M. 1999, A&A, 345, 769

Murgia, M. 2003, Publications of the Astronomical Society of Australia, 20, 19

Nishikawa, K.-I., Hardee, P., Richardson, G., Preece, R., Sol, H., & Fishman, G. J. 2003, ApJ, 595, 555

Norman, M. L., Winkler, K.-H. A., Smarr, L., & Smith, M. D. 1982, A&A, 113, 285

Nulsen, P. E. J., McNamara, B. R., Wise, M. W., & David, L. P. 2005, ApJ, 628, 629

O'Dea, C. P. 1998, PASP, 110, 493

O'Dea, C. P., & Baum, S. A. 1997, AJ, 113, 148

Orienti, M., Dallacasa, D., & Stanghellini, C. 2007, A&A, 461, 923

Padovani, P., & Urry, C. M. 1992, ApJ, 387, 449

Perley, R. A., Dreher, J. W., & Cowan, J. J. 1984, ApJ, 285, 35

Perucho, M., & Martí, J. M. 2007, MNRAS, 382, 526

Phillips, R. B., & Mutel, R. L. 1982, A&A, 106, 21

Piran, T. 1999, Phys. Rep., 314, 575

Polatidis, A. G., & Conway, J. E. 2003, Publications of the Astronomical Society of Australia, 20, 69

Pounds, K. A., Done, C., & Osborne, J. P. 1995, MNRAS, 277, L5

Rawlings, S., & Saunders, R. 1991, Nature, 349, 138

Raymond, J. C., Cox, D. P., & Smith, B. W. 1976, ApJ, 204, 290

Readhead, A. C. S., Taylor, G. B., Xu, W., Pearson, T. J., Wilkinson, P. N., & Polatidis, A. G. 1996a, ApJ, 460, 612

Readhead, A. C. S., Taylor, G. B., Pearson, T. J., & Wilkinson, P. N. 1996b, ApJ, 460, 634

Remillard, R. A., & McClintock, J. E. 2006, ARA&A, 44, 49

Reynolds, C. S., & Fabian, A. C. 1996, MNRAS, 278, 479

Reynolds, C. S., Fabian, A. C., Celotti, A., & Rees, M. J. 1996, MNRAS, 283, 873

Reynolds, C. S., Heinz, S., & Begelman, M. C. 2001, ApJ, 549, L1

Roques, J. P., et al. 2003, A&A, 411, L91

Rosen, A., & Hardee, P. E. 2000, ApJ, 542, 750

Rybicki, G. B., & Lightman, A. P. 1979, New York, Wiley-Interscience, 1979. 393 p.,

Scheck, L., Aloy, M. A., Marti, J. M., Gomez, J. L., & Muller, E. 2002, MNRAS, 331, 615

Schekochihin, A. A., Cowley, S. C., Kulsrud, R. M., Hammett, G. W., & Sharma, P. 2005, ApJ, 629, 139

Scheuer, P. A. G. 1974, MNRAS, 166, 513

Scheuer P. A. G. 1982, In *Extragalactic Radio Sources*, IAU Symposium No.97, edited by D. S. Heeschen and C. M. Wade (Reidel, Dordrecht), p. 163.

Schmidt, S. J., Connolly, A. J., & Hopkins, A. M. 2006, ApJ, 649, 63

Shakura, N. I., & Sunyaev, R. A. 1973, A&A, 24, 337

Shemmer, O., Brandt, W. N., Netzer, H., Maiolino, R., & Kaspi, S. 2006, ApJ, 646, L29

Shi, Y., et al. 2005, ApJ, 629, 88

Shields, G. A., Gebhardt, K., Salviander, S., Wills, B. J., Xie, B., Brotherton, M. S., Yuan, J., & Dietrich, M. 2003, ApJ, 583, 124

Shimada, N., & Hoshino, M. 2000, ApJ, 543, L67

Shimada, N., Terasawa, T., Hoshino, M., Naito, T., Matsui, H., Koi, T., & Maezawa, K. 1999, Ap&SS, 264, 481

Sikora, M., & Madejski, G. 2000, ApJ, 534, 109

Silk, J., & Rees, M. J. 1998, A&A, 331, L1

Smith, D. A., Wilson, A. S., Arnaud, K. A., Terashima, Y., & Young, A. J. 2002, ApJ, 565, 195

Stage, M. D., Allen, G. E., Houck, J. C., & Davis, J. E. 2006, Nature Physics, 2, 614

Tadhunter, C., Marconi, A., Axon, D., Wills, K., Robinson, T. G., & Jackson, N. 2003, MNRAS, 342, 861

Takahashi, T., et al. 2004, New Astronomy Review, 48, 269

Tanaka, T., et al. 2008, ApJ, 685, 988

Tavecchio, F., Maraschi, L., Sambruna, R. M., & Urry, C. M. 2000, ApJ, 544, L23

Totani, T. 1998, ApJ, 502, L13

Tremaine, S., et al. 2002, ApJ, 574, 740

Urry, C. M., & Padovani, P. 1995, PASP, 107, 803

Urry, C. M., Padovani, P., & Stickel, M. 1991, ApJ, 382, 501

van Breugel, W., Miley, G., & Heckman, T. 1984, AJ, 89, 5

Vikhlinin, A., Markevitch, M., & Murray, S. S. 2001, ApJ, 549, L47

Vink, J., Snellen, I., Mack, K.-H., & Schilizzi, R. 2006, MNRAS, 367, 928

Wardle, J. F. C., Homan, D. C., Ojha, R., & Roberts, D. H. 1998, Nature, 395, 457

Weaver, R., McCray, R., Castor, J., Shapiro, P., & Moore, R. 1977, ApJ, 218, 377

Wilkinson, P. N., Polatidis, A. G., Readhead, A. C. S., Xu, W., & Pearson, T. J. 1994, ApJ, 432, L87

Willot, C. J., Rawlings, S., Blundell, K. M., & Lacy, M. 1999, MNRAS, 309, 1017

Wilson, A. S., Young, A. J., & Shopbell, P. L. 2000, ApJ, 544, 27

Wilson, A. S., Smith, D. A., & Young, A. J. 2006, ApJ, 644, L9

Woo, J.-H., & Urry, C. M. 2002, ApJ, 579, 530

Yamazaki, R., Yoshida, T., Terasawa, T., Bamba, A., & Koyama, K. 2004, A&A, 416, 595

Zanni, C., Bodo, G., Rossi, P., Massaglia, S., Durbala, A., & Ferrari, A. 2003, A&A, 402, 949

Acknowledgments

It would have not been possible to write this doctoral thesis without the help and support of the kind people around me, to some of whom it is possible to give particular mention here.

I am deeply grateful to my supervisor, Prof. Shoichi Yamada for his guidance and support through my graduate course. His comments were always very fresh, and I was often encouraged by his advice. I am also indebted to Prof. Kei-Ichi Maeda for his guidance through my graduate course.

I would like to thank Dr. Motoki Kino for his constructive comments and tremendous patience during the course of this research. None of the works described in this thesis would have been possible without his support. I am also grateful to Dr. Nozomu Kawakatu for a lot of useful discussions and advise on the thesis. I thank Dr. Naoki Isobe for his comments on the observations of radio galaxies.

It has been a pleasure to work with all of the members of Yamada laboratory: Dr. Hidetomo Sawai, Dr. Ken'Ichiro Nakazato, Mr. Masaru Watanabe, Mr. Hiroki Nagakura, and so on. Particularly, I would like to thank Dr. Hidetomo Sawai for his friendship throughout my school life. I must also thank all the members of Maeda laboratory for fruitful discussions on the physics.

I would like to thank Dr. Hiroshi Nagai for valuable discussions on the radio observation with VLA radio telescope. I thank Mr. Masaomi Tanaka for useful comments on the optical observation.

Special thanks are to my fiancee Hiroko Andoh. Her cheerful encouragement and support made the stressful times bearable.

Finally to my family - I thank my parents and my sister for their kindness and continuous supports throughout my school life.